THE UNIVERSITY OF CHICAGO

A SEARCH FOR RESONANT PRODUCTION OF ZZ/ZW PAIRS IN THE SEMI-LEPTONIC $\ell\ell q\bar{q}$ FINAL STATE IN PROTON-PROTON COLLISIONS AT $\sqrt{s} = 8$ TeV WITH THE ATLAS DETECTOR

A DISSERTATION SUBMITTED TO

THE FACULTY OF THE DIVISION OF THE PHYSICAL SCIENCES

IN CANDIDACY FOR THE DEGREE OF

DOCTOR OF PHILOSOPHY

DEPARTMENT OF PHYSICS

BY

SAMUEL MEEHAN

CHICAGO, ILLINOIS

AUGUST 2014

This is dedicated to my parents, Ann and Jim Meehan, who taught me to love learning and have supported me the entire way.

Table of Contents

List of Figures

List of Tables

Acknowledgments

This work is by no means solely my own. It belongs collectively to those who have been influential throughout my education. To these people, thank you.

First and foremost, I thank my advisor, Mark Oreglia, who taught me how to find something that interested me and make it my own, all the while ensuring that I also recieved a fine education in the field of grappa. I further extend my gratitude to the entire group of ATLAS faculty at Chicago during my time here; Jim Pilcher, Frank Merrit, Mel Shochet, Florencia Cannelli, Young-Kee Kim, and David Miller. In addition, there have been a number of post-docs and graduate students in our group who have been a constant source of support and guidance in an "on the ground" kind of way ; Jordan Webster, Yang-Yang Cheng, Ho Ling Li, Chris Meyer, Constantinos Melachrinos, Anton Kapliy, Antonio Boveia, Joe Tuggle, Maria Fiascaris, and John Allison, in addition to the wonderful undergraduate students who I have supervised. More broadly, of the 3000 physicists in ATLAS and the TileCal collaboration, so many have made an impact on my education and I thank them all. In particular I thank my collaborators on this work; Koji Terashi, Alexander Oh, Steve Marsden, and Miles Wu, who have been so willing to share their expertise and enter into lengthy discussions time and time again. It is a delight to work with such wonderful people who share the passion for discovery and who refuse to settle.

Beyond ATLAS, I thank my educators at the University of Chicago. All of the staff who helped make sure that nothing went unsigned or unpayed, all the professors who instructed me in and outside the classroom, and all of my fellow graduate students who helped make what I learned stick, either by banging heads at a chalkboard or through impromptu conversations while eating lunch or working out[1], so many have been patient in helping me to develop as a scientist. In particular, I thank the following individuals from this group; Nobuko McNeill, Aspasia Sotir-Plutis, Autym Henderson, Kwang-Je Kim, Pavel Wiegmann, Henry Frisch, Fukun Tang, Jean-Francois Genat, Eric Oberla, Mark Miskin, Jake Ellowitz, Bobby Lanza, Mikhail Solon, Travis Maxfield, and Matthew Low.

Finally, there are so many individuals beyond the university and ATLAS that have been influential throughout my life. First and foremost, I thank my high school physics teacher Mr. Joseph Dumoulin, who taught me the power of curiosity and creativity and Kristen

1. "Hey, do you crossfit?"

Henry and Becca Beeman for learning to embrace the title of "nerd" from early on in life. And for all of my wonderful friends at University of New Hampshire, especially George Clark, Morgan O'Neill, and Vasya Vorotnikov who taught me, among other invaluable things, that drawing wonderfully round circles on chalk boards late at night in physics buildings is a wonderful learning tool. I further thank my good friend, Matthew Fleury, who "burnt it down" for two great years in Chicago with me and offerred invaluable support throughout a tumultuous time in my life. Lastly, I thank my entire family, from the aunts and cousins in Chicago (Al and Karen and Anthony and Erin), to the grandmas (Gram Betty and Grandma Wanda), to all the aunts and uncles further away, all of whom took a keen interest in what I was doing and made me feel that it was special to them as well. And finally to my brother, Patrick Meehan, sister, Liz Meehan, Dad, Jim Meehan, and Mom, Ann Meehan, I can't begin to thank you enough. Though not all of you are here, without any of you, it's sure that I wouldn't be here.

A million thanks to all.

Abstract

This thesis presents a search for resonant diboson production in the $\ell^+\ell^- q\bar{q}$ final state using 20.3 fb^{-1} of proton proton collision data collected at a center of mass energy of 8 TeV with the ATLAS detector. No significant excess over the Standard Model expectation is observed. Consequently 95% confidence level upper limits are set on the cross section times branching fraction for the production of bulk Randall-Sundrum gravitons and extended gauge model W' bosons, leading to the exclusion of masses below 740 and 1590 GeV, respectively.

Chapter 1
Introduction

Asking the question, *"What is fundamental?"* has been a continuous source of curiosity and has driven science to innovate in order to discover ever more basic building blocks of nature. Beginning with the theory of atoms by Democritus and spanning thousands of years, the pursuit of an answer to this question by great minds including Isaac Newton, Marie Curie, Enrico Fermi, and Richard Feynman has led to the Standard Model, a quantum field theoretic description of the interactions of fundamental particles that describes a vast number of phenomena to great precision. Initially conceived 30 years ago [3], the Large Hadron Collider (LHC) and its experiments aimed to discover, among other things, a key ingredient to this theory, the Higgs boson. With its discovery in July of 2012 [4, 5], the Standard Model was yet again vindicated as a successful description of nature and the LHC was proven to do what it was built to do, discover. Yet even with the discovery of the Higgs boson, we are aware of a number of observational problems and curiosities not accounted for in the Standard Model that beg for new physics. And we are confident that if something more exists within our reach that may lead to a deeper understanding of the fundamental building blocks of nature, the LHC machine and the experiments instrumented on it, are capable of discovering it.

With that in mind, this thesis presents a search for, and subsequent constraints placed on, new physics performed with the ATLAS experiment at the LHC. More specifically, the search focuses on signatures coming from the s-channel production of massive particles decaying to pairs of W and Z gauge bosons, either ZZ or ZW, with the subsequent decay of one Z boson to a pair of charged leptons and the other W or Z boson to a quark anti-quark pair. Searching for such a diboson signature probes new physics at and past the TeV scale. However, venturing to such mass scales presents a new set of challenges for the identification of hadronically decaying bosons. The techniques developed to deal with these new hadronic final states falls under the name of *jet substructure* and in the context of this thesis, those pertaining to boson jet tagging, were investigated and exercised in one of the first searches of its kind at the LHC.

Although no deviation from the Standard Model expectation is observed, the progress towards answering the initial question *"What is fundamental?"* is twofold. First, it vindicates the extreme predictive power of the theoretical framework we do have to make predictions of particle interactions at higher energy scales and constrains what new physics is believed to exist. Second, it provides an affirmation that new techniques being developed to exploit the full potential of the LHC as a discovery machine, namely jet substructure, do work and will allow the proverbial lamp-post under which we are able to explore to shed a broader light.

The content of this thesis is as follows. In Chapter 2, the Standard Model is briefly reviewed and motivation is given to search for signatures beyond the Standard Model with pairs of W and Z bosons. In Chapter 3, the LHC and the ATLAS experiment are briefly described. Chapter 4 presents the techniques of jet reconstruction and jet substructure as pertaining to boson jet tagging. The search itself is described in Chapter 5 with the results and constraints on new physics presented in Chapter 6. Finally, a brief conclusion is given in Chapter 7.

Chapter 2
Going Beyond the Standard Model

2.1 The Standard Model

During the course of the 20^{th} century, the quest to understand the basic building blocks of nature was pursued through the development of a new description of nature at the small scale; quantum mechanics. Initially proposed by Max Planck as a solution to the ultraviolet catastrophe, quantum mechanics led the way to the development of what came to be known as quantum field theory. In turn, guided by experimental results and the principle of beauty in symmetry, a quantum field theory describing three of the four known fundamental emerged as the Standard Model.

The Standard Model, a more complete description of which can be found in [6, 7] but whose salient points are summarized here, is a theory in which interactions between matter are governed by local principles of symmetry associated with the Lagrangian. In the Standard Model, there are two types of a spin $\frac{1}{2}$ matter fields, quarks and leptons. There are two types of quarks (i.e. up-type and down-type) and two types of leptons (i.e. charged leptons and neutrinos), each of which come in three families and each of which, except the neutrinos, has a corresponding anti-matter field. Moreover, each quark possesses a further property, "color" charge, which can take one of the three values red, green, or blue. The symmetry principle governing the interactions of these matter fields is composed of the set of local transformations defined by the group $SU(3)_c \times SU(2)_L \times U(1)_Y$. This set of transformations is a set of gauge transformations, meaning that to preserve symmetry under a given transformation requires the introduction of additional fields, spin 1 gauge fields, in the Lagrangian which then become associated with new particles. In particular, the $SU(3)_c$ gauge group is responsible for the strong interaction and is associated with eight gluon fields which themselves carry color charge and which mediate the interactions between colored objects, quarks and gluons. The $SU(2)_L \times U(1)_Y$ group together form the electroweak gauge group which is associated with three fields from $SU(2)_L$ and one field from $U(1)_Y$. Together, the set of terms containing these fields are combined through electroweak symmetry breaking as linear combinations of each other that gives rise to the more familiar $W^{\pm}$, Z, and γ fields.

Provided this set of matter fields and gauge fields, the resulting Lagrangian is composed of the set of all renormalizable[1] terms that are invariant under this gauge group and Lorentz transformations. However, with only these components, all particles of the Standard Model would be massless[2]. Therefore, the final component, the Brout-Englert-Higgs mechanism, prescribes the addition of spin 0 scalar field, associated with the Higgs boson, which acquires a vacuum expectation value through electroweak symmetry breaking which in turn gives rise to the masses of the fermions and the bosons. With the addition of the set of all possible additional terms that can be added due to the introduction of the Higgs field, the Standard Model Lagrangian is complete.

This mathematical object can be understood as a set of rules governing the possible types of interactions between the fields within it. The strengths of these interactions are tuned by experimentally measurable coupling constants that scale the size of each interaction term and provide parameters in which to perform mathematical expansion that allow for perturbative calculations of various processes to be made. At the LHC, these probabilities are expressed as measurable cross sections [3] and can be calculated with increasing accuracy, by adding more complex subleading terms to the expansion. The somewhat astonishing part is that these calculations, when compared to the experimentally measured rates as shown in Figure 2.1, describe these rates to a high level of precision.

2.2 Looking Beyond

Measurements spanning of a wide array of physics processes at the LHC can be described to great precision through the Standard Model. Nonetheless, a number of reasons exist to require physics beyond the Standard Model and believe that it is within the reach of the LHC.

1. Renormalizable means that the details of physics happening at an energy scale beyond the intended applicability of the theory itself does not affect the ability of the theory to make definite predictions as it only enters through small contributions to parameters that can be experimentally measured and used as inputs to the theory.

2. In fact, they would acquire small masses from QCD, but not enough to account for the observed values [8].

3. Cross sections at the LHC are typically measured in picobarns (pb) where 1 pb= 10^{-36} and in a classical sense can be thought of as the cross sectional area of the proton that, if entering into a collision, will result in a given process.

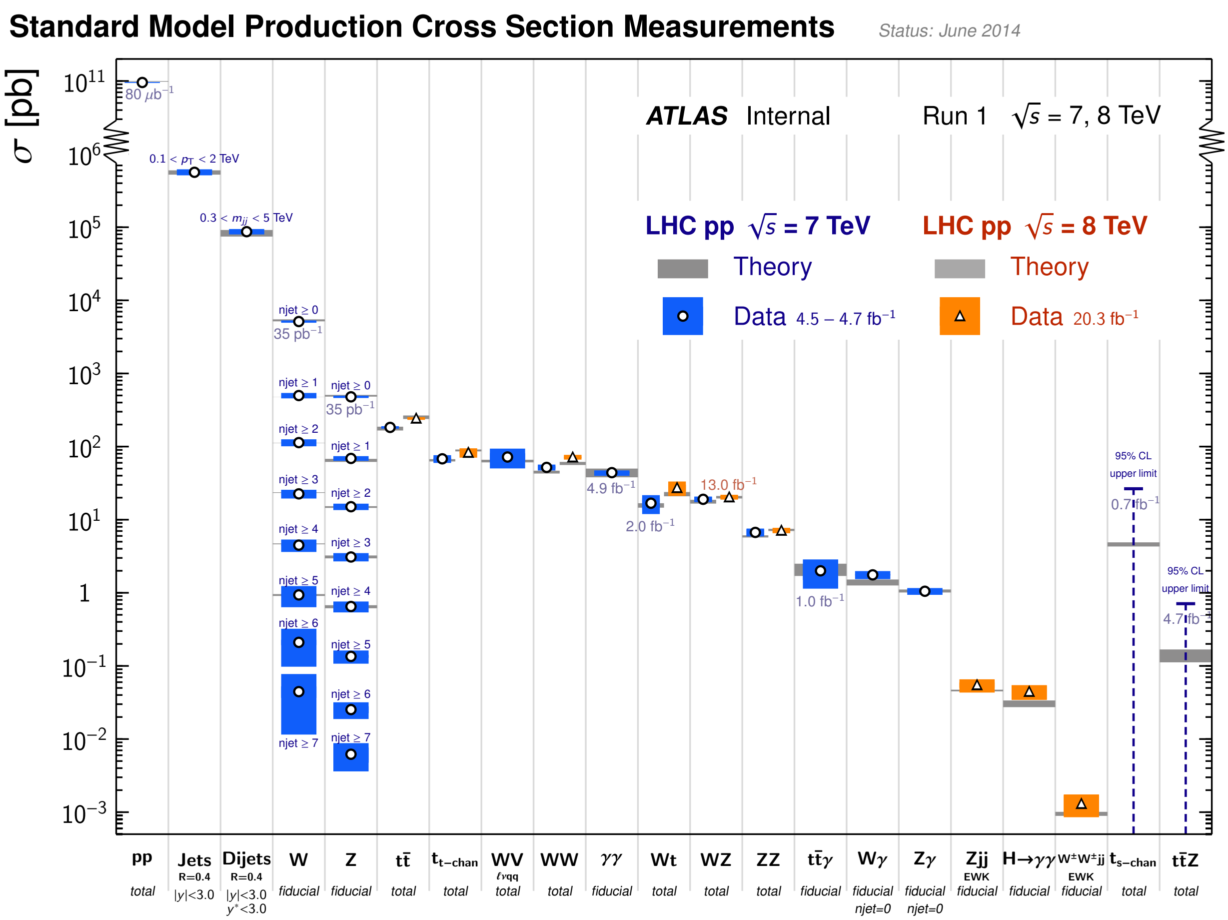

Figure 2.1: Comparison of experimentally measured cross sections in ATLAS to theoretical prediction for a number of physics processes.

First, it is known from neutrino oscillations [9] that neutrinos, which are taken as massless in the Standard Model, have mass, albeit very small. Second, the content of the early universe should naively be symmetrically composed of matter and anti-matter and all processes of annihilation or creation of matter would need to preserve this symmetry. However, the observable universe at present is composed overwhelmingly of matter and there exists no confirmed mechanism within the Standard Model to explain this transition to a state of asymmetry. Finally, there is overwhelming astronomical evidence for the existence of dark matter [10] and dark energy [11], which together account for over 95% of the energy content of the universe. Yet there exists no particle description of either of these phenomena in the Standard Model.

Furthermore, there exists a strong reason to believe that the new physics involved in explaining these phenomena will manifest itself at the LHC. This arises from the idea of naturalness which has manifested itself numerous times to guide the discovery of new particles. It relies on the separation of scales, the basic assumption that a physical theory at one energy scale will make sensible predictions until some high scale Λ beyond which the degrees of freedom in the theory being used are not those at work in nature. In other words, the theory must be modified to correctly describe these higher energy experiments and in quantum field theory, this is accomplished by introducing new particles. Three past predictions illustrate the power of this principle very well. The first is the introduction of the positron due to the breakdown of the calculation of the classical self energy of the electron [12]. The next is the prediction of the existence of a new particle, the ρ meson ($m_\rho \sim 770$ MeV), at an energy scale less than $\Lambda < 850$ MeV coming from the need to cancel the quadratic divergence of the prediction of the pion mass difference arising from QED corrections [13]. Lastly, the introduction of the charm quark ($m_c \sim 1.3$ GeV), through the GIM mechanism, was foreshadowed by the inability to predict the neutral kaon mass difference in a three quark model and required new physics at an energy scale less than $\Lambda < 2$ GeV [13].

Currently, this idea of naturalness and scale separation arises in the Standard Model through the calculation of the Higgs boson mass. Due to the combination of loop corrections from all particles, but primarily the top quark and W bosons, the Higgs mass is quadratically divergent and predicted to be on the order of the Planck scale ($\sim 10^{18}$ GeV) but it has been observed at $m_h \sim 125$ GeV. One explanation of this curious separation of scales is that the couplings of the Higgs boson to the Standard Model particles (i.e. top quark) are "finely tuned" in the sense that they take values that cause for cancellations to happen that give a mass of 125 GeV. However, these cancellations would have to involve separate contributions that each have absolute values of approximately the Planck scale. Therefore, the precision with which these cancellations must occur is approximately 10^{-16}, which is deemed by many to be *unnatural*. Explaining this unnaturally large separation of scales between that at which the the cancellations occur (Planck scale) and that at which we observe the Higgs boson (electroweak scale) is the way in which the naturalness problems currently manifests itself at the LHC. Luckily, many extensions of the Standard Model, illustrated on the left side of Figure 2.2 [14], that explain the aforementioned problems also offer an explaination to explain this unnatural hierarchy and require new physics to exist at the energy scale of approximately 1 TeV, that being probed by the LHC.

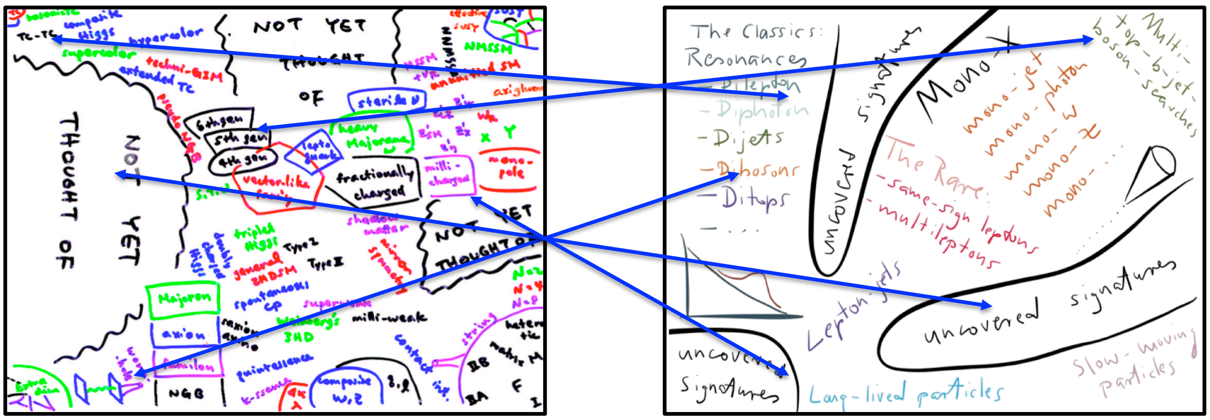

Figure 2.2: Illustration of the mapping between the space of beyond the Standard Model theories (left) and the subsequent experimental signature produced at the LHC.

Typically, these models are predicted to manifest themselves as distinctive *signatures* (right side of Figure 2.2) in LHC collisions through the production and decay of new, and typically massive, particles. Therefore, by performing a signature based search for events with certain characteristics, events can be studied that likely arise from beyond the Standard Model physics. The rate of production of such events can then be compared to the well understood and precise predictions of the Standard Model and deviations from these predictions can confirm or refute the existence of new physics. However, there is not a one to one correspondence between models and signatures and in many cases one signature can result from the existence of multiple possible new physics models. It is therefore efficient to strategize searches for new physics through classification in terms of the final state signature used to search for new physics and in doing so cover multiple new physics scenarios.

The classes of signatures are typically grouped based on the types of final state objects (e.g. leptons, jets, missing transverse energy) and intermediate topologies (i.e. top quarks, bosons, etc.) from which they originate. One such signature involves the intermediate state topology of pairs of W and Z bosons (e.g. WW,WZ,ZZ) that result from the decay of a massive s-channel resonance. The final state signature is fully defined by the subsequent decay of the W and Z bosons which can proceed through either the leptonic channel ($Z \to \ell^+\ell^-$, $Z \to \nu\bar{\nu}$, and $W \to \ell\nu$) or the hadronic channel ($W/Z \to q\bar{q}$). The leptonic decay mode has the benefit that leptons [4] are well understood physics objects with signatures that are easily identifiable. The hadronic decay mode, however, has the benefit that the branching fraction of W/Z to quarks ($B(W \to q\bar{q}) \sim 68\%$ and $B(Z \to q\bar{q}) \sim 69\%$) is much greater than the branching fraction to leptons ($B(W \to \ell\nu) \sim 10.8\%$, $B(Z \to \ell^+\ell^-) \sim 11\%$, and $B(Z \to \nu\bar{\nu}) \sim 20\%$) due to the three quark color charges. Therefore, choosing to search for the semi-leptonic final state, in a subset of events containing a real $Z \to \ell\ell$ decay and one decay of $W/Z \to q\bar{q}$, strikes a balance between these two regimes and is expected to give good sensitivity to new physics across a broad mass range. In particular, it is expected that in the intermediate mass range near 1 TeV, where fully leptonic signatures run out of statistics and all hadronic signatures are still overwhelmed by backgrounds, the semileptonic final states, of which $\ell\ell qq$ is one, will provide the best sensitivity, as shown in Appendix E.

This single final state signature can be used to search for particles produced in the context of multiple new physics scenarios. Two specific benchmark models are chosen with which to interpret the result and determine, in the absence of an excess, the extent to which new physics is constrained. The first is the production of Kaluza-Klein modes of the graviton within the context of the bulk Randall-Sundrum framework of extra dimensions. The second is the production of W' bosons resulting from a simple extension of the standard model, the extended gauge model.

2.2.1 The Bulk Randall-Sundrum Graviton

The first new physics scenario covered by this signature is the production of Kaluza-Klein modes of the graviton (G^*), in particular, from the bulk Randall-Sundrum model of extra dimensions [15, 16]. The bulk Randall-Sundrum model proposes a solution to the previously mentioned hierarchy problem through the introduction of a single warped extra dimension. Solving Einsteins equations with the addition of this extra dimension yields the spacetime metric

$$ds^2 = e^{-2kr_c|\phi|}\eta_{\mu\nu}dx^\mu dx^\nu + r_c^2 d\phi^2 \tag{2.1}$$

4. In ATLAS, and in this analysis in particular, a lepton commonly refers to an electron or a muon. This is because τ lepton decays, due to their increased mass, leave a very different experimental signature, closer to that of a hadronic jet and require much greater care in understanding.

which has two free parameters, k and r_c, representing a common energy scale of the theory and the radius of curvature of the warped extra dimension, respectively. This extra dimension provides a bulk separation between two $3+1$ dimensional branes, on which occur dynamics at the ultraviolet (UV) scale and the infrared (IR) scale. Through careful analysis of the Higgs contribution to the Lagrangian in this framework, it can be seen that the vacuum expectation value of the Higgs on the IR brane, v, is related to that on the UV brane, v_0, as $v = e^{-kr_c\pi}v_0$. Apparently large separations in scale at the IR brane are therefore understood as small separations at the Planck scale that have simply been enhanced when observed at the lower scale IR brane due to the warping of the extra dimension.

Furthermore, as a result of the warped nature of the extra dimension, the massless graviton acquires an entire tower of excited states, called Kaluza-Klein modes, that result from the necessary periodic boundary conditions of the field in the extra dimension, and it is these states that can be produced and searched for at the LHC. It is necessary to fix two features of the model in order to specify the phenomenology. The first is the scale of the extra dimension, which requires specifying values for k and r_c. The reduction of scale separations can be achieved for values of $kr_c \sim 11$ which is the value used in this benchmark model. The only free parameter of the model is therefore the scale k, which is fixed to the Planck scale by requiring $k/\bar{M}_{Pl} = 1.0$ [5], where $\bar{M}_{Pl}$ is the reduced Planck mass; $\frac{M_{Pl}}{\sqrt{8\pi}}$. Also affecting the phenomenology of the graviton signature is the manner in which the wavefunction of fields (Standard Model or otherwise) populate the extra dimension, how these wavefunctions overlap, and in doing so influence their respective couplings. Typically, the massless graviton is localized near the UV brane and Higgs field and Kaluza-Klein G^*excitations are taken to be localized near the IR brane. Given this condition, if the three flavors of quarks are made to be localized at difference locations in the bulk space between the UV and IR branes, then the overlap with the Higgs wavefunction can be tuned to explain the hierarchical nature of the masses of the three families. In turn, this means that the coupling to the graviton, and so the massive Kaluza Klein modes of the graviton, will be small. However, the overlap with the wavefunctions of the longitudinal modes of the gauge boson wavefunctions (W_L/Z_L) can be large and so provide a striking signature through their final state decay products. There are two such channels, the $G^* \to W^+W^-$ and $G^* \to ZZ$, the couplings specified through the

5. It should also be noted that the final result is also interpreted in terms of the model with $k/\bar{M}_{Pl} = 0.5$

interaction of the graviton field ($h_{\alpha\beta}$) with the energy momentum tensor of the longitudinal components of the W and Z bosons ($T_{\mu\nu}^{W_L,Z_L}$) as

$$\mathcal{L}_G \sim \frac{e^{kr_c\pi}}{\bar{M}_{Pl}}\eta^{\mu\alpha}\eta^{\nu\beta}h_{\alpha\beta}T_{\mu\nu}^{W_L,Z_L} \tag{2.2}$$

Both of these decays are searched for in ATLAS, but the focus for this analysis is the $G^* \to ZZ$ channel.

For implementation in the search, this model is simulated at leading order in CalcHEP v3.2 [17] with `CTEQ6L1` [18] parton distribution functions and normalized to the leading order cross section. The produced events are then passed to PYTHIA 8 [19] for parton showering and hadronization. Because different signal masses produce different experimental signatures, events are produced with a variety of values for the G^* pole mass; from 300 to 1000 GeV with 50 GeV steps, and from 1000 to 2000 GeV with 100 GeV steps. The width of this signal varies with the pole mass and is 2.8% (5.5%, 6.1%) at a mass of 300 GeV (1 TeV, 2 TeV).

2.2.2 The Extended Gauge Model W'

The second new physics scenario covered by this signature is a result of the sequential standard model (SSM) [20]. Unlike the Randall-Sundrum model of extra dimensions, the sequential standard model is not the consequence of a top down solution to a specific, “big” problem. Although it is inspired by aspects of a strongly interacting Higgs sector, it instead takes a bottom up approach to predicting new phenomenology expected at the LHC. The general idea, proposed following the discovery of the W and Z bosons [21, 22], posits the existence of heavier copies of these particles that possess the same basic properties, referred to as the W' and Z', commonly V. Because the properties are the same, the structure of the couplings to the Standard Model are identical to those of the standard W and Z, with possible modifications to the strength of these couplings. For masses below the WW and WZ thresholds, fermion couplings dominate, but when this threshold is passed, as at the LHC, the decay to ZW and WW dominates and increases like $M(V)^5$. This very dramatic increase is corrected by allowing for mixing between the Standard Model and SSM gauge bosons which results in an overall scaling of the VWW and VWZ couplings by a mixing factor of $c\frac{M_W^2}{M_V^2}$, where c is a tunable coupling strength, taken to be $c = 1$ in this search, resulting in what is commonly referred to as the extended gauge model (EGM). The interaction term of the Lagrangian thus takes the same form as the triple gauge coupling in the Standard Model with one leg being the new W' boson as

$$\mathcal{L}_{EGM,W'} \sim \frac{M_W^2}{M_W'^2} W' W Z \tag{2.3}$$

As in the case of the bulk Randall-Sundrum graviton, the two decays $W' \to ZW$ and $Z' \to W^+W^-$ exist and although both are searched for in ATLAS, the specific final state signature examined here probes the existence of $W' \to ZW$.

For implementation in this search, this model is simulated at leading order using PYTHIA 8 with with `MSTW2008OLO` [23] parton distribution functions. Because the sequential standard model W', by definition, couples to Standard Model particles with the same strength as the Standard Model W boson, it is more important to consider higher order contributions to the total cross section and therefore, next-to-next-to-leading order k factors are applied as a function of the W' pole mass. Events are produced for W' pole masses ranging from 300 to 2000 GeV with 100 GeV steps. The width of this signal varies with the pole mass and is 3.2% (3.6%, 3.6%) at a mass of 300 GeV (1 TeV, 2 TeV).

2.2.3 Previous Searches

Searches such as this, for resonant production of pairs of W and Z bosons in a number of final states, have been performed previously at both the Tevatron and the LHC, all of which have resulted in constraints on new physics. At the Tevatron, the D0 collaboration searched for WZ resonances decaying to $\ell\nu\ell\ell$, $\ell\nu qq$ and $qq\ell\ell$ [24] excluding the extended gauge model W' boson between 180 GeV and 690 GeV and the Randall-Sundrum graviton[6] between 300 GeV and 754 GeV. The CDF collaboration performed similar searches in the $X \to WW/WZ \to e\nu qq$ channel [25] and $X \to ZZ \to \ell\ell\ell\ell, \ell\ell qq, \ell\ell\nu\nu$ channels [26]. In the former, the result lead to the exclusion Randall-Sundrum gravitons below 607 GeV and W' bosons between 285 GeV and 516 GeV. In the latter, although there was an excess of three events in the four lepton channel close to an invariant mass of 325 GeV, these data were found

6. It should be noted that the Randall-Sundrum graviton model used to perform these interpretations at the Tevatron is the original model proposed in [15], which is different than the bulk Randall-Sundrum model used in the search described in this thesis. Therefore, a direct comparison to these results is difficult.

to be consistent with a background fluctuation and so limits were set on Randall-Sundrum gravitons, presented as limits on production cross section times branching fraction to ZZ and varied from approximately 0.3 pb at low mass (250 GeV) to 0.04 pb at high mass (1000 GeV). At the LHC, the CMS collaboration has performed searches for diboson resonances in the semileptonic channels ($WW/WZ \to \ell\nu qq$ and $ZZ/WZ \to \ell\ell qq$) [27] and the fully hadronic channel ($WW/WZ/ZZ \to qqq'q'$) [28], both requiring that the $q\bar{q}$ pair be reconstructed as a single jet and then exploiting jet substructure techniques to improve sensitivity. From these, the highest mass reach is obtained in the fully hadronic channel which is able to exclude W' boson masses up to 1.7 TeV and bulk Randall-Sundrum graviton masses up to 1.2 TeV. The last search of this type performed by the ATLAS collaboration was in the combined $ZZ \to \ell\ell\ell\ell,\ell\ell qq$ channel using 1 fb^{-1} of data at $\sqrt{s} = 7$ TeV [29] and was interpreted in the context of the original Randall-Sundrum graviton model, not the bulk Randall-Sundrum model, resulting in a lower mass limit of 845 GeV. Therefore, an update of this search with a significantly larger dataset and improved analysis techniques will significantly improve constraints.

Chapter 3
The LHC and ATLAS

3.1 The LHC Machine

The Large Hadron Collider [30], located underground at the CERN laboratory near Geneva, Switzerland is designed to probe the energy frontier at the smallest length scales through the collision of protons at a maximum center of mass energy of $\sqrt{s} = 14$ TeV and luminosity of $\mathcal{L} = 10^{34} cm^{-2} s^{-1}$[1]. These collisions occur at four interaction points around the LHC ring, as shown in Figure 3.1, each of which is instrumented with an experiment. Two all-purpose experiments are designed to study the high luminosity proton-proton collisions. These are CMS (The Compact Muon Solenoid experiment) and ATLAS (A Toroidal LHC ApparatuS), which is the experiment used to perform this search. A third experiment, LHCb (The Large Hadron Collider Beauty experiment), collects luminosity at intentionally reduced rates to allow for precision studies of b physics and a fourth experiment, ALICE (A Large Ion Collider Experiment), is designed specifically to study the phenomenology of strongly interacting matter in heavy ion collisions.

The LHC is a superconducting collider circulating two beams of protons in opposite directions. During the 2012 data taking period, the beam energy was 4 TeV, producing a proton-proton center of mass energy of 8 TeV. This final energy of a single beam in the LHC is achieved through a series of accelerating stages. The protons start by being ionized and accelerated in the LINAC2 (LINear ACcelerate 2) to an energy of 50 MeV. They are then injected into the PS Booster (Proton Synchrotron Booster) which further increases the energy of the protons to 1.4 GeV. From here, the protons are injected into the SPS (Super Proton Synchrotron) which increases their energy to 450 GeV and finally into the LHC which completes the ramping of the energy to the final target energy. Throughout this entire process, the acceleration occurs through the application of an oscillating electric field in resonant frequency (RF) cavities that impart energy to the electron in short bursts. Thus, the beam entering the LHC is not continuous but rather partitioned into “bunches”, with 1380 bunches circulating in each beam during 2012, each of which contains approximately 115 billion pro-

1. It is further capable of being made to collide heavy ions at a maximum nucleon-nucleon energy of $\sqrt{s_{NN}} = 2.8$ TeV and luminosity of $\mathcal{L} = 10^{27} cm^{-2} s^{-1}$, but these collisions are not directly utilized in this work.

tons and are separated by 50 ns, two times the minimum 25 ns bunch spacing that is set by the frequency of the RF cavities in the LHC; 40 MHz. The two counterrotating beams are circulated in separate beamlines, but are contained within the same cryogenics system due to space constraints and so share a common dipole magnetic field used to steer the beams around the ring. The beams pass through eight straight sections and eight bending sections during one pass around the machine, continually being focused by quadrupole magnets to preserve the emittance of the beam. They are brought into collision at the interaction points of the experiments collecting data with those collisions and provide a maximum peak luminosity of approximately a few times $10^{34} cm^{-2} s^{-1}$. The collisions are sustained but slowly cause the beam emittance, and thus the instantaneous luminosity delivered, to decrease until after 10-20 hours of continuous operation, the beam is dumped and a new beam is injected. This period of running constitutes a single fill of the LHC and typically delivers approximately 100 pb^{-1} of luminosity. During the period of running in 2012, the accumulation of multiple fills lead to a total of 23.3 fb^{-1} of integrated luminosity delivered to ATLAS, with detector inefficiencies leading to a recorded luminosity of approximately 21.3 fb^{-1}. This is the dataset that was analyzed to perform this search.

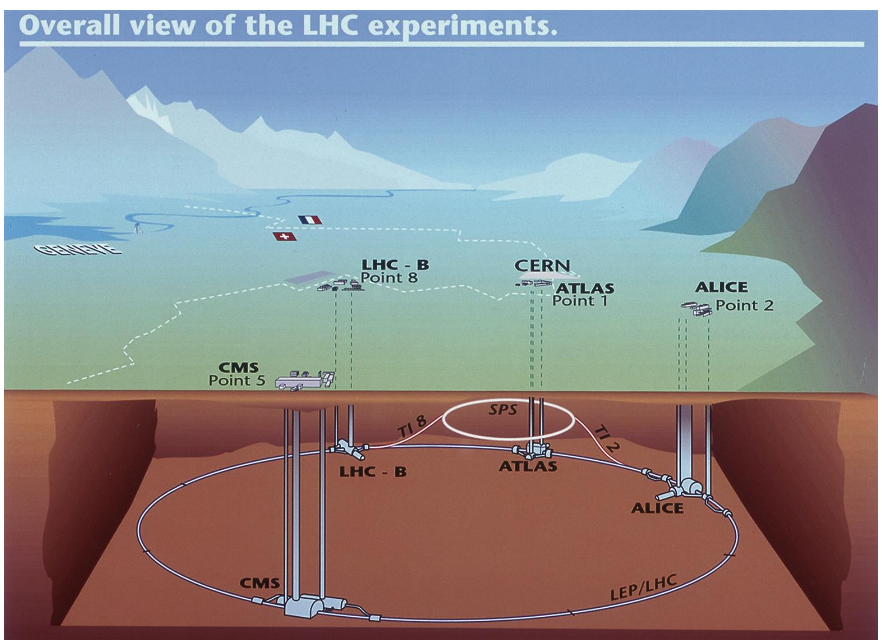

Figure 3.1: A schematic of the Large Hadron Collider and the four experiments (ATLAS, CMS, LHCb, and ALICE) underneath the CERN laboratory and the surrounding area on the border of France and Switzerland near Geneva.

3.2 The ATLAS Detector

The ATLAS detector is an all-purpose particle physics detector designed to operate in a high luminosity environment and accurately reconstruct proton proton collisions. There were multiple criteria on which the design of the detector was focused and those criteria that make this search possible are:

1. High precision measurement of muon momentum to very high energies.
2. High precision and efficient tracking of charged particles for charged particle identification and reconstruction.
3. Very good electromagnetic and hadronic calorimetry providing maximum possible fiducial coverage for the precise measurement of electrons, photons, and jets in addition to the reconstruction of missing transverse energy.

These three criteria by themselves necessitated the construction of the main subsystems of ATLAS; the inner detector, the calorimeter system, and the muon spectrometer, as shown in Figure 3.2. These subdetectors are arranged in concentric cylinders and disk shaped endcaps surrounding the interaction point to provide a nearly hermetic coverage to allow for full reconstruction of events. A full technical description of these various subsystems and the manner in which they are integrated is described at great length in [31], but a short discussion of each is provided here, focussing on the main design features important for this analysis.

3.2.1 The Inner Detector

The inner detector (ID), shown in Figure 3.3, is situated closest to the interaction point and is primarily responsible for reconstructing the trajectories of charged particles. This is achieved by instrumenting the space with a number of layers to provide precise spatial measurements, hits in (r, η, ϕ)[2], of passing charged particles that follows helical trajectories

2. ATLAS uses a right-handed coordinate system with the z-axis along the beam pipe. The x-axis points to the center of the LHC ring, and the y-axis points upward. The pseudorapidity is defined in terms of the polar angle θ as $\eta = ln(tan(\theta/2))$, ϕ is the azimuthal angle measured around the beamline, and r is the radial distance from the beamline.

due to the presence of a 2T solenoidal magnetic field produced by a superconducting solenoid. Therefore, the primary goal of the inner detector is to provide accurate measurements of these hits. This is achieved by using three different subdetectors based on two technologies that, in addition to providing this set of hits, provide measurements that are essential for particle identification.

The innermost subdetector is the silicon pixel detector. It is composed of silicon detector modules divided into small regions, pixels, that are 50 μm by 400 μm. When a charged particle passes through a pixel, electron hole pairs are generated, drift in the applied electric field and are collected and read out, thus registering a hit. The very small size of each pixel is necessary in this region for two reasons. The first is to obtain extremely precise spatial measurements in the (η, ϕ) plane and the second is that, due to the high flux of particles close to the interaction, small active regions ensure that the pixels are not continually busy

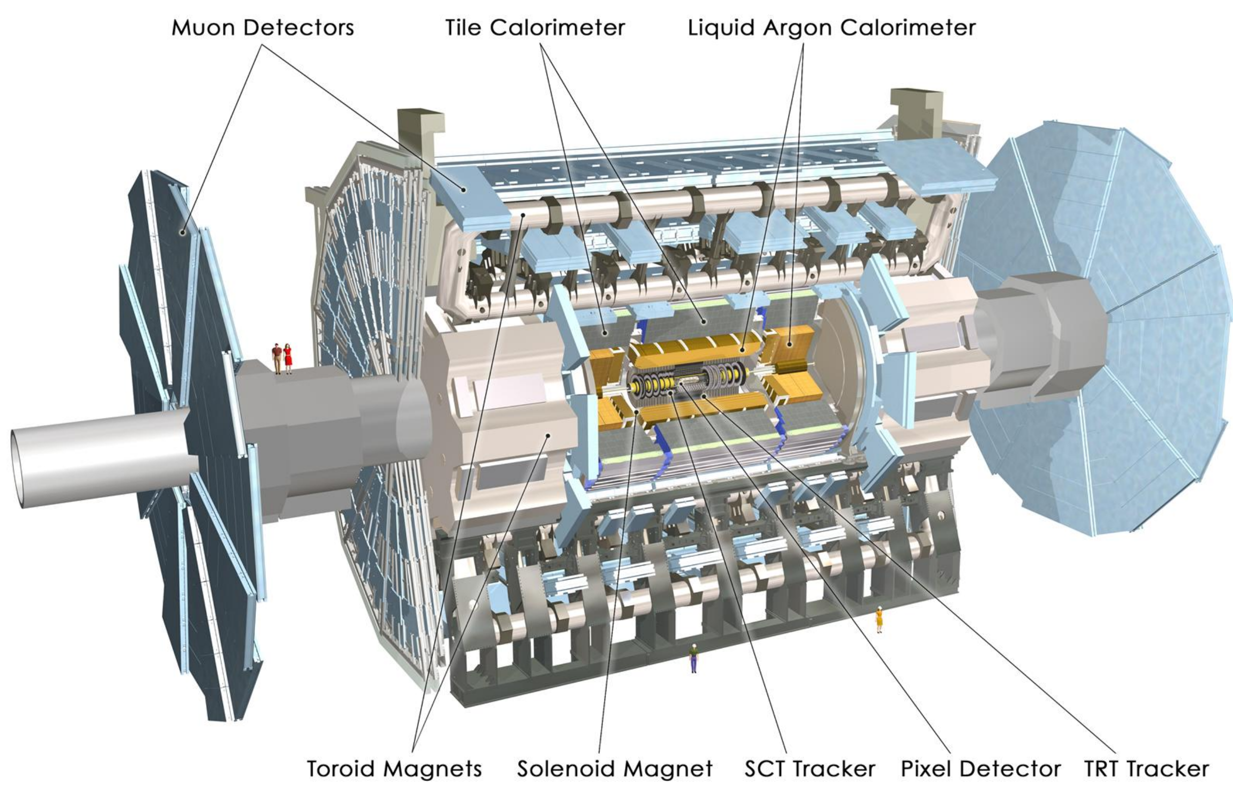

Figure 3.2: Schematic design of the ATLAS detector showing the three main subsystems (inner detector, calorimetry, and muon spectrometer) and further subdetectors of this construction.

reading out the signal from previous bunch crossings. These detectors are instrumented in two configurations. The barrel region consists of three concentric cylinders of these detectors and more forward regions are instrumented with three endcap layers, providing coverage out to $|\eta| < 2.5$.

Outside of the pixel detector is the silicon strip tracking detector (SCT). The SCT functions based on the same principle as the pixel detectors; a passing charged particle creates electron hole pairs which drift in an electric field and are collected and read out. The difference is that rather than being read out with individual pixels that provide a simultaneous (η, ϕ) measurement, the silicon modules are instrumented with many sets of strips, cathodes, that give a measurement in a single coordinates. Therefore, to obtain a full (η, ϕ) measurement, a second detector is instrumented to provide an orthogonal measurement. As in the case of the pixel detector, two regions are instrumented. The barrel region is instrumented with four layers (detector pairs) and nine endcaps provide coverage out to $|\eta| < 2.5$.

The outermost subdetector is the transition radiation tracker (TRT). The TRT is composed of straw tubes filled with a mixture of xenon gas and CO_2 with a gold plated tungsten wire held under tension in the center of the tube held at high voltage with respect to the tube. When a charged particle passes, the gas is ionized and the charge drifts and is collected by the wire and registered as a hit. This provides a measurement in two dimensions and can be used to follow tracks originating in the pixel detector and SCT. These straw tube detectors are, as with the pixel and SCT, arranged in a barrel and endcap configuration for maximal coverage out to $|\eta| < 2.0$. The barrel configuration is instrumented with 70 layers of straw tubes, aligned along the z direction and making measurements in the (r, ϕ) plane. Each endcap is composed of multiple disks of straw tubes with a total of 140 layers of straw tubes in each endcap that make measurements in the (z, ϕ) plane. In addition to providing added precision to the measurement of tracks from charged particles, the TRT provides particle identification handles for discriminating charged pions from electrons. This is achieved through the measurement of the amount of transitions radiation which, being a function of the $\gamma = E/mc^2$ of the passing particle, is much smaller for a pion than an electron.

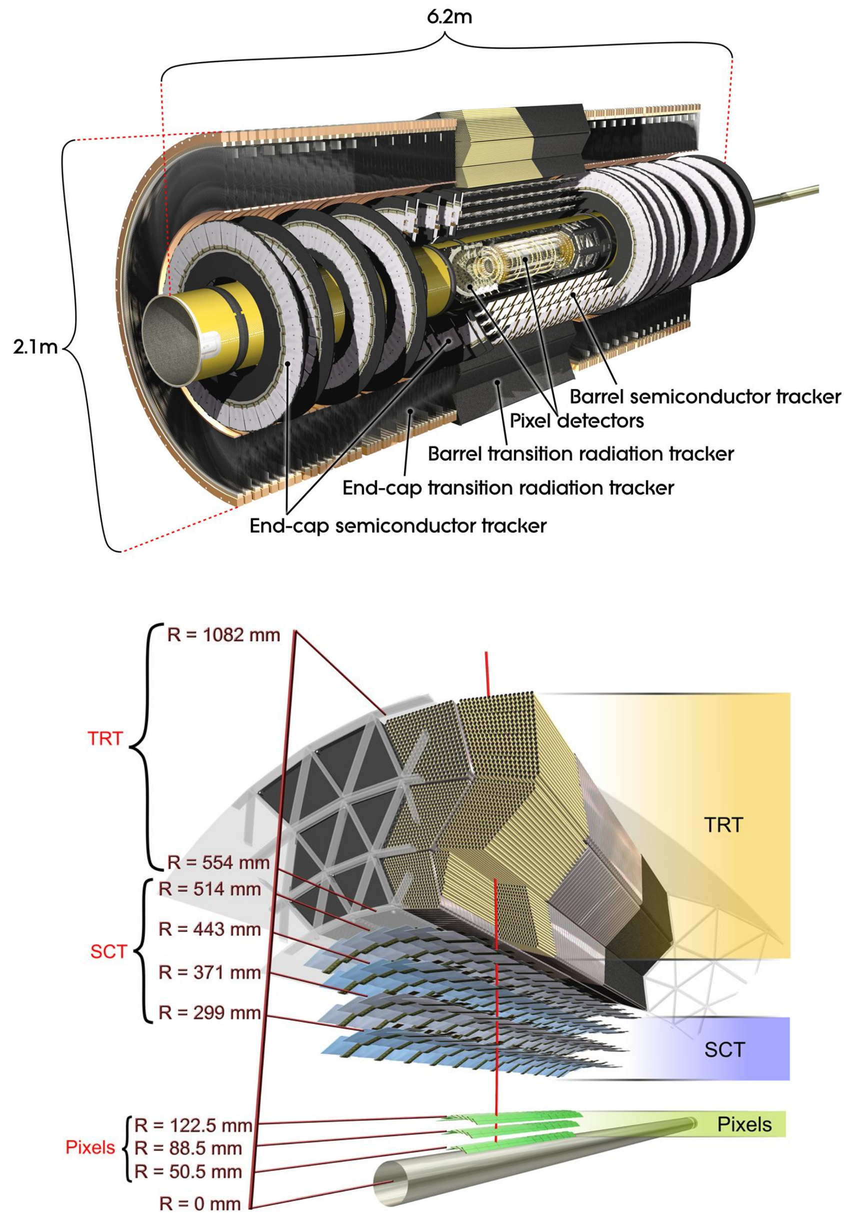

Figure 3.3: Illustration of the inner detector and its subsystems showing the layout of the barrel and endcap regions (top) and a more detailed illustration of the radial layout of the different subsystems in the barrel region (bottom).

3.2.2 The Calorimeter System

The ATLAS calorimeter, shown in Figure 3.4, is divided into two primary systems, the electromagnetic calorimeter and the hadronic calorimeter, and is responsible for measuring the energy of particles with the exception of muons and neutrinos. These measurements are crucial for both the identification and measurement of electrons and for the measurement of energy depositions from hadrons used to reconstruct jets. This is accomplished with three different technologies, all of which are broadly classified as non-compensating sampling calorimeters, meaning that energetic particles are showered using a dense passive medium (e.g. lead) and this shower is subsequently sampled with an active medium (e.g. plastic). However, since the entire shower is not collected, offline corrections are needed that relate the energy measured to the initial energy of the incident particle.

The electromagnetic calorimeter, responsible for measuring charged particles and photons, is situated directly outside of the ID and consists of a barrel portion, spanning $|\eta| < 1.475$, and two endcap portions that extend this coverage from $1.375 < |\eta| < 3.2$. Both portions consist of a cryostat containing a liquid argon (LAr) bath (active material) and an accordion like structure of lead (passive material). When a charged particle enters the detector, it either directly ionizes the LAr or in the case of a hadron, first showers in the lead and then ionizes the LAr. The electrons produced are then collected on readout cathodes and the collected charge is measured and calibrated to represent the total deposited energy in that calorimeter cell. A given cell is defined by the segmentation of the calorimeter, as shown in Figure 3.5. In the case of the the electromagnetic calorimeter, the full coverage is divided into three layers longitudinally and each layer is divided laterally by varying amounts, with 0.025×0.025 granularity in the first layer of the barrel. Before this calorimeter system, however, is a "presampler", which is a layer composed solely of the active LAr medium and is responsible to sample the shower created by detector material prior to the calorimeter itself and provides information used to better reconstruct the energy measurement.

The second calorimeter system is the hadronic calorimeter, which has a barrel and endcap portion, and is responsible for measuring hadrons that are either neutral, and so do not interact in the electromagnetic calorimeter, or otherwise produce a shower that extends beyond the electromagnetic calorimeter. The barrel portion of the system, called the tile calorimeter, is situated directly outside of the electromagnetic calorimeter and covers the region of $\eta < 1.7$. It is composed of alternating tiles of iron (passive material) and plastic (active material) as shown in Figure 3.5. The shower is initiated in the iron tiles and converted to light by the plastic tiles. This light signal is transmitted via optical fibers to a PMT that amplifies the signal and converts it to an electrical signal which is read out and calibrated for each cell. As with the electromagnetic calorimeter, a cell is defined based on the segmentation of the calorimeter. In the tile calorimeter, this segmentation divides the subdetector into three longitudinal layers in addition to lateral layers which are roughly 0.1×0.1 in $\Delta\eta \times \Delta\phi$. The endcap portion of the hadronic calorimeter, extending coverage to $|\eta| < 3.2$, operates on the same principle as the liquid argon electromagnetic calorimeter, ionization of active liquid argon, but implements copper plates to promote showering of hadrons.

Three attributes pertaining to this calorimeter system directly translates into an increase in physics performance in this search. The first is its ability to stop the outgoing energetic particles and thus fully contain and measure their energy. For the electromagnetic calorimeter, the first quality criteria is characterized by the number of radiation lengths[3] which ranges from 20 and 30 depending on η. For the hadronic calorimeter, this same metric is characterized by the number of interaction lengths, which is approximately 7 for the central portion of the tile calorimeter. These figures are sufficiently high that energetic particles are fully contained and measured in the calorimeter and the probability of punch through, the escape of an energetic hadron into the muon spectrometer, is very low. The second is the excellent energy resolution. Due to the sampling nature of the calorimetry it varies as a function of energy, decreasing at higher energy due to a larger number of particles being sampled in a larger shower, and is $\sigma/E \sim 10\%/\sqrt{E} \oplus 0.17\%$ for the electromagnetic calorimeter and $\sigma/E \sim 50\sqrt{E} \oplus 3\%$ for the hadronic tile calorimeter. Lastly, the longitudinal and lateral segmentation of both systems allows for the calibration of showers from different types of objects and the measurement of shower shapes for improved particle identification. This is essential both in the identification and measurement of electrons and the construction and calibration of topoclusters (described in Section 5.3.4) used to construct jets.

3. A radiation length is a measure of the thickness of material with respect to the electromagnetic force in terms of the number of times a charged particle radiates while passing through the calorimeter. An interaction length is defined similarly, but with respect to the strong nuclear force.

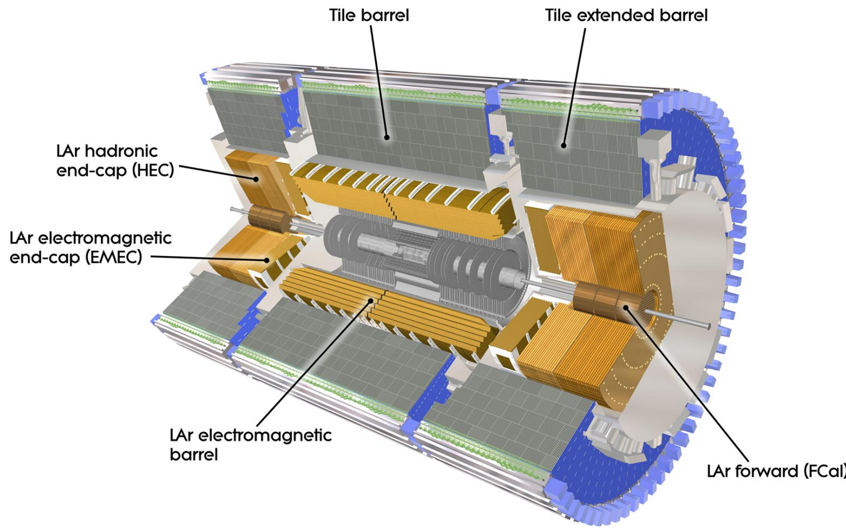

Figure 3.4: A schematic overview of the subsystems of the electromagnetic and hadronic calorimeter systems in the ATLAS detector.

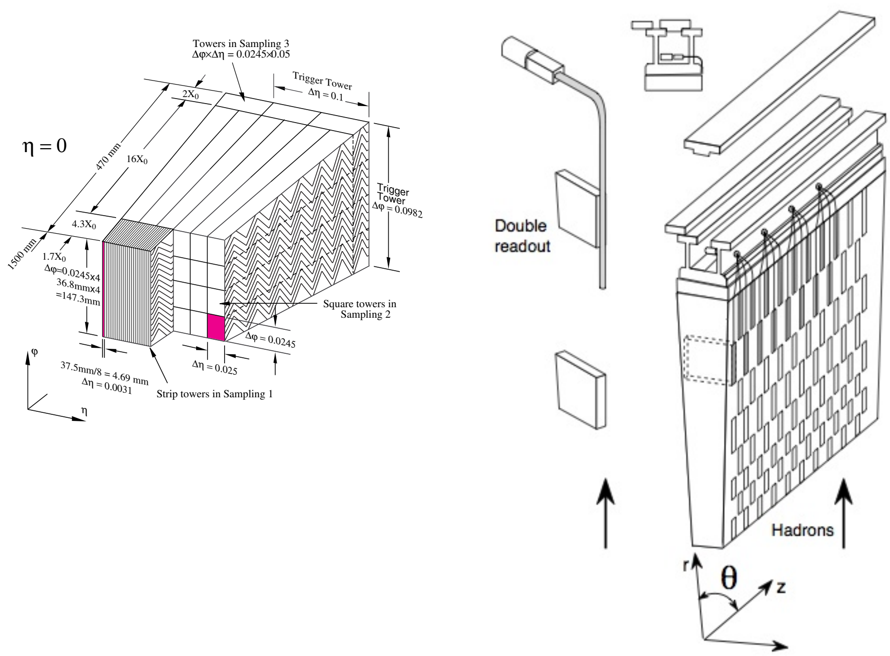

Figure 3.5: Schematic designs of the liquid argon electromagnetic calorimeter (left) and hadronic tile calorimeter (middle). Not shown here is the liquid argon hadronic endcap calorimeter which is very similar to the electromagnetic calorimeter in design principle, but using copper as an absorber to stop energetic hadrons.

3.2.3 The Muon Spectrometer

The muon spectrometer (MS), shown in Figure 3.6, is the outermost subdetector and is responsible for identifying muons and measuring their momenta. It consists of a toroid magnet and three layers of tracking chambers, based on four different technologies, to register hits from passing muons. The principle of operation is similar to that of the ID for reconstructing tracks but since the magnetic field is toroidal, the induced bending of charged muons occurs in the (r, z) plane. In addition to reconstructing muons offline, specialized components of the MS provide fast registering of muon hits which is crucial in for the initial trigger identification of events containing muons.

The four technologies implemented in the MS are resistive plate chambers (RPC), thin gap chambers (TGC), cathode strip chambers (CSC), and monitored drift tubes (MDT). All of these technologies operate in a similar way, by collecting charge produced from the ionization of a gaseous mixture by the passing of a muon. However, the manner in which the charge is collected is what differentiates the technologies and defines their specific application. The RPCs, used in the barrel region, collect the ionized charge on two parallel resistive plates separated by a small gap. This configuration is operated in an avalanche mode that allows for fast readout, and therefore triggering capabilities. The TGC technology, implemented in the endcap region, consists of a gap between two conducting cathodes which contains a set of parallel wires which collect ionized charge. This allows for fast readout for triggering but can further be used in the reconstruction of muons given the good spatial resolution provided by the wires. The CSCs, instrumented throughout the muon system, operate in the same manner as the TGCs but with a reduced spacing between wires. Lastly, the MDTs are constructed similarly to the TRT straw tubes and are instrumented throughout the system. This collection of subsystems provide muon triggering and identification out to $|\eta| < 2.7$.

Two features of the MS are noteworthy for this search. First, the large radius of the MS provides a long lever arm over which the muon reconstruction is performed which in turn leads to increased precision in the measurement of the muon momenta, especially at large momenta. Second, due to the MS being the outermost subdetector of ATLAS, space is required for services leading to the calorimetry and ID and therefore there is a gap in the central portion of the MS that is uninstrumented with RPCs and which leads to a decrease in the acceptance of muon triggers as described in Section 5.2.

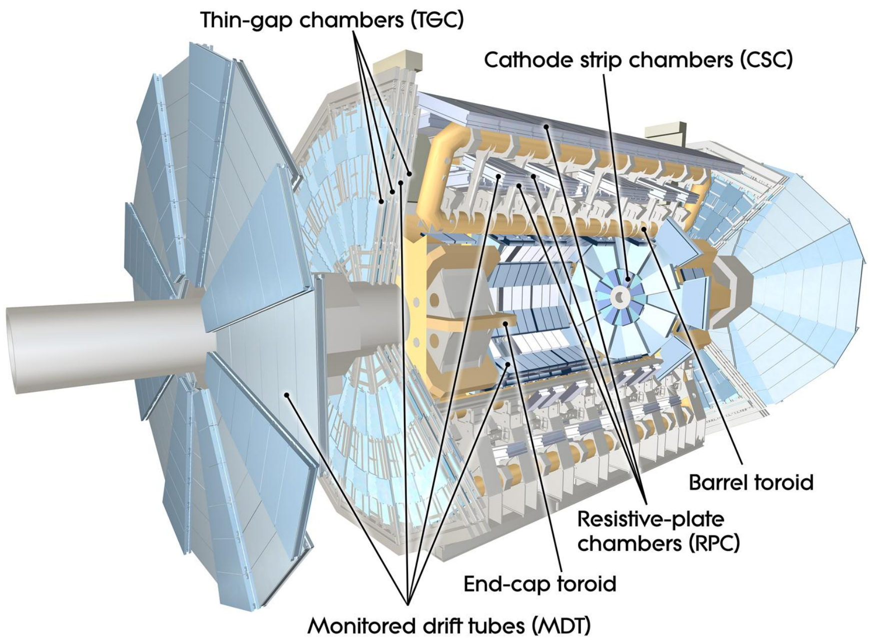

Figure 3.6: Schematic illustration of the muon spectrometer system in the ATLAS detector, the main components of which are the detector panels and toroid magnets.

Chapter 4

Jets, Substructure, and Boson Tagging

4.1 Building Jets

The study of hadronically decaying W and Z bosons requires the reconstruction of final states involving quarks. However, because the theory of quantum chromodynamics, which describes the interactions of quarks and gluons, is strongly coupled at low energies, no independent parton with a net color charge can be independently observed [32]. Therefore, unlike electrons and muons, which traverse a large fraction of the detector leaving a relatively clean signature of their presence, a parton emitted from a process can propagate for only a few fermi. The strong coupling of QCD then causes the parton to readily radiate gluons and create $q\bar{q}$ pairs from the vacuum. This process of splitting, called the parton shower, continues as shown in Figure 4.1 [33] until the energy scale of the partons approaches $\Lambda_{QCD} \sim 0.2$ GeV. At this point, the color connections between the low energy partons cause them to condense into stable hadrons, through the non-perturbative process of hadronization. These hadrons continue into the detector and are reconstructed as collimated sprays of charged and neutral hadrons known as "jets".

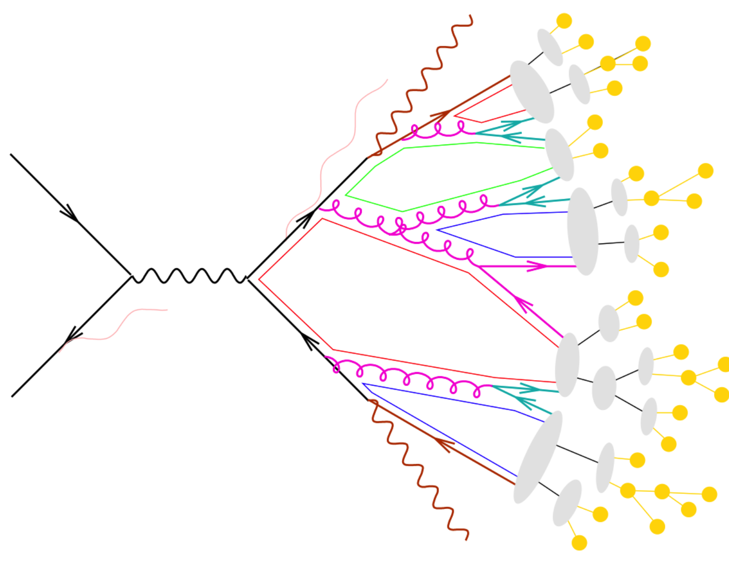

Figure 4.1: Illustration of the decay of a W or Z boson to a $q\bar{q}$ pair with the subsequent dynamics of the parton shower (red and purple lines) and hadronization (gray clusters and yellow circles) of the hard partons.

Quantum chromodynamics is a strongly coupled theory and so the Feynman diagrams that emerge from considering the cascade of a single energetic parton to a jet are intractable to direct calculation. However, it can be shown that given an n leg diagram ($\mathcal{M}_n$), the $n+1$ leg diagram ($\mathcal{M}_{n+1}$) formed by including an additional contribution from a parton splitting ($a \to bc$), as shown in Figure 4.2, scales as:

$$|\mathcal{M}_{n+1}|^2 \sim \frac{1}{\theta^2} C_A F(z) |\mathcal{M}_n|^2 \tag{4.1}$$

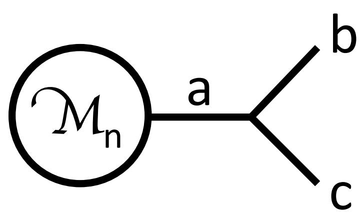

Figure 4.2: The Feynman diagram representing an $n+1$ leg matrix element process $\mathcal{M}_{n+1}$, build from an n leg process $\mathcal{M}_n$ and an additional parton splitting.

where $z = \frac{E_b}{E_a}$ is the relative energy of the more energetic parton after the splitting to that of the initial parton and θ is the opening angle of the splitting between parton b and parton c. There are three key features that emerge from this equation that dictate the first order evolution of jets. The first concerns the function $F(z)$, related to the abc splitting vertex and depends whether the vertex is a ggg, qqg, or gqq vertex. For the gqq vertex, this function is well defined for all values of z but for the ggg and qqg vertices a singularity exists for an emission of $z = 0$ or $z = 1$, meaning that radiation coming from these splittings are preferentially low energy, "soft". Second, the $1/\theta$ singularity common to all vertices implies that splitting are preferentially at small angles, "collinear". The third key feature is that in addition to the soft and collinear nature of the splittings, the splittings do not depend on the azimuthal angle around the axis of propagation of parton a. These three features lead to the intuition that the resulting hadronization pattern coming from a parton produced in the matrix element will generally be azimuthally symmetric around the initial direction of the parton with a hard central core of energy and some amount of less energetic radiation distributed rather evenly around it.

Indeed, this is the signature that is used to identify jets as collimated sprays of hadrons. To make this identification, analyses at the LHC typically use a set of infrared and collinear safe algorithms called sequential recombination algorithms that take as input a set of all the objects identified as final state particles p_i in an event and produce a set of jets, which are discrete sets of these initial particles [1]. The generic recombination algorithm requires two parameters, the *constituent-constituent* distance d_{ij} and the *constituent-beam* distance d_{iB}. The algorithm then proceeds as follows:

1. Calculate the constituent-constituent distance for all possible combinations of particles in the initial set.
2. For the pair that has the smallest d_{ij} [1], compare this distance to d_{iB}.
3. If the $d_{ij} < d_{iB}$, combine constituents i and j into a common constituent by adding their four vectors and return to step (1).
4. If the $d_{ij} > d_{iB}$, define constituent i as a jet, which may itself be a collection of multiple constituents from previous combinations.

This process is repeated until the entire set of initial constituents has been grouped into separate collections, which compose the set of jets in the event. The manner in which this clustering occurs depends critically on the constituent-constituent and constituent-beam distances chosen. Three primary choices for these distances are in common use and can be broadly categorized by

$$d_{ij} = min({p_T}_i^{\,n}, {p_T}_j^{\,n})\frac{{\Delta R_{ij}}^2}{R^2} \tag{4.2}$$

$$d_{iB} = {p_T}_i^{\,n} \tag{4.3}$$

and are distinguished by the choice of n and R. The parameter R roughly corresponds to the radius of the jet in (η, ϕ) space and the choice of n governs the extent to which the momenta of constituents are taken into account when building the jet. In particular, the choice of $n = 2$ corresponds to the "k_t" algorithm, $n = 0$ corresponds to the "Cambridge-Aachen" (C/A) algorithm, and $n = -2$ corresponds to the "anti-k_t" algorithm.

To gain an appreciation of the extent to which the jets found by these three different algorithms differ in structure, shown in Figure 4.3 is an image of the same event clustered

1. The measurement of separation of any two objects in an event, in this case two jet constituents ΔR_{ij} used to define the d_{ij} distance, is defined in (η, ϕ) to be $\Delta R = \sqrt{\Delta\eta^2 + \Delta\phi^2}$

with these three algorithms. The grid roughly corresponds to the size of typical calorimeter cell segmentation and the different colored regions indicate which cells correspond to the different jets. It is evident from this that the anti-k_t algorithm is advantageous as it defines jets with structure that corresponds to the physical intuition obtained from the parton splitting functions, namely that anti-k_t jets are circular. Furthermore, they are initially defined by a constituent pair with high energy, most likely coming from a hard scattering process, and so are robust against soft radiation. Therefore, the anti-k_t algorithm is ideal to use to define physical objects as proxies for quarks and gluons in LHC collisions.

The other two algorithms, k_t and C/A, do not exhibit these characteristics and so are not used to reconstruct parton proxies. However, the feature that both of these have is that the order in which the clustering of the initial jet constituents into a final jet occurs follows an ordering that attempts to mimic that which would be obtained if one were to invert the hadronization and showering of the final state particle. For the C/A algorithm, the assumption is made that stable hadrons formed from nearby splittings will be close to one another and so the ordering is done relying only on the proximity of constituents in (η, ϕ). The k_t algorithm takes this a step further and relies on the added information that these final hadrons will be low energy as well, as would be the final state hadrons that cascade down in energy from the initial hard parton. This feature of defining a physically sensible reconstruction sequence is of the utmost importance in exploring the internal dynamics of the jet and providing the tools that allow for jets to be viewed as proxies for not only energetic partons but also massive objects such as W and Z gauge bosons.

Lastly, it is of great importance to note that all three of these algorithms exhibit the characteristic that they are infrared and collinear safe. This means that the result of the algorithm, the set of jets found, is unaffected by the presence of additional soft radiation or additional collinear splittings in the shower. This radiation may come from actual splittings in the showering process, which are inherently soft and collinear, or additional pileup collisions. This condition further applies to all observables calculated for these jets including, in addition to the components of the four vector of the jet, the additional set of observables described in Section 4.4.2 that examine the substructure of the jet and is necessary to allow for the stable and consistent identification and measurement of jets.

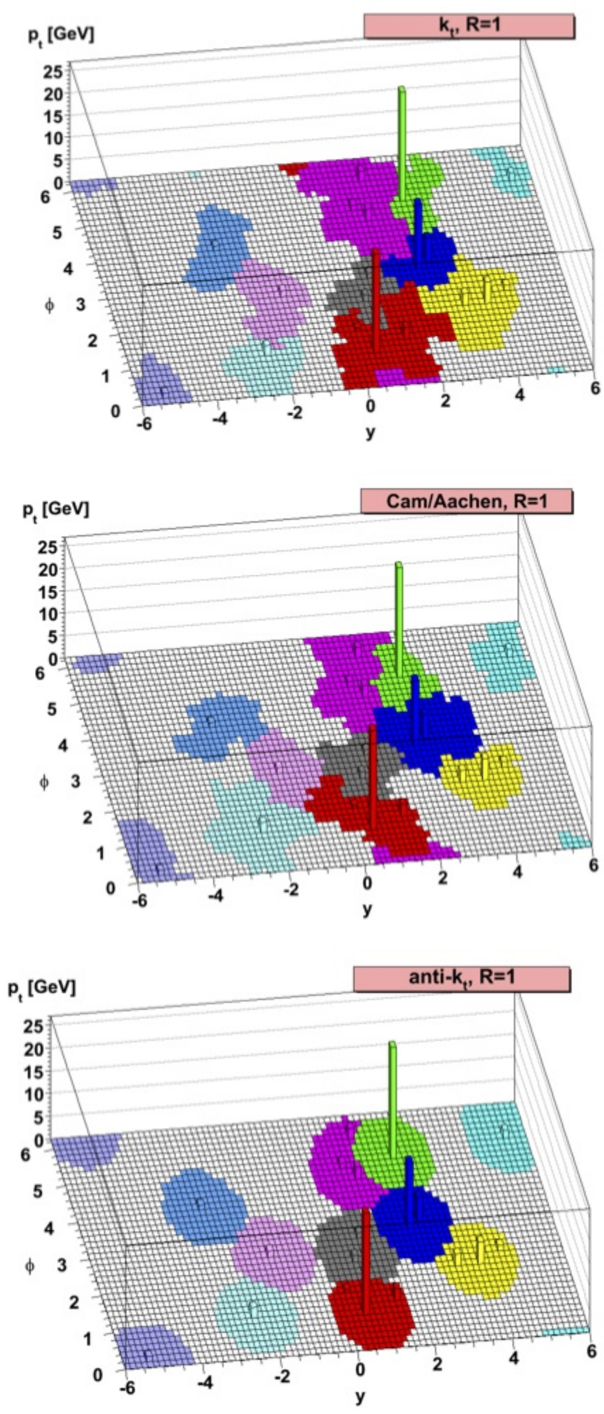

Figure 4.3: From [1], the reconstruction of the same multijet event in the (η, ϕ) plane using the anti-k_t, k_t, and C/A jet algorithms for the clustering of constituents. Of note are the differences in the general shape of the jets built using these different procedures.

4.2 "Fat" Jets

Due to the high energies at the LHC, regions of phase space are becoming accessible to measurements where massive objects (e.g. W/Z bosons) are heavily boosted, meaning that their transverse momentum is several hundred GeV or more. From basic kinematics, the spatial separation $\Delta\theta$ between two massless objects, namely quarks, resulting from the decay of a boosted massive object X

$$\Delta\theta(q\bar{q}) \sim \Delta R(q\bar{q}) \sim \frac{1}{\sqrt{z(1-z)}}\frac{M(X)}{p(X)} \rightarrow \Delta R_{min}(q\bar{q}) \sim \frac{2M(X)}{p(X)} \tag{4.4}$$

where z is the momentum fraction of higher p_T decay product. Therefore, for particles with $M(X) \sim 100$ GeV (e.g. W/Z) and a momentum of $p(X) \sim 300$ GeV gives an angular separation of $\Delta R \sim 0.6$. In ATLAS, the standard anti-k_t jet reconstruction algorithm used to reconstruct partons uses a jet radius of $R = 0.4$. Therefore, the two jet cones begin to overlap and the identification of jets associated to individual partons becomes increasingly difficult and ambiguous. This can lead to difficulties in correctly reconstructing the true hard collision given that one of these jets may be discarded if it does not pass the experimental selection requirements placed on jets. Furthermore, from an experimental standpoint, it can lead to difficulties in understanding the calibration of these individual jets due to topological dependencies in the calibration and possible associated uncertainties. Therefore, when the desired final state involves such a boosted object, it is advantageous to view the final state set of associated hadrons not as belonging to two separate jets but rather to a single jet, representative of the initial object, the W/Z boson. To fully accommodate the decay products of the boosted object, the jet radius is thus increased. The extent to which the jet radius is increased will affect the energy regime at which this merging occurs and is thus process dependent. Typically, increasing the radius to larger values ensures that the full energy of the hard decay and associated final state radiation is contained within the jet cone and so a single W or Z boson can be reconstructed in that single jet, as shown in Figure 4.4 for a sample of W bosons. However, pileup collisions contribute to the set of constituents that are clustered into a given jet and, because energy depositions from pileup are rather uniform in distribution, leads to an increased affect for larger jet radii.

To counteract the effect of pileup, and better define the jet to be the set of hadrons associated to a jet requires that the jet not be viewed as a single vector, constructed as the

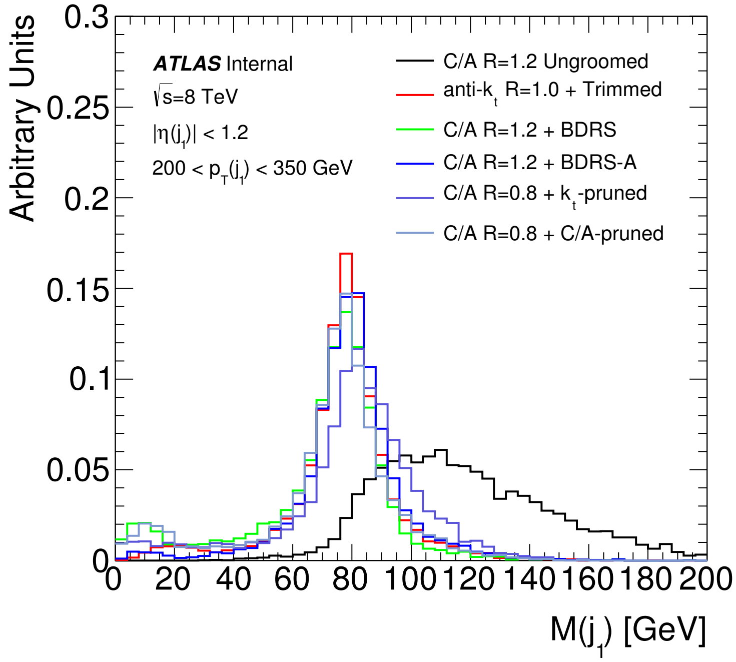

Figure 4.4: From simulation, a comparison of the leading jet mass, constructed from topoclusters, described in Section 5.3.4, for a high-p_T W boson jet for the Cambridge-Aachen jet algorithm with R=1.2 and several alternative algorithms and grooming procedures described in Section 4.3 intended to mitigate the effects of pileup.

vectorial sum of its constituents, but rather the full set of constituents themselves. This set contains a wealth of information and the study of how to define that set and more carefully understand and subsequently exploit the properties of it in searches for new physics has come to be known as the field of *jet substructure*. The study of jet substructure was first proposed in the early 1990's [34] but received little attention until 2008 when it was proposed as a possible means by which to allow for improvements in the search for $H \to b\bar{b}$ at the LHC [35]. During the course of Run 1 of the LHC, much attention has been given to studying jet substructure both from the theoretical standpoint [36] and by the ATLAS and CMS experiments from the experimental point of view [37–40]. It has focused on a number of topics related primarily to the identification of boosted top quarks and boosted W/Z and H bosons and this thesis contextualizes it as a tool to identify hadronically decaying W and Z bosons, "boson jets", for subsequent use in the search for decays of massive, $M(X) > 1$ TeV, diboson resonances.

To understand how jet substructure is used to achieve this goal, it can be understood as divided into two main pieces; jet finding/grooming and jet tagging.

1. **Jet Finding/Grooming** : This is the initial step of jet finding where a set of constituents are defined according to one of the aforementioned jet algorithms (k_t, anti-k_t, and C/A) and then certain constituents are removed, groomed away, according to some criteria to derive a final set of constituents, representative of the heavy particle [2].

2. **Jet Tagging** : This second stage of substructure analysis takes the previously defined set of jet constituents and forms jet moments, functions of the four momenta of the constituents, which can be used as discriminating variables to differentiate jets coming from the decay of a heavy particle from those originating from an energetic parton.

4.3 Jet Finding/Grooming

Following the initial step of jet finding, a jet is defined as a set of four vectors, intended to be representative of stable hadrons. These hadrons may not all come from the intended target, the boosted object, and in particular there may be contributions from initial state radiation, pileup, and multi parton interactions that lead to a degradation of the resolution of the properties of the jet. Jet grooming is the application of an algorithm intended to recover the resolution of the jet and better define the constituents as those from the interesting boosted physics object. There are three main types of jet grooming (splitting and filtering, trimming, and pruning) which are presently in wide use and from these, five variations are studied in greater detail for application in this search and for use by other ATLAS analyses using the identification of boson jets during Run 1 of the LHC [2].

4.3.1 Splitting and Filtering

The first class of jet grooming studied is that of splitting and filtering [35]. The colloquial name used by the community is that of "BDRS", representing the initials of the authors of the paper. The algorithm was initially developed in the context of searching for the associated

2. Note that the removal of a jet constituent can be viewed as a binary decision that weights the four vector of the constituent with a weight or 0 or 1. Certain types of jet substructure, namely jet *cleansing* [41], explore the possibility of the more general approach to simply down-weight the contribution of the constituent. The study of this is out of the scope of this thesis.

production of a Higgs boson with a W or Z boson with the subsequent decay of $H \to b\bar{b}$. Therefore, it is somewhat focused on fat jets with primarily two-body-like substructure and is useful for W/Z tagging as well.

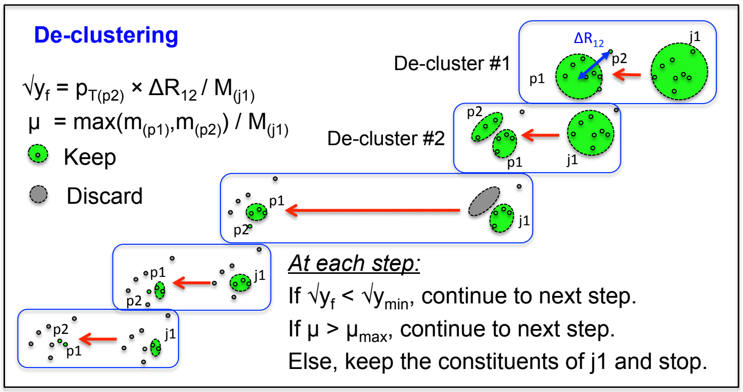

Figure 4.5: From [2], an illustration of the mass-drop / momentum-balance technique utilized by the BDRS and BDRS-A algorithms for identifying jets with hard substructure. The de-clustering is performed by running backwards the history of the clustering algorithm, until it finds a recombination that contains a mass drop (μ_{max}) between the initial jet and the more massive of the subjets and those two subjets are balanced in transverse momentum ($\sqrt{y_{\mathrm{f}}}$). The BDRS algorithm requires $\sqrt{y_{\mathrm{f}}} \geq 30\%$ and $\mu_{max} = \frac{2}{3}$. The BDRS-A algorithm requires $\sqrt{y_{\mathrm{f}}} \geq 20\%$ and makes no requirement on the mass-drop, $\mu_{max} = 1$.

The canonical BDRS jet grooming method decomposes jets, formed with the C/A algorithm which provides a clustering sequence which attempts to invert the parton shower and a distance measure of $R = 1.2$, works backwards through the clustering steps to search for hard structure within the large-R jet. The jet J at a given stage of the cluster history is decomposed into two subjets: j_1 and j_2, as in Figure 4.5. If there is a significant mass drop, defined as $\mu_{12} = \frac{\max(m(j_1), m(j_2))}{m(j_1+j_2)}$, and the momentum is balanced, defined with the parameter $\sqrt{y_{\mathrm{f}}} = \frac{\min(p_{\mathrm{T1}}, p_{\mathrm{T2}})}{m_{12}} \Delta R_{12}$[3] , then the parent jet is presumed to represent a hard decay and the procedure ends by returning this jet and defining the subjet distance scale R_{12} in that recombination which will be used in the further filtering stage. In particular, the choices for these parameters are taken from [35] and are $\mu_{12} < \mu_{max} = 2/3$ and $\sqrt{y_{\mathrm{f}}} > 0.3$. If the cuts fail then the highest mass subjet is taken as the new parent jet and the procedure continues. If this iterative splitting stage eventually identifies a boson-like recombination, the remaining jet constituents are then filtered. The filtering step, illustrated in Figure 4.6,

3. The angular separation of objects i, j in the (y, ϕ) space is defined as $\Delta R_{ij} = \sqrt{(y_i - y_j)^2 + (\phi_i - \phi_j)^2}$.

attempts to remove the radiation not belonging to the last three subjets in the clustering process, thus allowing for the two daughters of the hard decay and one hard final state emission. This is carried out by reclustering the remaining constituents using the anti-k_t algorithm with a distance parameter of $R_{\text{subjet}} = \min(0.3, R_{12}/2)$ where R_{12} is the angular separation of the splitting identified in the previous stage. The three hardest subjets found by this method are recombined and form the final boson-tagged jet. This configuration of jets has been studied in depth in ATLAS [42] and was found to perform quite well.

The modified BDRS tagger, referred to here as "BDRS-A" and studied to a greater extent in [43], follows the same procedure as the original BDRS tagger, initially finding jets with the C/A algorithm and a distance metric of $R = 1.2$. However, the splitting and filtering process has three modifications that are intended to be more optimal for particularly high-p_T boson jet identification, beyond the regime originally studied in [35]. The modification made are

1. The mass drop requirement is removed in the splitting stage as it was found to not remove any fake QCD jets that would not be removed by the momentum balance requirement

2. The momentum balance cut is loosened to the value of $\sqrt{y_{\text{f}}} > 0.2$. This ensures that a larger fraction of signal jets, predisposed to reside at high values of $\sqrt{y_{\text{f}}}$, pass the requirement. Furthermore, QCD jets tend to accumulate along the boundary of this requirement and so moving it to lower values causes there to be larger separation between signal and background in this measure which can be used to make a post-selection requirement.

3. The subjet radius used in the filtering stage is fixed to be $R = 0.3$ to ensure that very high-p_T, collimated decays will not lead to reclustering with a distance measure finer than the granularity of the calorimeter.

It is important to note that the loosening of the momentum balance cut will cause a greater contamination of QCD jets which are not fully decomposed and rejected by the algorithms. Therefore, it is intended that a selection requirement be made on $\sqrt{y_{\text{f}}}$ after the initial splitting stage that is tuned for a given analysis. The effect of not having this requirement is made apparent when examining the comparison of signal W boson jets with QCD jets in Figure 4.4, in which the spectrum composed of large R, ungroomed jets has been pushed to higher masses and broadened. However, upon applying grooming, the W boson mass is restored and the resolution improved.

4.3.2 Trimming

The second type of jet grooming studied is that of trimming [44]. Although it is widely used to study boosted massive objects, the initial motivation to study trimming arose from working to better reconstruct jets as proxies for hard partons. It is well understood that in a clean Monte Carlo event, one with no pileup interactions or multi parton interactions (MPI) obscuring the event reconstruction and in which initial state radiation (ISR) has been artificially turned off, the reconstruction of jets as parton proxies is benefitted by using the circular anti-k_t algorithm and increasing the jet radius to a value of $\sim$1.0 to capture the full extent of final state radiation (FSR) from the parton shower. However, the gains acquired by doing this are washed out when pileup, MPI, and ISR are turned back on. To mitigate these effect and attempt to restore the jet to its definition that only includes the final state radiation, an algorithm is employed that attempts to identify uncharacteristically soft radiation within the jet and remove it. To achieve this, the initial fat jet is reclustered into smaller subjets using the k_t algorithm with some smaller subjet radius (R_{subjet}). Some of these subjets are discarded if they are determined to be too soft as shown in Figure 4.6. The choice of the definition of *soft* is defined by two parameters, the energy scale of the process (Λ_{hard}) and the threshold relative to this Λ_{hard} that is considered soft (f_{cut}). The definition of Λ_{hard} was studied in [44] and found that using the initial fat jet p_T is an acceptable choice. Therefore, jet constituents are trimmed away if they belong to subjets with $p_T(subjet) < p_T(jet) \times f_{cut}$.

The particular implementation of trimming was studied here initially finds anti-k_t, $R = 1.0$ jets and then applies trimming with $f_{\text{cut}} = 5\%$ and $R_{\text{subjet}} = 0.3$. These parameter choices were determined through extensive studies in ATLAS at $\sqrt{s} = 7$ TeV [42] and were found to be effective at uncovering hard substructure and stable with respect to varying pileup conditions.

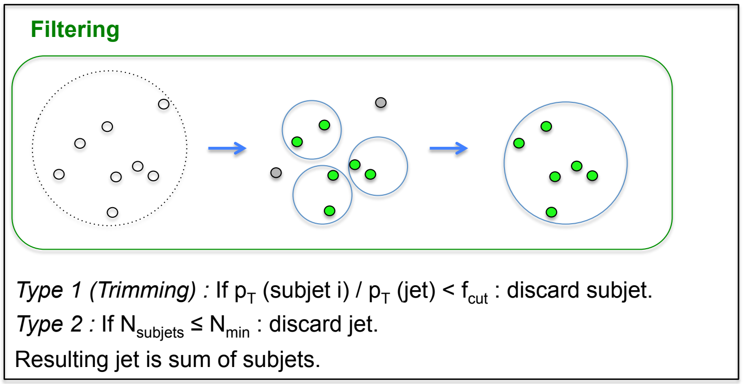

Figure 4.6: From [2], an illustration of the filtering and trimming procedures. Filtering is used here as part of the BRDS and BDRS-A algorithms, each requiring a minimum of three subjets reconstructed with $R_{subjet} = min(0.3, \Delta R/2)$ and $R_{subjet} = 0.3$ respectively. Trimming is used here with $f_{cut} = 5\%$ and $R_{subjet} = 0.3$.

4.3.3 Pruning

The third class of jet grooming that is explored is that of pruning [45]. Unlike splitting/filtering and trimming, jet pruning does not rely on reclustering a jet's constituents into subjets. Instead, it relies on rebuilding the jet using the sequence that is initially defined by the jet finding and examining each combination in the building procedure to remove pileup contributions. As illustrated in Figure 4.7, when a possible jet constituent combination is determined at a given stage in the sequence for jet constituents j_1 and j_2, two parameters are calculated; $z = \frac{min(p_T(j_1), p_T(j_2))}{p_T(j_1+j_2)}$ and $\Delta R(j_1, j_2)$. These two parameters are used to identify a given piece of radiation as being attributed to the parton shower and hadronization of the hard decay of the boosted object, or coming from pileup, ISR, or MPI which primarily consists of soft, wide-angle emissions. Therefore, for a given stage in the clustering, two conditions are checked; $z < z_{cut}$ and $\Delta R(j_1, j_2) > d_{\rm cut}$. If the pair of jet constituents fulfills both of these conditions, then the softer component is assumed to be from pileup and is discarded and the jet building proceeds with the remaining set of constituents. This procedure proceeds until all constituents are clustered into a final pruned jet.

Two versions of this algorithm have been studied by both ATLAS and CMS. The first begins by finding C/A, $R = 0.8$ jets with a combination sequence defined with the C/A algorithm and pruned with $d_{cut} = m^J/p_T^J$ and $z_{\rm cut} = 0.1$. This is the grooming algorithm found to perform the best in [40] for the purposes of W-tagging, and has also been used

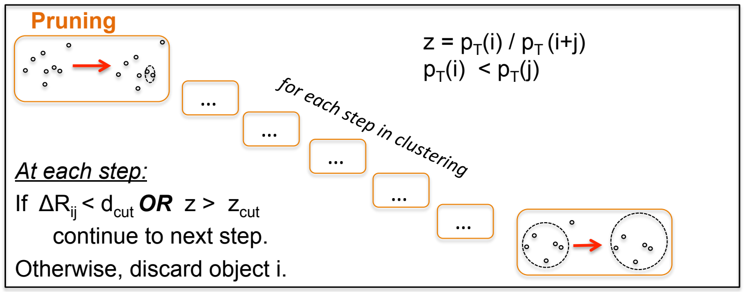

Figure 4.7: From [2], an illustration of jet pruning. The re-clustering of the jet constituents can proceed via either of the C/A or k_t algorithms; both are studied here.

by ATLAS for the Q-jets analysis [46]. The second type of pruned jets investigated starts with C/A, $R = 0.8$ jets with a clustering sequence redefined using the k_t algorithm and then pruned with $d_{cut} = m^J/p_T^J$ or $z_{\mathrm{cut}} = 0.1$. This is the variation of pruning that has been previously studied in detail in Ref. [42].

4.4 Tagging Boson Jets

The identification of boson jets requires using the jet substructure information obtained by examining additional information from the full collection of jet constituent four-vectors in ways that probe unique properties of the hard decay of the boson to distinguish it from the canonical QCD jet described in Section 4.1. This can be approached by breaking the problem into two pieces. The first is studying the jet mass, which itself comes from the square difference between the energy and momentum of the jet and provides a significant fraction of the discrimination between boson jets and QCD jets. The second step is to probe finer details of splittings and radiation patterns contained in the jet to find additional characteristics that can be used as distinguishing handles. Lastly, it is possible to imagine combining all possible information in a machine learning algorithm to produce optimal results for discrimination.

Extensive studies were performed in [2] using Monte Carlo to determine the optimal combination of jet finding and grooming along with selection criteria on jet mass and other substructure moments that give good discrimination power. These studies were performed using a sample of W boson jets derived from semi-leptonic decays of bulk Randall-Sundrum gravitons (G^*) as $G^* \to W^+W^- \to \mu\nu q\bar{q}$ and compared to a sample of QCD jets derived from Standard Model production of W+jets with the subsequent decay of $W \to \mu\nu$. The G^*

samples used for this study were produced over a wide range of masses to ensure that there exist sufficient statistics for a wide kinematic range in transverse momentum. These jets are required to be within $\eta < 1.2$ to ensure that the full set of jet constituents is contained within the inner detector and so can be reconstructed as a track jet as well, in order to define systematic uncertainties as described in Section 5.6.4. To further produce robust results and allow for meaningful performance comparisons between multiple jet algorithms, the Monte Carlo based analysis is performed in three kinematic bins defined by the transverse momentum of the leading C/A, $R = 1.2$ jet formed from stable truth hadrons ($p_T^{Truth} = [200, 350]$ GeV, $p_T^{Truth} = [350, 500]$ GeV, $p_T^{Truth} = [500, 1000]$ GeV). The comparison of performance can then be optimized for the kinematic region of a specific search. The general performance that is obtained is an overall rejection of background QCD jets of greater than 95% for a 50% signal efficiency for the kinematic regime of greatest interest.

However, these optimization studies would be remiss if the Monte Carlo tools used to model them did not model them well. Therefore, the understanding of the substructure of true boosted bosons, specifically W bosons is studied in data using a sample of very high-p_T, semileptonic $t\bar{t}$ events. This sample is initially collected by reconstructing the leptonic $t \rightarrow Wb \rightarrow \mu\nu + bjet$ signature and then requiring the event to contain a fat jet passing the HEPTopTagger selection [47]. When the kinematic region of interest is limited to $p_T^J < 350$ GeV, the boosted hadronic top decay contains a "partial merging" where the $W \rightarrow q\bar{q}$ is merged but the Wb system is not merged. This, therefore, provides a relatively clean sample in which to study the modelling of the jet substructure that eventually is relied on for sensitivity to new physics signals. The comparison of this sample to a sample of Monte Carlo events generated at next to leading order with POWHEG $t\bar{t}$ [48] shows that the data is generally modelled well by the Monte Carlo as in Figures 4.9, 4.11, 4.13 for the jet mass and in Figure 4.15 for a number of jet substructure moments, described in Section 4.4.2.

4.4.1 Jet Mass Discrimination

The first, and most powerful handle used to distinguish boson jets from QCD jets is the jet mass. This arises because of the manner in which jets acquire mass in QCD, through the emission of soft and collinear radiation, would cause a divergence at $M = 0$ GeV were it not for Sudakov form factors in the parton shower evolution that cause this divergence to be removed and the maximum to be shifted to a slightly increased mass. Boson jets, on the other hand, have an intrinsic hard splitting from the $W/Z \rightarrow q\bar{q}$ that produces a mass on the order of the $M_{W,Z}$. It was seen in Section 4.2 that the mass is greatly affected by contributions to the jet from additional sources of radiation. This causes the mass of QCD jets to migrate to higher values of mass, thus causing them to appear to be as massive as boson jets. Second, it causes the mass of the boson jets to increase beyond $M_{W,Z}$ and broaden significantly. By applying jet grooming and removing additional radiation not from the parton shower, two things are accomplished; the peak of the QCD jet spectrum shifts to a lower value, more consistent with the peak formed from the summation of all soft emissions from the QCD shower [49], and the boson jet signal is restored to the correct scale and increases in resolution.

The extent to which these two affects occur depends on the jet grooming that is applied, as can be seen in Figures 4.8, 4.10, and 4.12 for the five different jet finding and grooming configurations described in Section 4.3. To compare the effectiveness for one of these grooming algorithms to reject QCD jets in favor of W boson jets, which is critical in applying these methods in a search for new physics, the smallest possible window containing 68% of the signal jets is formed around the most probable value, defined as the maximum of the probability distribution function of the mass spectrum. The results for the most probable value, the width of this "optimal window", and the resulting background efficiency is given in Table 4.1. One important thing to note about this stage of defining a boson tagging prescription is that some jet algorithms, namely the BDRS algorithm, seems to outperform the other algorithms over a wide kinematic range. However, as noted before, there is still information contained in the distribution of jet constituents that can be used to further discriminate signal and background and this is the next step of determining a boson tag.

Jet collection	$200 < p_{\mathrm{T}}^{truth} < 350$ GeV		$350 < p_{\mathrm{T}}^{truth} < 500$ GeV		$500 < p_{\mathrm{T}}^{truth} < 1000$ GeV	
	$\mathcal{P}^{+U}_{-L}$ [GeV]	ϵ_{QCD}	$\mathcal{P}^{+U}_{-L}$ [GeV]	ϵ_{QCD}	$\mathcal{P}^{+U}_{-L}$ [GeV]	ϵ_{QCD}
Trimmed	82^{+10}_{-18}	$13.6 \pm 0.1\%$	80^{+8}_{-8}	$9.9 \pm 0.2\%$	82^{+10}_{-10}	$8.4 \pm 0.5\%$
BDRS	78^{+14}_{-16}	$14.8 \pm 0.1\%$	80^{+6}_{-18}	$7.8 \pm 0.2\%$	76^{+6}_{-14}	$6.7 \pm 0.5\%$
BDRS-A	78^{+12}_{-16}	$23.2 \pm 0.1\%$	82^{+8}_{-14}	$15.9 \pm 0.3\%$	80^{+10}_{-14}	$10.0 \pm 0.6\%$
C/A-pruned	78^{+22}_{-40}	$28.9 \pm 0.1\%$	78^{+8}_{-12}	$8.0 \pm 0.2\%$	78^{+6}_{-14}	$6.5 \pm 0.5\%$
k_t-pruned	84^{+22}_{-42}	$40.7 \pm 0.2\%$	82^{+16}_{-14}	$16.9 \pm 0.3\%$	82^{+18}_{-14}	$16.4 \pm 0.7\%$

Table 4.1: The most probable value of the signal mass distribution, $\mathcal{P}$ is given along with the upper (U) and lower (L) boundaries of the mass window that contains 68% of W jets for each jet algorithm. The boundaries of the sliding windows are rounded to the closest integer in GeV. The fraction of background jets in the mass window, ϵ_{QCD} is given with the binomial statistical uncertainty.

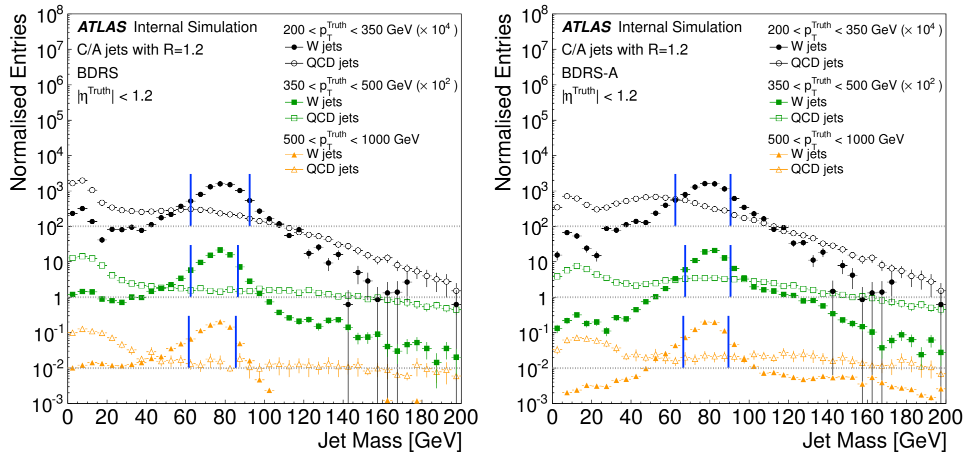

Figure 4.8: Calorimeter jet mass in signal and background reconstructed with the two splitting and filtering algorithms, BDRS (left) and BDRS-A (right). For both, the jet mass is shown in three p_{T} bins for signal (W jets) and background (QCD jets). Indicated on each distribution is the mass window containing 68% of the signal jets. The distributions are all normalized to unity and then offset from zero such that the distributions for the different p_{T} ranges are all visible.

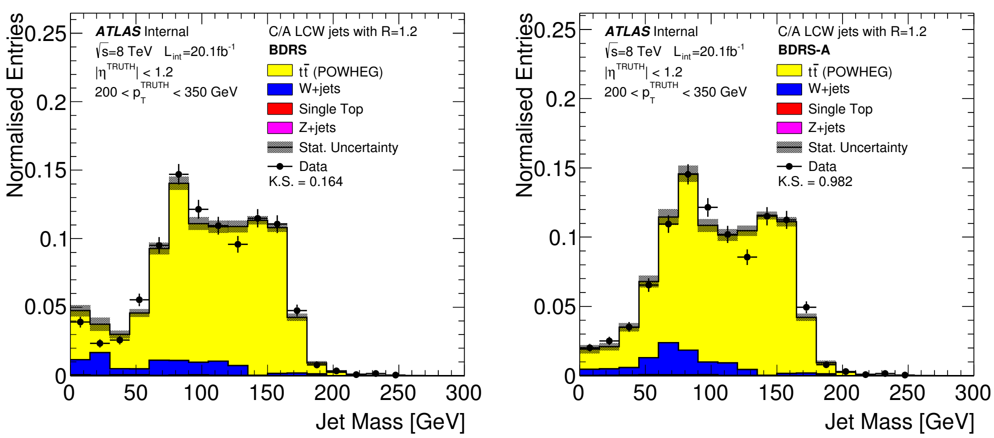

Figure 4.9: For the calorimeter jet mass with the two splitting and filtering algorithms, BDRS (left) and BDRS-A (right), the comparison of data to boosted $t\bar{t}$ signal Monte Carlo preselected with the HEPTopTagger in the regime of $200GeV < p_T(reco) < 350GeV$. This sample is chosen such that the hadronically decaying top is boosted to the extent that the $W \rightarrow q\bar{q}$ decay is fully merged, without the full merging of the Wb system.

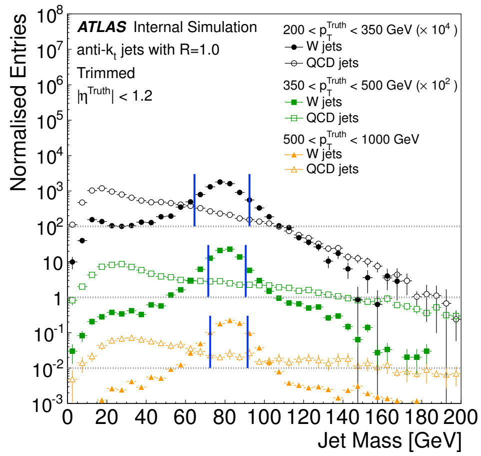

Figure 4.10: Calorimeter jet mass in signal and background reconstructed with the trimming algorithm. The jet mass is shown in three p_{T} bins for signal (W jets) and background (QCD jets). Indicated on each distribution is the mass window containing 68% of the signal jets. The distributions are all normalized to unity and then offset from zero such that the distributions for the different p_{T} ranges are all visible.

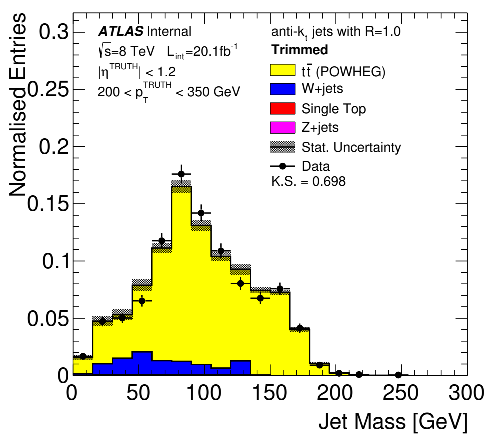

Figure 4.11: For the calorimeter jet mass with the trimming algorithm, the comparison of data to boosted $t\bar{t}$ signal Monte Carlo preselected with the HEPTopTagger in the regime of $200GeV < p_T(reco) < 350GeV$. This sample is chosen such that the hadronically decaying top is boosted to the extent that the $W \rightarrow q\bar{q}$ decay is fully merged, without the full merging of the Wb system.

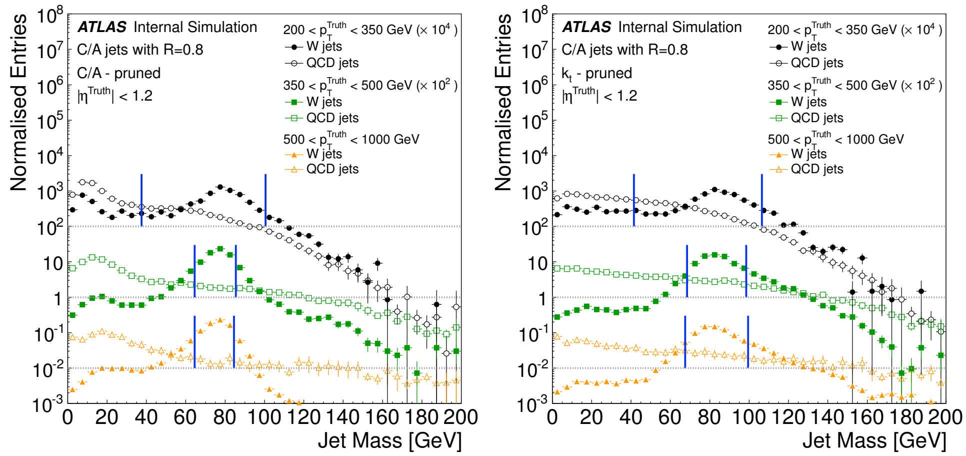

Figure 4.12: Calorimeter jet mass with the two pruning algorithms, C/A-pruning (left) and k_t-pruning (right). For each algorithm, the jet mass is shown in three p_{T} bins for signal (W jets) and background (QCD jets). Indicated on each distribution is the mass window containing 68% of the signal jets. The distributions are all normalized to unity and then offset from zero such that the distributions for the different p_{T} ranges are all visible.

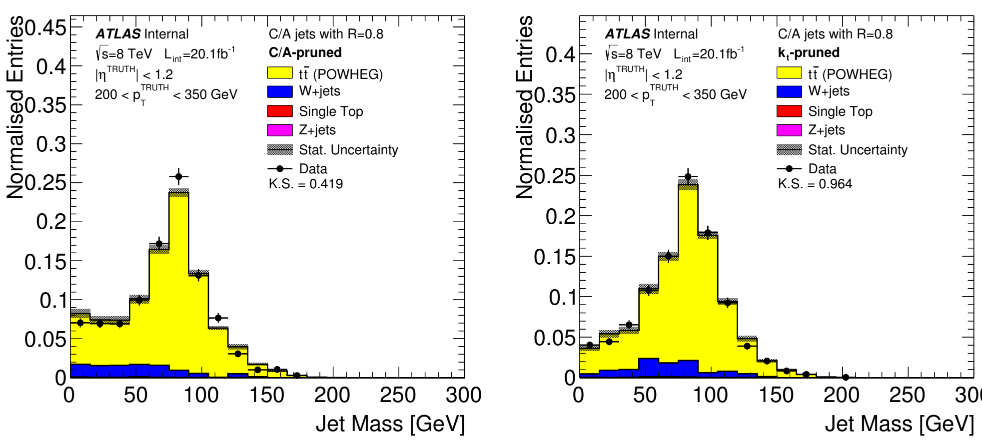

Figure 4.13: For the calorimeter jet mass with the two pruning algorithms, C/A-pruning (left) and k_t-pruning (right), the comparison of data to boosted $t\bar{t}$ signal Monte Carlo preselected with the HEPTopTagger in the regime of $200GeV < p_T(reco) < 350GeV$. This sample is chosen such that the hadronically decaying top is boosted to the extent that the $W \rightarrow q\bar{q}$ decay is fully merged, without the full merging of the Wb system.

4.4.2 Jet Substructure Moments

In addition to the jet mass, a number of jet moments, functions of the jet constituent four momenta, exist that parameterize the information contained in the full set of constituents in a way that allows for discrimination between boson jets and QCD jets. Much progress is being made to develop novel techniques to achieve this goal, develop new types of moments [50–52], and leverage existing jet moments to obtain optimal boson tagging [53]. For the studies presented here, a subset of seven jet substructure moments is considered. This is by no means exhaustive, but provides a first attempt in ATLAS implementing a broad number of techniques aimed at the same primary goal of hadronic W boson identification. These moments are summarized below.

- **Splitting scale** [54] The splitting scale, $\sqrt{d_{12}}$, is calculated for a jet (re)clustered with the k_t-clustering algorithm, and is the k_t distance between the two proto-jets of the final clustering step:

  $$\sqrt{d_{12}} = \min(p_{T1}, p_{T2}) \times \Delta R_{12} \tag{4.5}$$

  The k_t algorithm combines the hardest proto-jets at the last step of clustering, so $\sqrt{d_{12}}$ can distinguish the products of the W boson, which tend to have a symmetric energy distribution, from QCD jets which are more asymmetric on average.

- **Momentum balance** [35] The momentum balance, $\sqrt{y_{\mathrm{f}}}$, is defined as the ratio between the splitting scale defined above, and the jet mass of the final clustering step:

  $$\sqrt{y_{\mathrm{f}}} = \frac{\min(p_{\mathrm{T}1}, p_{\mathrm{T}2})}{m_{12}} \Delta R_{12} \tag{4.6}$$

- **Mass-drop** [35] The mass-drop fraction, μ_{12}, is also defined at the last step of recombination where two ‘proto-jets’ are combined to form one ‘jet’. μ_{12} is the fraction of mass carried by the most massive proto-jet:

  $$\mu_{12} = \frac{\max(m_1, m_2)}{m_{12}} \tag{4.7}$$

- **Jet width** [39] The jet width is the first radial moment in (η, ϕ) space weighted by p_T. Symbolically:

$$w = \frac{\sum_i p_{Ti} \Delta R_{iJ}}{\sum_i p_{Ti}}, \tag{4.8}$$

where J denotes the jet axis, and i runs over the set of constituents of the jet. Jet mass and jet width are related, but as a dimensionless quantity the jet width may be less sensitive to the uncertainties in the overall energy scale.

- **Planar flow** [55] Planar flow is a measure of how uniformly spread out the energy of a jet is perpendicular to its axis. Denoted P, planar flow is computed as

$$P = 4 \times \det(I)/\mathrm{Tr}(I)^2, \tag{4.9}$$

where I is a two-dimensional matrix of momentum correlations defined as $I_{ab} = \frac{1}{M} \sum_i \frac{p_{i,a} p_{i,b}}{E_i}$. The index i runs over the set of constituents of a jet and the a, b indices represent the components of the p_{T} of the i^{th} constituent perpendicular to the jet axis. A typical QCD jet is characterized by the planar flow near 1, in contrast to a smaller value expected for the localized two-prong structure of W jets.

- **N-subjettiness** [56] The jet shape moment "N-subjettiness" describes to what degree the substructure of a given jet resembles N or fewer subjets. The parameter τ_N is used to describe the substructure and is defined as

$$\tau_N = \frac{\sum_k p_{\mathrm{T},k} (\min\{\Delta R_{1,k}, \Delta R_{2,k}, ..., R_{N,k}\})^\beta}{\sum_k p_{\mathrm{T}} (R_0)^\beta} \tag{4.10}$$

where the sum runs over the constituents of the jet, $p_{\mathrm{T},k}$ is the momentum of constituent k, $\Delta R_{A,k}$ is the azimuth-rapidity distance between subjet axis A and particle k and R_0 is the characteristic jet radius. The constant β is an angular weighting component, set to 1 for this study. While the τ_N variables on their own are not particularly powerful at discriminating the number of hard subjets, the ratios τ_N/τ_{N-1} are powerful discriminants of jets containing N hard subjets. In this note, τ_2/τ_1 is used to highlight the two-body structure of a jet coming from W decays.

- **Q-jets mass volatility** [57] For a jet clustered with a given recombination jet clustering algorithm, the Q-jets technique reclusters the jet many times with a degree of randomness. Following this, any jet observable, such as the mass, will have a distribution for a given jet. At a given step in clustering, the probability that a pair is clustered is proportional to

$$\omega_{ij}(\alpha) = \exp\left\{-\alpha\frac{\Delta R^2_{ij} - \Delta R^2_{\min}}{\Delta R^2_{\min}}\right\}, \tag{4.11}$$

where the rigidity $\alpha \in \mathbb{R}$ controls the level of randomness. A value of $\alpha = 0.1$ was optimized in Ref. [46] and adopted in this study. The high mass in W jets tends to persist during the re-clustering while the mass of QCD jets fluctuates. A sensitive observable to this trend is the coefficient of variation of the mass distribution for a single jet, called the volatility:

$$\nu_{\text{QJets}} = \frac{\sqrt{\langle m^2\rangle - \langle m\rangle^2}}{\langle m\rangle}. \tag{4.12}$$

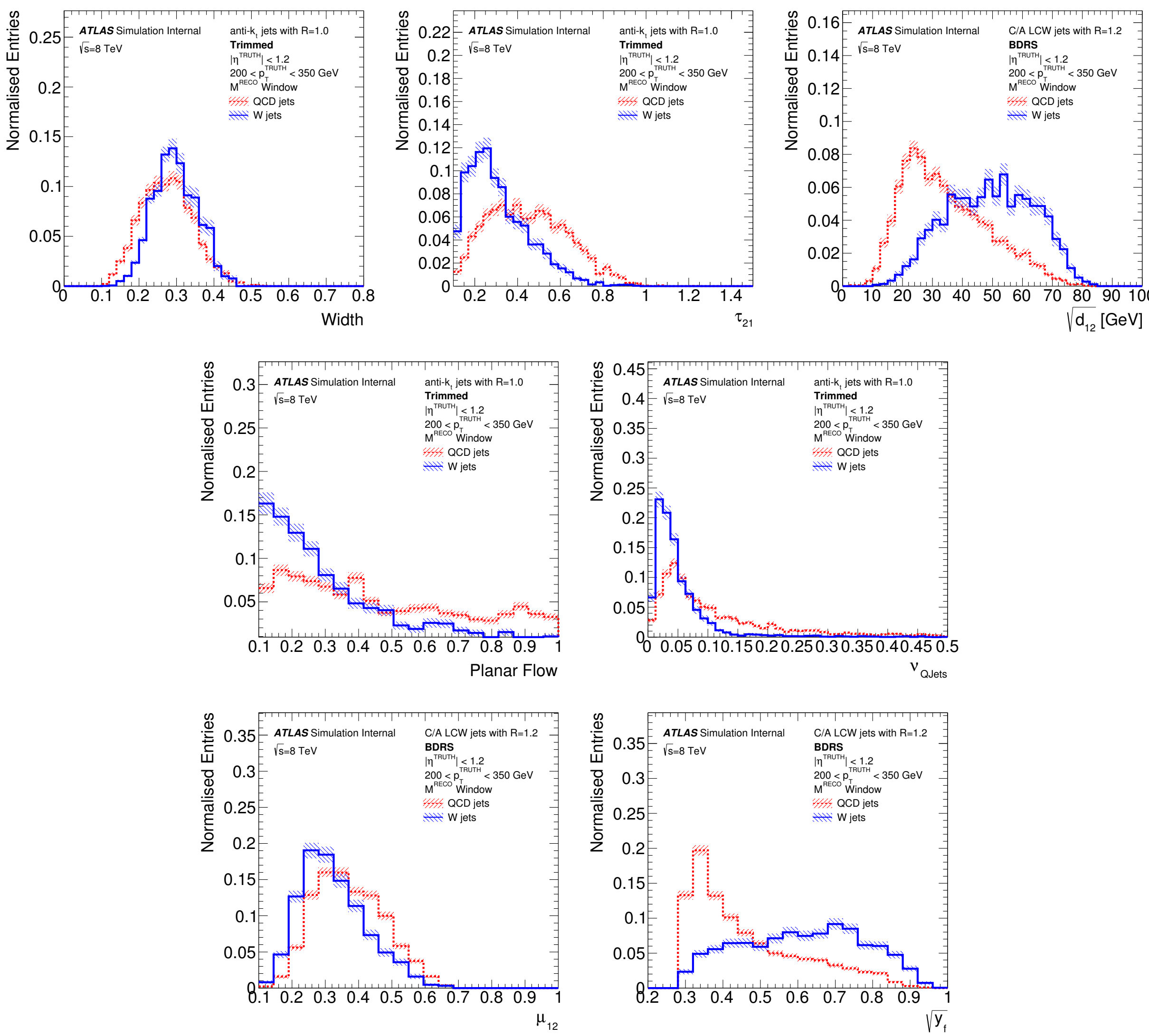

Figure 4.14: The seven substructure moments in W jet (signal) and QCD jet (background) distributions are shown. In each case, the grooming algorithm shown is that which makes the best groomer+tagger combination in terms of efficiency and rejection. The shaded band represents the bin-by-bin statistical uncertainty in simulation.

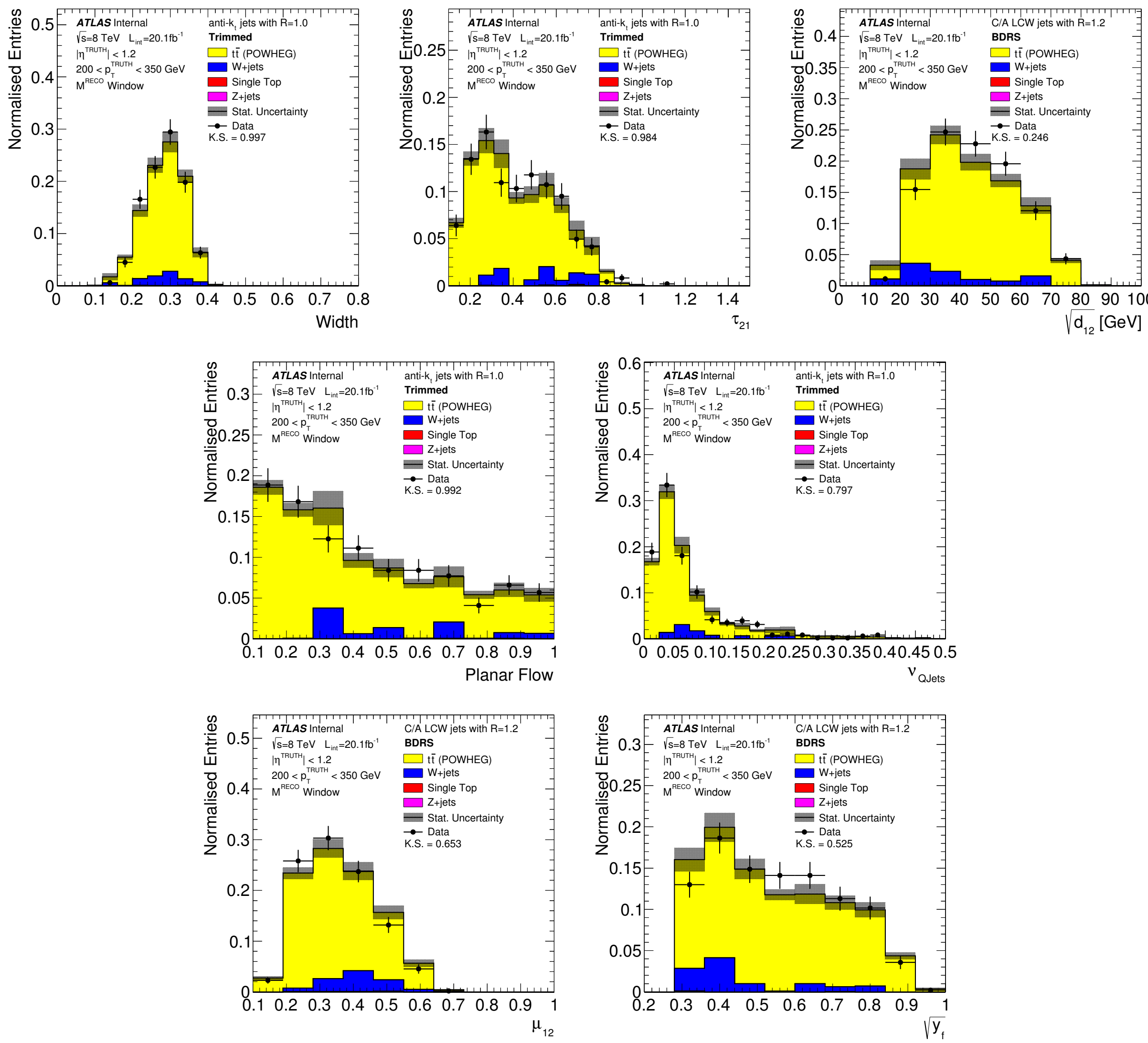

Figure 4.15: The seven substructure moments in the comparison of data to boosted $t\bar{t}$ signal Monte Carlo preselected with the HEPTopTagger in the regime of $200GeV < p_T(reco) < 350GeV$. This sample is chosen such that the hadronically decaying top is boosted to the extent that the $W \rightarrow q\bar{q}$ decay is fully merged, without the full merging of the Wb system.

4.4.3 Optimizing Single Variable Discrimination

By making a selection requirement on a given substructure moment, some level of discrimination can be gained as seen in Figure 4.14. However, there are five different grooming algorithms and seven different substructure moments, which means the set defined by the convolution of these two sets is large. To perform this optimization, ROC curves, described in Appendix C, are used to rank the performance for a given operating point. The full evaluation of the performance of the jet finding and grooming algorithm with a substructure tagging moment must take into account two stages:

1. The effect of the substructure tagging moment ϵ^{Tag} to reject QCD jets while accepting boson jets after a selection on the jet mass.

2. The combined effect of the substructure tagging moment and the groomed jet mass window $\epsilon^{\text{Groom}} \times \epsilon^{\text{Tag}}$ which combines the QCD jet rejection power from both the mass and substructure selections. This performance metric is obtained by transforming that determined in (1) by the signal efficiency and background rejection obtained from the optimized mass window selection. It should be noted that this limits the maximal signal efficiency to 68%.

Furthermore, two ways for deciding what constitutes the best combined performance are used in this section.

1. For each substructure moment, identify the jet grooming algorithm that gives the greatest background rejection at a fixed 50% signal efficiency for the grooming + tagging combination.

2. For each jet grooming algorithm, identify the substructure moment that gives the greatest background rejection at a fixed 50% signal efficiency, again for the grooming + tagging combination.

These two different approaches are complementary in the conclusions they provide and the results are shown in Figures 4.16, 4.17, and 4.18 for the three different kinematic regimes studied. For most of the working points, the difference between the best few algorithms is very small, at the level of a few percent and with the full inclusion of systematic uncertainties it is likely that the performances of the best algorithms will be equivalent within these uncertainties. An understanding of the uncertainties is therefore important because in analyses dealing with very large backgrounds, even a difference in background rejection of a few percent is worth pursuing.

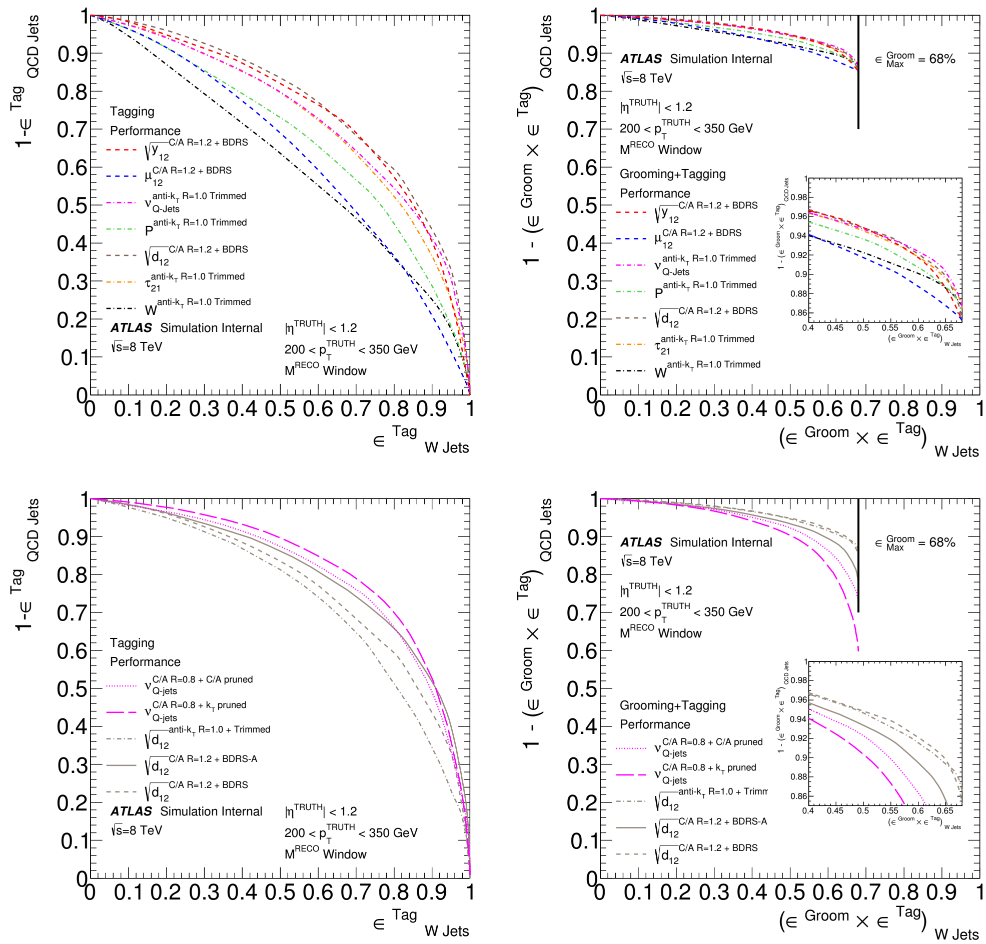

Figure 4.16: For the kinematic $p_T^{Truth} = [200, 350]$ GeV region, the comparison of optimized ROC curves for the tagger only performance (left) and for the full groomer + tagger performance (right). The set of curves shown on the top is derived by fixing the jet algorithm and determining the optimal tagging variable for that algorithm while the set on the bottom is derived by fixing the tagging variable and determining the optimal groomer to use with that tagger.

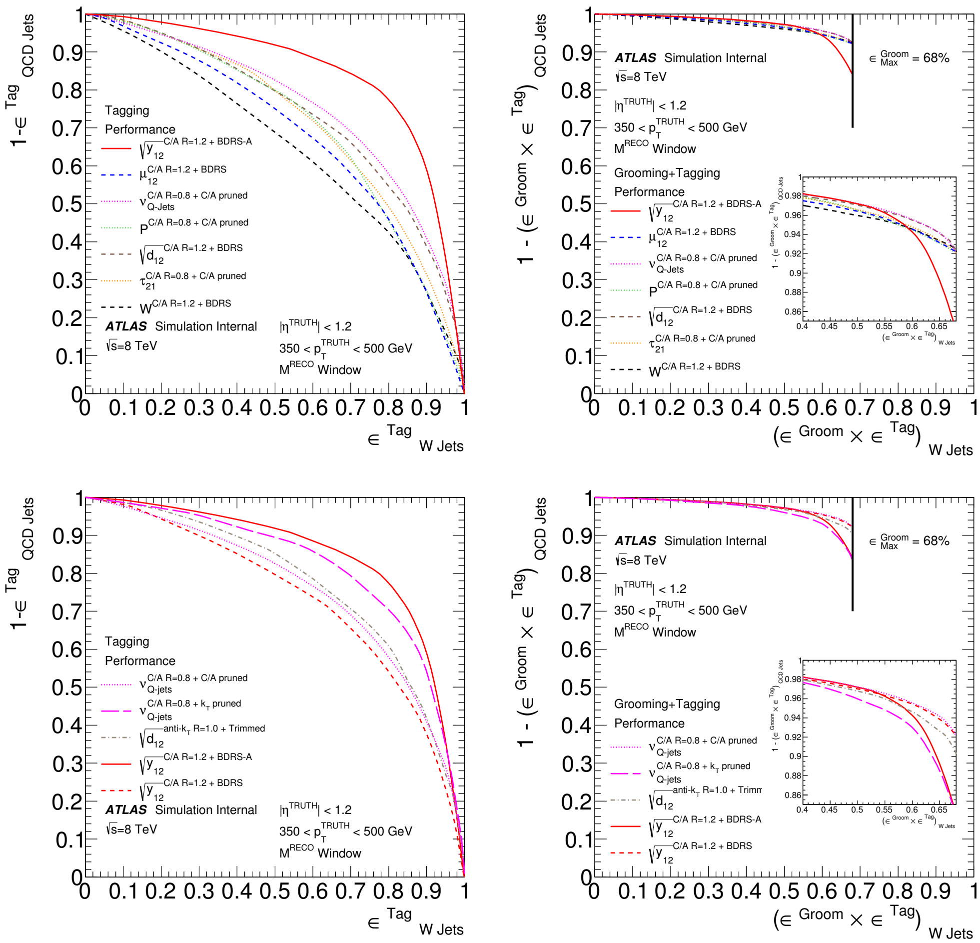

Figure 4.17: For the kinematic $p_T^{Truth} = [350, 500]$ GeV region, the comparison of optimized ROC curves for the tagger only performance (left) and for the full groomer + tagger performance (right). The set of curves shown on the top is derived by fixing the jet algorithm and determining the optimal tagging variable for that algorithm while the set on the bottom is derived by fixing the tagging variable and determining the optimal groomer to use with that tagger.

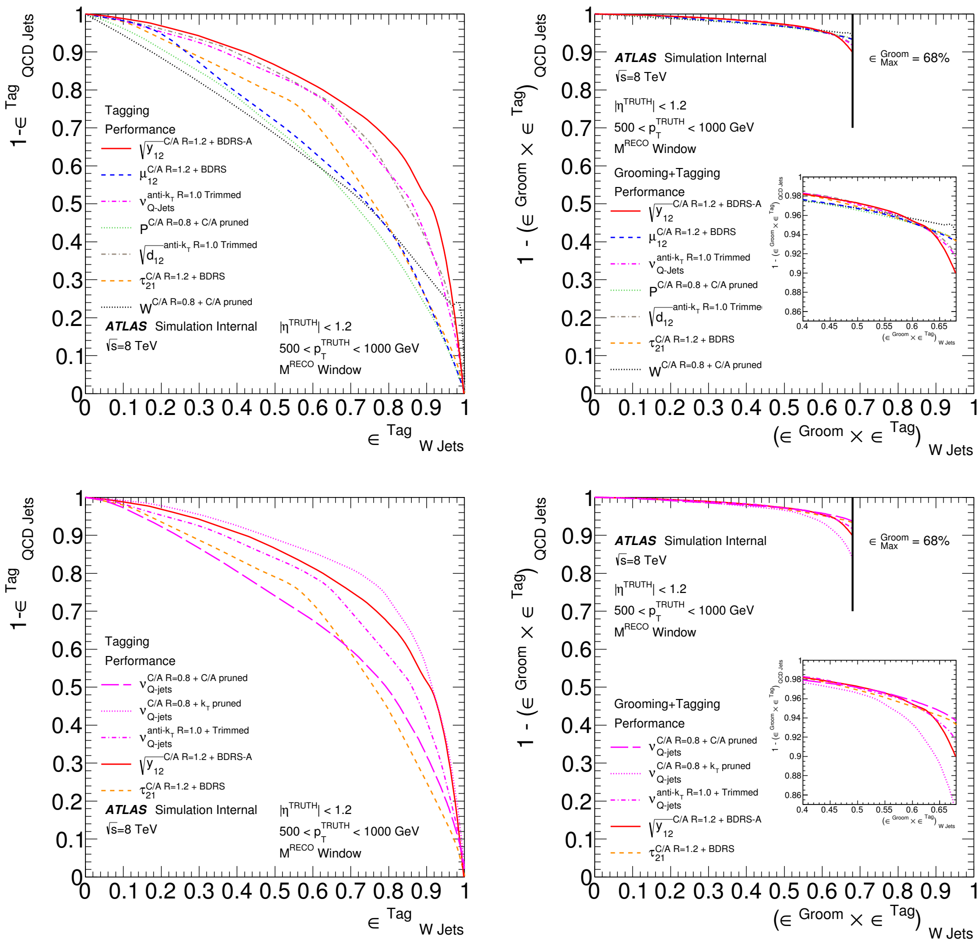

Figure 4.18: For the kinematic $p_T^{Truth} = [500, 1000]$ GeV region, the comparison of optimized ROC curves for the tagger only performance (left) and for the full groomer + tagger performance (right). The set of curves shown on the top is derived by fixing the jet algorithm and determining the optimal tagging variable for that algorithm while the set on the bottom is derived by fixing the tagging variable and determining the optimal groomer to use with that tagger.

4.4.4 Multivariate Boson Discrimination

All substructure variables are constructed from the energy and angular separation of jet constituents, and are thus correlated. Furthermore, they all attempt to parameterize the substructure information in different ways and so it is worth pursuing the possibility of exploiting these correlations in a multivariate combination to gain maximum sensitivity. Such attempts have been made previously [58] and found the gains to be minor compared to expected uncertainties associated with the variables in question.

To determine the extent to which this conclusion holds for the approaches taken here, the linear correlation matrices are examined for three of the grooming algorithms under study (BDRS, Trimmed, and C/A-pruned), after applying the mass window requirement determined in Section 4.4.1. By comparing these correlations in signal and background, it is possible to understand what first order correlations would likely be exploited in a multivariate analysis. Here the correlation factors between pairs of variables are calculated as their covariance divided by the product of their standard deviations:

$$\rho = \frac{cov(x,y)}{\sigma_x \, \sigma_y} \tag{4.13}$$

These correlation matrices are shown in Figure 4.19. The correlation matrices of BDRS-A and k_t-pruned jets are similar to BDRS and C/A-pruned jets, respectively, within 10% variation. The p_{T} dependence of the correlation matrix is also within 10% variation. Some selected observations from these matrices can be made:

- Width and $\sqrt{d_{12}}$ are highly correlated to jet mass.
- Planar flow is highly correlated to τ_{21} and anti-correlated to $\sqrt{d_{12}}$.
- The mass-drop, μ_{12}, is highly correlated with planar flow and τ_{21} in C/A jets but not in anti-k_t jets.
- The Q-jet volatility, ν_{Qjets}, is weakly anti-correlated with most of the variables, so it could be effectively used in combination with other taggers.
- The correlation of τ_{21} to $\sqrt{y_f}$ and μ_{12} in C/A jets is reduced after pruning.
- The mass-drop, μ_{12}, is anti-correlated to jet mass, $\sqrt{d_{12}}$ and width, and is correlated with τ_{12} and planar flow in W jets.

- The correlation is weaker in QCD-jets and even smaller in the C/A-pruned jets.
- All substructure variables under study are weakly correlated with the number of reconstructed primary vertices, N_{vtx}, indicating a weak pileup dependence.

The most important general observation, however, is that the correlations between substructure variables are too similar in signal and background to be expected to give significant gains in performance when combined through machine learning. This points to the fact that although the substructure moments are unique in definition, the aspects of the substructure in the parton shower that they are exploiting are common at some higher, more abstracted level. More effectively probing this full wealth of information using multivariate techniques in terms of conventional approaches and the techniques of shower deconstruction [59] are both active areas of work in ATLAS.

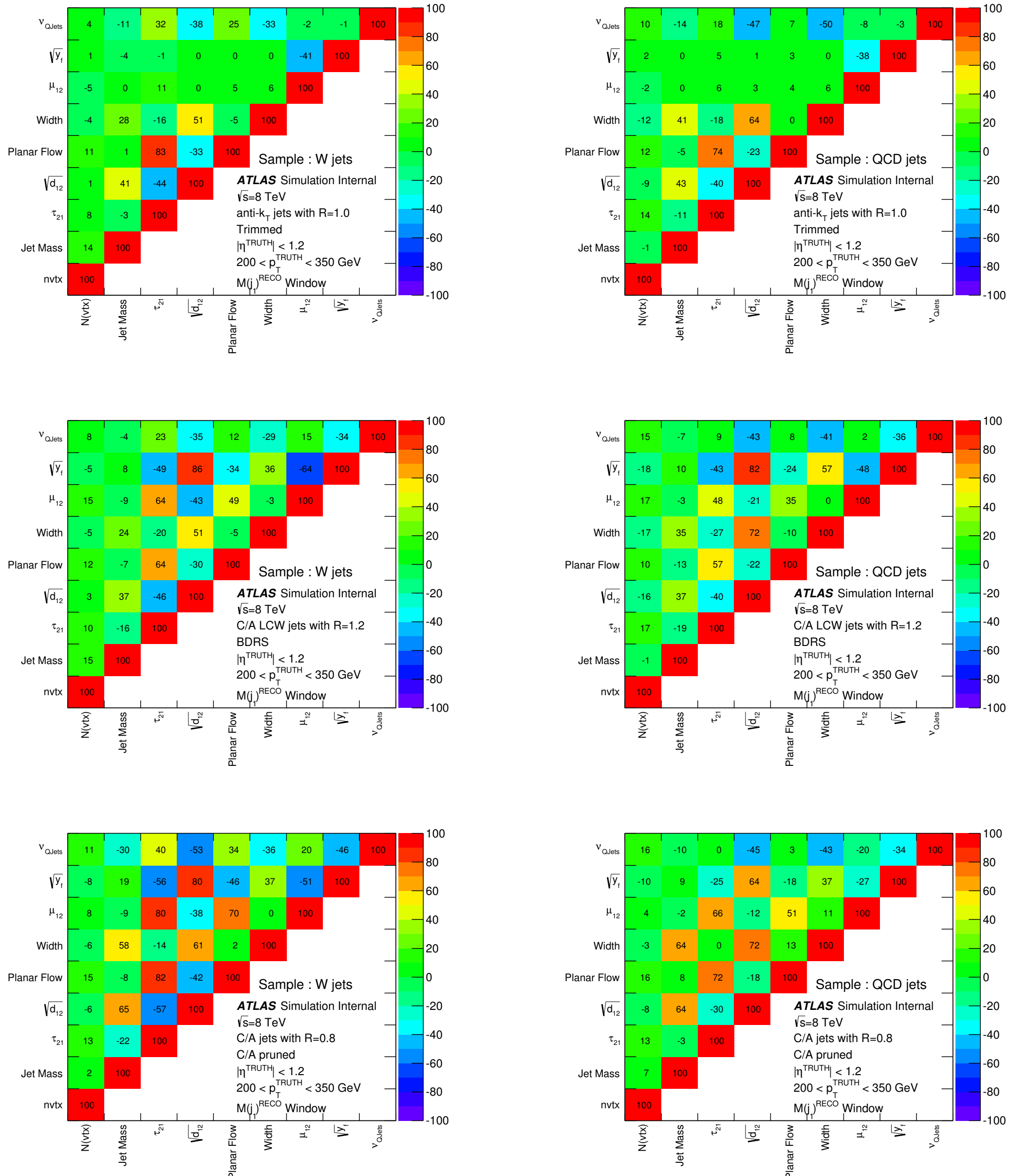

Figure 4.19: Linear correlation matrices for variables the range $200 < p_{\mathrm{T}} < 350$ GeV for the leading jet, after the dynamic mass window cut for three of the jet algorithms studied.

Chapter 5
The Search

In designing a signature based search, careful thought is given to the unique characteristics that distinguish the signal from the background. In this case, the signal is the s-channel production of a massive new particle (i.e. G^* or W') that decays to a pair of gauge bosons as shown in Figure 5.1, with one Z boson decaying leptonically and another W or Z boson decaying hadronically. The full signature for which this search is designed is therefore $X \to Z + V \to \ell\ell + q\bar{q}$ (with $V = W, Z$). The particular beyond the Standard Model particle, X, ranges from $M(X) = 300$ GeV to $M(X) = 2000$ GeV. This particular range is chosen because of the possible final states to which the W and Z bosons can decay. For masses below 300 GeV, there are sufficient statistics available in the all leptonic channels ($ZZ \to \ell\ell\ell'\ell'$ and $WZ \to \ell\nu\ell'\ell'$) which have greater mass resolution when reconstructing the final state and therefore greater sensitivity to resonant excesses. For masses above 2 TeV, however, the presence of the leptonic branching in the semi-leptonic mode causes for the number of events in the final state to significantly decrease. Therefore, the all hadronic decay mode ($ZZ/WZ \to qqq'q'$) dominates in sensitivity above this point. In this intermediate mass range, however, the semileptonic decay mode benefits from both the increase in statistics from the hadronic W/Z boson decay in addition to the cleanly measured dilepton system.

The mass splitting between $M(X)$ and $M(W, Z)$ immediately indicates that the final state objects can have large transverse momenta, large "boost". The extent to which the objects are boosted splits the search into two natural categories, based on the topology of the hadronic decay of the W or Z boson. For $M(X) < 1$ TeV, it is likely that the quarks from this decay will be well separated and be resolved as two independent jets in the calorimeter. However, for $M(X) > 1$ TeV, the back-to-back decay in the rest frame from

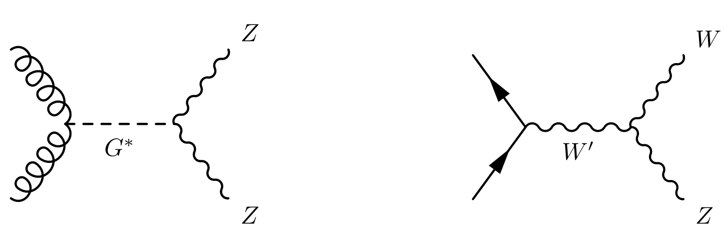

Figure 5.1: Example Feynman diagrams for the bulk Randall-Sundrum graviton decaying to a pair of Z bosons (left) and an extended gauge model W' decaying to a WZ pair (right).

the W or Z boson occurs in a heavily boosted ($p_T \sim 400$ GeV) lab frame and so the parton showering and subsequent hadronization of the partons will be less distinguishable. It thus becomes advantageous to apply the techniques of jet substructure, described in Section 4.4 to reconstruct the entire W, Z system as a single jet and distinguish the resultant jet from those coming from processes involved QCD jets. Once the subset of events representative of an $X \to Z + V \to \ell\ell + q\bar{q} \to \ell\ell + jet + jet$ and $X \to Z + V \to \ell\ell + q\bar{q} \to \ell\ell + FatJet$ are identified, the mass spectrum of the new particle can be reconstructed as the invariant mass $M(\ell\ell + jet + jet)$ or $M(\ell\ell + FatJet)$, and by examining the spectrum of these events, it can be determined whether a resonant excess appears in the data. To achieve this goal, multiple steps are taken that are summarized as:

1. Trigger on events containing leptons; electrons or muons.
2. Reconstruct a high-p_T $Z \to \ell\ell$ decay.
3. Reconstruct a high-p_T $W/Z \to jet + jet$ or $W/Z \to FatJet$ decay.
4. Reconstruct the $M(\ell\ell + jet + jet)$ or $M(\ell\ell + FatJet)$ invariant mass spectrum and search for a resonant peak excess over background indicative of new physics. [1]
5. In the event that no excess is present, set limits on the cross section times branching ratio of $\sigma(pp \to X) \times BR(X \to ZZ, ZW)$

5.1 Data Collection

The data sample used in this search was collected during 2012, while the LHC was operating at $\sqrt{s} = 8$ TeV. Over the course of the year, the LHC delivered 23.3 fb^{-1} of integrated luminosity with an average of 21 interactions per bunch crossing. Of this luminosity, 21.3 fb^{-1} was recorded by ATLAS, the difference being due to detector inefficiencies. The evolution of the accumulation of this recorded data is shown in Figure 5.2. However, for any number of reasons pertaining to faulty detector operations (e.g. power failures), not all portions of the data are useable in the analysis and events recorded during these portions of data taking

1. The shape of this excess is process dependent, but in general somewhat Gaussian with a width that varies between 20 GeV and 150 GeV depending on the signal pole mass. More details can be found in Appendix D.

are vetoed, leading to a final dataset amounting to 20.3 fb^{-1} that was used for the search. Of this dataset, further event vetoes are applied to known events during which calorimeter systems experienced serious problems, or the recorded data was known to be corrupt.

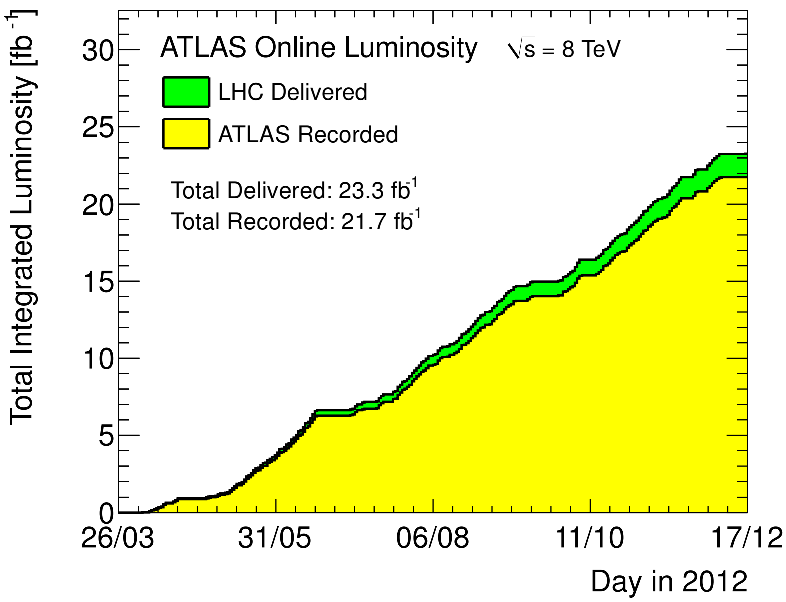

Figure 5.2: Record showing the accumulation of integrated luminosity during the course of 2012 data taking.

5.2 Trigger

One of the challenges of producing data through collisions at a rate of 40 MHz in the LHC is determining which events to write to offline storage for more careful analysis. The decision chain that makes this choice is called the trigger. The trigger in ATLAS is composed of three levels; a level one, hardware based trigger that is based on calorimeter or muon spectrometer information which seeds a level two trigger, and then an event filter software based trigger which implements successively more precise algorithms that are closer to offline reconstruction algorithms. The trigger philosophy of ATLAS is to implement general purpose triggers that can be used by a number of analyses. Therefore, the triggers used in this analysis are focused on detecting the presence of leptons from the $Z \to \ell\ell$ boson decay, for which there are two separate chains; one for electrons and one for muons.

In the case of electrons, the level one trigger uses a sliding window algorithm to scan the calorimetry for electromagnetic showers with a total energy above the noise threshold of the calorimeter and high enough to sufficiently reduce the frequency at which events are triggered to a manageable rate. These regions of interest are then sent to the level two trigger which combines information from the tracker to reduce the trigger rate. Lastly, the event filter trigger defines selection criteria that closely resemble the offline selection quality of electrons selected as in Section 5.3.1. In particular, events are recorded at this stage if there is a single electron with an energy of at least 60 GeV passing a medium set of quality criteria, a single isolated electron of energy of at least 24 GeV passing the same medium set of quality criteria, or a pair of electrons, each having an energy of at least 12 GeV, and slightly looser quality criteria. Further details concerning the implementation of the electron triggers can be found in [60].

The trigger chain for muons proceeds by initially searching for coinciding hits in muon chambers in dedicated hardware that uses the position of the coincidence hits to estimate the muon momentum. The level two trigger and event filter proceeds similarly to that of the electron trigger by implementing fast muon reconstruction algorithms in a region of interest defined by the level one coincidence. The final set of criteria that determine if the muon trigger is passed and an event used in analysis is the presence of a single muon with at least 36 GeV of transverse momentum being required to pass a set of tight quality criteria, a muon with at least 24 GeV of transverse momentum that is isolated from other activity and passes the same set of quality criteria, or a pair of muons, one with at least 18 GeV of transverse momentum passing the same quality requirements and another muon with at least 8 GeV of transverse momentum. Further details concerning the implementation of the muon triggers can be found in [61].

The figure of merit determining the extent to which the triggers used to record events for a given analysis are performing well is the trigger efficiency. This is defined as the ratio of events that pass all offline selection criteria, except the trigger, to those passing the offline selection and the trigger. For the electron channel, this is greater than 99% across the mass range of the search. For the muon channel, this is approximately 92%, due to the geometrical acceptance of the muon spectrometer used to determine a positive level one muon trigger, 80% in the barrel, which is low due to the presence of services for the calorimetry and inner detector.

5.3 Physics Object Reconstruction and Selection

In order to reconstruct events used in the search, it is necessary to identify signatures in the detector that are consistent with the presence of well understood particles coming from the hard scatter event. These signatures are abstractly called physics objects, of which there are three types used in this analysis; electrons, muons, and jets. The ATLAS detector was designed such that combinations of subsystems can be used to make a measurement of three components of the four-vector of an object, and in the case of jets, its constituents as well, with the full four vector being reconstructed assuming the mass of the particle being measured. In addition to making this basic measurement, ancillary information is extracted that pertains to the quality of the measurement performed and the quality of the physics object that was reconstructed. This information is essential in identifying and rejecting instances of "fakes" where a different type of particle or a detector malfunction causes the reconstruction algorithms to detect the presence of a physics object.

5.3.1 Electrons

Identifying and measuring electrons is crucial to this analysis to accurately reconstruct the $Z \to ee$ decay and provide an initial handle to significantly reduce the large multijet background and identify signatures of possible new physics. To do this effectively, information is used from the inner detector to reconstruct the track of the electron and from the liquid argon calorimeter, which stops the electron and measures its energy. This reconstruction begins by using a sliding window algorithm with a window of 3×5 in units of 0.025×0.025 in (η, ϕ) space to reconstruct electromagnetic clusters. Inner detector tracks are then matched to these clusters by extrapolating the fitted track and declaring a match if an EM cluster is within $|\Delta\eta| < 0.05$ and $\Delta\phi < 0.05$, with a loosened $\Delta\phi < 0.1$ matching on the external bending side of the track to allow for possible bremsstrahlung. After initially finding the set of electrons, the EM cluster measurement is refined by modifying the cluster to account for the differing detector geometry and the track is refit using a Gaussian sum filter [62] that fits tracks under the assumption of bremsstrahlung radiation during the propagation of the electron to more accurately model its path. The energy (E), transverse momentum (p_{T}), and pseudorapidity (η) are then defined using the following prescription to ensure that the measurement is made using the most accurate pieces of information available

- The electron energy is measured from the calorimeter cluster energy. This measurement is then scaled by calibrations determined from $Z \to ee$ decays, in data and smeared in Monte Carlo to match detector resolution.

- If the electron track has less than 4 combined SCT and pixel hits, then the pseudorapidity is taken to be the calorimeter cluster pseudorapidity. Otherwise, the track pseudorapidity is used. This avoids problems with TRT-only tracks for which there is no η measurement.

- The transverse momentum is defined as the energy divided by $\cosh(\eta)$.

This set of reconstructed electron objects is then required to pass the following requirements to select good quality electrons and reject fake electrons coming from misidentification of hadrons.

- Veto the electron if the cluster measurement is categorized as poor quality based on the quality of the energy measurement in the cells associated with that cluster.

- Consistency with medium electron quality criteria optimized for the 2012 data taking period that take advantage of the LAr calorimeter segmentation to construct shower shapes that are used to identify electrons.

- To ensure that the electron comes from the hard scatter of interest, the electron track must have a longitudinal impact parameter ($|z_0 \sin\theta|$) along the beam axis less than 0.5 mm from the primary vertex. In addition, the transverse distance of closest approach in the x-y plane to the primary vertex divided by its uncertainty ($\frac{|d_0|}{\sigma(d_0)}$) must be less than 6.

- The sum of transverse momenta of tracks with $p_{\mathrm{T}} > 1$ GeV surrounding the electron track in a cone of radius 0.2 divided by the electron p_{T} must be less than 0.15. The sum of transverse energy of calorimeter cells surrounding the cluster associated with the electron in a cone of radius 0.2, accounting for leakage into the cone from the central core and for pileup contributions, divided by the electron E_T must be less than 0.3. Both of these are calculated as the ATLAS standard isolation variables for electrons.

- For non-isolated electron pairs with $\Delta R(ee) < 0.2$, the isolation variables are calculated with the dilepton isolation algorithm explained in Section 5.3.3.

- Transverse energy $E_{\mathrm{T}} > 25$ GeV.

- Pseudorapidity $|\eta| < 2.47$, excluding electrons in the region of $1.37 < |\eta| < 1.52$ which is uninstrumented with liquid argon calorimetry due to the presence of service cables.

The electron objects reconstructed in Monte Carlo simulated events do not fully reproduce the reconstruction and identification efficiencies and energy resolution measured in data, which itself does not necessarily measure electrons at the correct energy scale which is observed through the measurement of the $Z \to ee$ mass peak. Therefore, a number of corrections are applied to the electrons. The first is an electron energy scale correction made to electrons in data and a smearing correction to electrons reconstructed in Monte Carlo to match the energy resolution in data. These two corrections are primarily measured using samples of $J/\Psi \to ee$ and $Z \to ee$ events and validated using measurements comparing the track momentum to calorimeter energy in the higher statistic $W \to e\nu$ samples. The reconstruction efficiency scale factors, defined as the ratio of reconstruction efficiency in data and Monte Carlo, is measured using the "tag and probe" method described in [63] with the same type of $Z \to ee$, $J/\Psi \to ee$, and $W \to e\nu$ events. These correction factors for the medium quality electrons are determined in bins of η and are within a few percent of unity.

In the future there will be a combination of multiple searches for resonant diboson production, and to allow them to be combined statistically, exclusive selection are made based on the number of leptons in the final state. Therefore, in addition to identifying the two leptons coming from the $Z \to ee$ decay, it is necessary to identify any additional electrons produced in the hard scatter and veto such events. The veto electron definition is similar to the signal electron definition but with slightly loosened criteria to produce a conservative veto that ensures exclusivity between individual channels. These modified requirements are:

- No veto due to the quality of the measured electron

- Lower transverse energy requirement, $E_{\mathrm{T}} > 20$ GeV

- Looser requirement on longitudinal impact parameter, $|z_0 \sin\theta| < 2.0$ mm

- No calorimeter isolation requirement is applied.

5.3.2 Muons

As with electrons, the proper reconstruction and measurement of muon objects used to reconstruct the $Z \to \mu\mu$ decay is very important in this second primary channel of this analysis. However, because muons are minimum ionizing particles, they are not stopped in the calorimeter system as is the case for electrons. Rather, they traverse the entire detector and leave only small deposition of energy in each layer. These depositions are used to reconstruct the muon object as a track using information from both the inner detector and the muon spectrometer and in some cases the calorimeter system [61].

The procedure used to perform this reconstruction is to reconstruct tracks independently using ID-only and MS-only information. These two sets of tracks are then roughly matched in (η, ϕ) space and any possible matched track candidates are further combined using the procedure described in [64] which compares the full set of track parameters with the co-variance matrix to parameterize the uncertainty, and returns a single ID+MS track whose parameters are a statistical combination of both sets of information. Other procedures exist in ATLAS that use only partial information and using these algorithms can lead to increases in overall signal reconstruction efficiency of the order of a few percent. However, using muons reconstructed with the single combined algorithm results in the selection of muons with the lowest level of misidentified muons.

After reconstructing an initial set of muons as matched tracks, the quality of the muon is ensured to be high by making the following requirements on the track information of the ID and MS.

- A hit on the innermost pixel detector layer hit if one is expected based on the overall track fit.

- The sum of the number of pixel hits and the number of dead pixel sensors traversed by the muon track must be greater than or equal to 1.

- The sum of the number of SCT hits and the number of dead SCT sensors traversed by the muon track must be greater than or equal to 5.

- The sum of pixel and SCT track holes must be less than 3.

- A high quality TRT track if the muon track falls within the η acceptance of the TRT.

Defining N_{TRT} as the sum of the number of TRT hits and the number of TRT outliers, the following TRT hit conditions must be satisfied: If the η of the muon track is within $0.1 < |\eta| < 1.9$, then N_{TRT} must be greater than 5 and the fraction of the number of TRT outliers must be less than 90%. If $|\eta| \leq 0.1$ or $|\eta| \geq 1.9$ and $N_{TRT} > 5$, then the fraction of TRT outliers must be less than 90%.

- To ensure that the momentum is consistently measured between the muon spectrometer (MS) and inner detector (ID), the q/p measurements in the two detectors are required to satisfy $\frac{|(q/p)_{\mathrm{MS}} - (q/p)_{\mathrm{ID}}|}{\sigma_C} < 5$, where σ_C is the combined q/p uncertainty, q is the muon charge, and p is the momentum of the muon.

- To ensure that the muon comes from the hard scatter of interest, the muon track must have a longitudinal impact parameter $|z_0 \sin\theta|$ less than 0.5 mm and the transverse impact parameter significance $\frac{|d_0|}{\sigma(d_0)}$ less than 3.5.

From the group of muon candidates that satisfy all of these requirements, the following quality selections are applied:

- $p_{\mathrm{T}} > 25$ GeV where p_{T} is the combined muon track p_{T}.

- $|\eta| < 2.5$.

- The sum of transverse momenta of tracks with $p_{\mathrm{T}} > 1$ GeV surrounding the muon track in a cone of radius 0.2 divided by the muon p_{T} must be less than 0.15. The sum of transverse energy of calorimeter clusters surrounding the muon track in a cone of radius 0.2 divided by the muon p_{T} must be less than 0.3. This requirement is made to reject jets that may contain a semi-leptonic B-meson decay

- For non-isolated muon pairs with $\Delta R(\mu\mu) < 0.2$, the isolation variables are calculated with the dilepton isolation algorithm explained in Section 5.3.3 and the same cut values on the isolation variables are used.

The muons in Monte Carlo simulated events do not fully reproduce the reconstruction efficiency and p_T scale and resolution measured in data using $J/\Psi \to \mu\mu$,$\Upsilon \to \mu\mu$, and $Z \to \mu\mu$ events. Therefore, the p_T of a muon candidate derived from the initial track fitting procedure is corrected. Both the ID and MS tracks are smeared and the result is propagated to the combined muon p_{T} measurement [65]. Furthermore, to account for mismodelling in reconstruction efficiencies, event-by-event weights are applied to the Monte Carlo to correct for these that are 1.0 to within the percent level [61].

Similar to the electron case, the veto muon, used to reject events that may contain three or more real leptons is defined using the same criteria for signal muons except with looser selection criteria to ensure that the veto is more conservative. These loosened criteria are:

- Lower transverse momentum $p_{\mathrm{T}} > 20$ GeV,
- Loosened impact parameters $|z_0 \sin\theta| < 2.0$ mm,
- No calorimeter isolation is applied.

5.3.3 Dilepton Isolation

For signal resonance masses above $M(X) \sim 1.6$ TeV the opening angle of the two leptons from the decay of the $Z \to \ell\ell$ decay starts to become smaller than the isolation radius of $\Delta R = 0.2$ due to the boost of the Z boson and leads to a significant loss in acceptance above this mass because the leptons start to enter the isolation cone of each other. To mitigate this effect and improve the acceptance for events with boosted Z bosons the concept of isolation is extended to dilepton objects. The basic idea of the dilepton isolation is to subtract the energy of the second lepton if it falls into the isolation cone of the first lepton, and to apply the isolation criteria to the isolation variables for both combinations of the leptons in the pair $\{l_1, l_2\}, \{l_2, l_1\}$. Taking into account this modification of isolation in a boosted dilepton topology, there are three types of isolation criterion that are applied:

- $Iso_{20}^{track} = \frac{\Sigma p_T^{track}(\Delta R(\ell,track)<0.2)}{p_T^{\ell}} < 0.15$ (PtCone) : The sum of transverse momenta of tracks with $p_T > 1$ GeV surrounding the electron or muon track in a cone of radius 0.2 divided by the lepton p_T must be less than 0.15.
- $Iso_{20}^{calo} = \frac{\Sigma E_T^{cluster}(\Delta R(\ell,cluster)<0.2)}{E_T^{\ell}} < 0.14(0.3)$ (EtCone) : The sum of transverse energy of calorimeter clusters surrounding the cluster (track) associated with the electron (muon) in a cone of radius 0.2 divided by the electron E_T (muon p_T) must be less than 0.14 (0.3). In the case of electons, this energy is corrected for electron energy leakage from the electron cluster core and pile-up contributions.

- $DilepIso_{20}^{track} = \frac{\Sigma p_T^{track}(\Delta R(\ell_1,track)<0.2) - p_T^{\ell_2}}{p_T^{\ell_1}} < 0.15$ (Di-lepton PtCone) : This requires a pair of leptons (ℓ_1 and ℓ_2) and deems the lepton pair to be isolated if both leptons pass the nominal PtCone isolation criterion where the sum of transverse momentum in the isolation cone is corrected by removing the contribution from the second lepton. Note that the equation above is only for lepton 1 and also must hold for lepton 2.

These criterion are applied in three different scenarios, defined based on the separation of the two leptons selected with all criteria *except* isolation.

- If $\Delta R(\ell\ell) > 0.25$: Apply EtCone isolation and PtCone isolation.
- If $\Delta R(\ell\ell) > 0.2$: Apply PtCone isolation but *not* EtCone isolation.
- If $\Delta R(\ell\ell) < 0.2$: Require Di-lepton PtCone isolation on the lepton pair but *not* EtCone isolation.

Shown in Figure 5.3 is the 2D plane of lepton separation and the calculated PtCone variable for an $M(G^*) = 2$ TeV graviton sample. It can clearly be seen that in the case of the PtCone being calculated in the nominal ATLAS way for traditional lepton objects, nearly all of the cases where the leptons become separated by less than $\Delta R < 0.2$ cause for the isolation to fall in the region that is rejected by the quality requirement imposed in the analysis. However, when the dilepton prescription is applied, nearly all of these events migrate to the region accepted and the real $Z \to \ell\ell$ can be reconstructed.

The affect of applying this dilepton isolation criteria is a marked increase in acceptance in the very high mass region as shown in Figure 5.4. As expected, the biggest increase is seen at the highest masses where the separation of leptons is smallest, with increases in reconstruction efficiency between 30% and 50% depending on the lepton flavor and mass. This translates into a direct improvement in the sensitivity to new physics in this region.

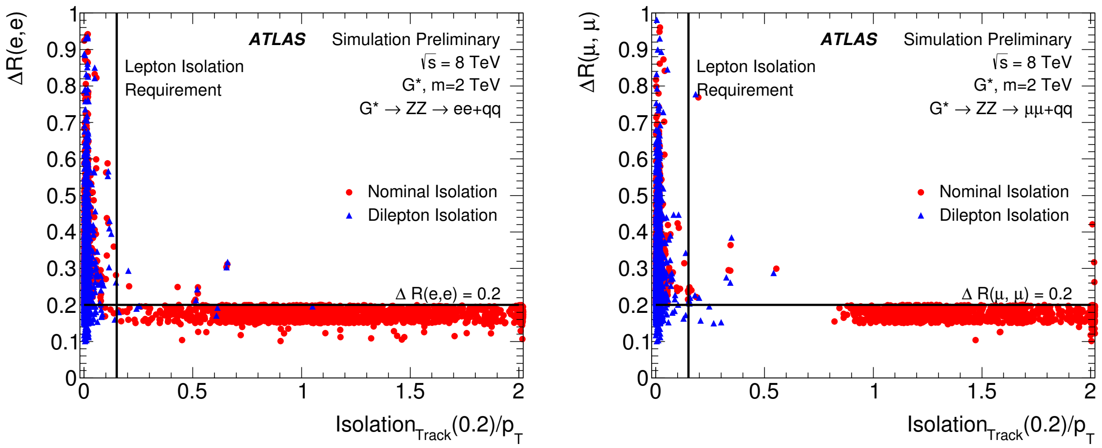

Figure 5.3: Track-based relative p_{T} isolation with a cone size of $R = 0.2$ as a function of the inverse of the distance $\Delta R(\ell, \ell)$ between the two leptons for the 2 TeV gravitons decaying into a $ZZ \to e^+e^- + q\bar{q}$ (left) and $\mu^+\mu^- + q\bar{q}$ (right). The dilepton (nominal) isolation is shown by the blue dots (red triangles). The horizontal line corresponds to $\Delta R(\ell, \ell) = 0.2$ and the vertical line corresponds to the cut applied to the dilepton isolation.

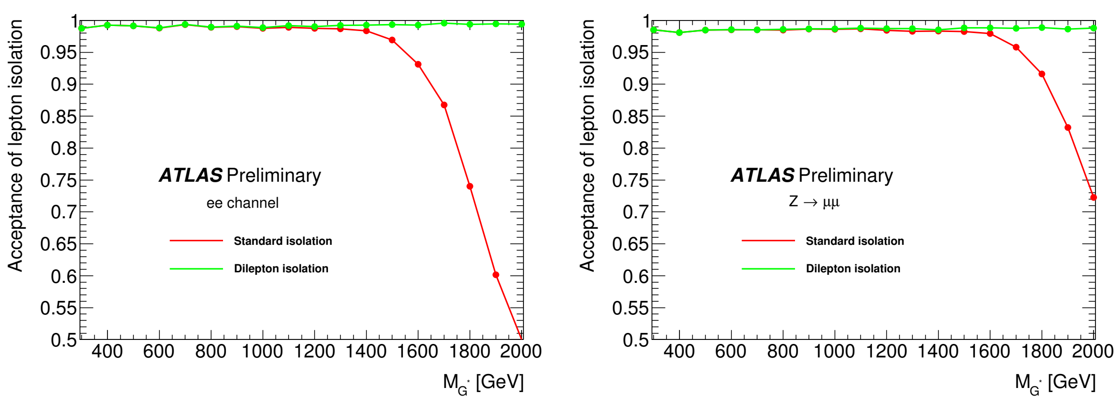

Figure 5.4: The relative acceptance for the single lepton isolation and dilepton isolation as a function of the graviton mass for the electron (left) and muon (right) channels.

5.3.4 Jets

As described in Section 4, jets are intended as proxies for strongly interacting particles involved in the short distance physics that manifest themselves as a collimated spray of hadrons in the experiment. As a result, the signature of a jet is that of multiple charged tracks in the inner detector pointing to many energy depositions in the electromagnetic and hadronic calorimeter. Because the input to any of the jet building algorithms previously described would ideally be the truth hadrons, it is necessary to define a set of physics objects which approximate the properties of those hadrons. Understanding what lies behind this set of inputs is important for the calibration of jets. Two such sets of objects are commonly used in ATLAS; tracks and topoclusters.

- **Tracks** : As with electron and muon reconstruction, tracks are constructed as helical fits to the set of inner detector hits. Using tracks has many benefits including the much finer spatial resolution between tracks compared to the energy depositions in the calorimeter and the ability to use tracks to point back to the origin within the bunch crossing from which it came and thus be used to determine whether a given hadron came from the hard collision or a pileup collision. However, given that the hadron content is primarily pions (π^0, π^+, π^-) only approximately 2/3 of the energy content of the jet is carried by the charged component and so jets measured using tracks have properties that are biased with respect to jets reconstructed using calorimeter information.

- **Topo-Clusters [66]** : Topoclusters are the primary object used to identify hadronic energy depositions in the calorimeter. They are three dimensional groups of cells in the electromagnetic and hadronic calorimeter that are built with an iterative procedure intended to reduce the affect of noise in the calorimeter. The procedure starts by identifying seed cells whose energy is greater than four times the noise threshold for that cell. The surrounding cells that are found with energy greater than two times the noise threshold are then added to the group. This continues until all such cells are added to their respective groups. Lastly, the surrounding cells, regardless of their energy, are added to the group. Given that the second stage of clustering may cause multiple true hadrons to become clustered into a single group, a procedure was designed that splits groups of cells that have multiple local maxima. The resulting groups of clustered and (possibly) split cells constitute the set of topoclusters. The benefit of topoclusters are twofold. The first is that, unlike tracks, the full set of constituents is recorded. The second is that, given both the lateral and longitudinal segmentation of the ATLAS calorimetry, a set of characteristic shower shapes can be used to determine calibrations that reduce the offline size of the calibration correction necessary to restore jets to the truth particle scale.

For a wide majority of cases in this analysis, the inputs for jet finding are topoclusters. Using topoclusters, two types of jets are built. The first set are small-R jets, which are identified as physics objects representing energetic partons and are hereafter referred to as j. These are constructed with the anti-k_t jet algorithm with distance parameter $R = 0.4$. However, because the hadronic calorimeter is a non-compensating calorimeter and because the Monte Carlo does not exactly model the scale of the jet energy in date, multiple corrections are made to correct for these effects. This process involves a correction for the offset of the true collision location from the detector origin, a pileup correction based on the measured energy density produced by pileup on an event-by-event basis, a Monte Carlo based jet energy scale correction that brings the initial measurement into agreement with the truth particle scale, and an in-situ correction from data based on dijet, γ-jet, and Z-jet balance [67]. After this calibration, the jets are required to pass the following set of criteria:

- Reconstructed within $|\eta_{EM}| < 2.1$, where η_{EM} is measured with the centroid of the EM energy deposition defined before any energy correction is applied.
- Transverse momentum of $p_{\mathrm{T}} > 30$ GeV after the full jet calibration.
- These jets must satisfy a set of quality criteria intended to reject jets due to calorimeter spikes, coherent noise, and non-collision backgrounds.
- Satisfy the jet vertex fraction (JVF) cut of $|\mathrm{JVF}| > 0.5$ for jets with $p_{\mathrm{T}} < 50$ GeV. The jet vertex fraction is defined as the ratio of the summed track p_T originating from tracks associated to the jet coming from the primary vertex to the total summed track p_T for all tracks associated to the jet. Jets originating from the hard scatter generally have values close to 1 while jets from pileup collisions have values close to 0, and it can thus be used to reject jets from pileup.

The second set of jets, large-R jets as described in Section 4.2, are identified in this analysis as physics objects representative of W/Z bosons that undergo a hard decay to a $q\bar{q}$ pair which subsequently showers and hadronizes. To build these physics objects, topoclusters are formed into jets using the C/A jet algorithm with a distance parameter of $R = 1.2$. The jets are then split and filtered using the BDRS-A algorithm to identify the two-body substructure of the boson decay coming from signal and remove the effect of pileup contamination. It was found that for the purposes of this search the Monte Carlo calibration produced a response that was sufficiently close to unity that no offline calibration need be applied [2] and systematic uncertainties are assigned that cover the residual deviation from unity in the jet response. The reconstructed jets are then required to pass the following kinematic requirements:

- Reconstructed within $|\eta| < 1.2$. A more restrictive requirement is made on the pseudorapidity for large-R jets because of the method used to derive the systematic uncertainties, described in Section 5.6.4 that uses information from the tracker. Thus, to ensure that the full jet of radius $R = 1.2$ is contained within the tracker, which extends to $|\eta| < 2.5$, it is necessary to restrict the center of the jet to $|\eta| < 1.2$.

- Transverse momentum of $p_{\mathrm{T}} > 100$ GeV.

These two sets of jets are used to reconstruct what are intended to be $W/Z \to q\bar{q}$ decays.

5.4 Optimizing Sensitivity

The goal of searches for new physics is to be as sensitive to new physics as possible. This is achieved by two means. The first is rejecting events that are characteristic of background in favor of signal and the second is by understanding and reducing the uncertainties associated with reconstruction, background estimation, and the signal modelling.

In this search, the first of these goals is achieved by using Monte Carlo modelling of the resonant signal processes and the dominant backgrounds that may hide this signal to

2. Unlike small-R jets which primarily seek to measure the jet energy only, the substructure of large-R jets is essentially performing a measurement of correlated information. Therefore, it is an active field of work within ATLAS to better understand how to perform a proper calibration of multiple jet properties in addition to the jet energy for large-R jets.

determine a set of selection criteria to increase the sensitivity to the presence of a signal. Because the signature has two real leptons, the initial selection requires two same flavor electrons or muons and the very large multijet background is reduced to a negligible level. The requirement that these leptons be of opposite charge is only required in the muon channel so as not to reject events where there may be a mismeasurement of the charge due to a multiple scatterings in the electron channel. The remaining backgrounds are composed of the following:

- $Z + jets$: The dominant background is the Standard Model production of a Z boson in association with partons. It is modeled with Sherpa [68] at leading order and normalized to next-to-leading-order cross section with a k-factor [3]. Although generically referred to as $Z+jets$ from this point forward, it should be noted that this background is composed of three separate components differentiated by the flavor of parton in the final state producing the jets. The three components are produced by applying truth level filters during event generation to exclusively produce samples with bottom quark jets, charm quark jets, and light flavor (up, down, strange, gluon) jets in the final state. This does not significantly affect the following optimization given that flavor information is not used, but it should be noted that these three components are separately modeled in the final result and calculation of sensitivity.

- **Top** : The production of $t\bar{t}$ pairs contributes at the few percent level. The production of a single top quark contributes at the sub-percent level. The $t\bar{t}$ and s-channel single top and Wt production is modeled with $MC@NLO$ [69] with HERWIG [70] for hadronization and JIMMY [71] for underlying event. The t-channel single top production is simulated with AcerMC [72] and PYTHIA for shower and hadronization.

- **Standard Model Diboson** : Standard Model diboson production of $WW/WZ/ZZ$ pairs is simulated with HERWIG and is very small, at the level of a percent or less.

The selection then proceeds by exploiting the high-p_T nature of both the leptonically and hadronically decaying bosons to remove portions of the $Z + jets$ background. The first requirement is made on the dilepton invariant mass, shown in Figure 5.5 for the electron and

3. The term k-factor is short for knowledge factor and is calculated as the correction factor to the cross section based on the comparison of next-to-leading-order cross sections to leading order cross sections.

muon channels separately, requiring $66 < M(\ell\ell) < 116$ GeV. This requirement removes a large fraction of the $t\bar{t}$ and single top background that is manifest as a continuum background in this spectrum. As previously discussed, after this baseline selection, it is beneficial to divide the signal region into exclusively selected categories of events with kinematics tuned for optimal sensitivity in a given region. In addition to the primary division based on the topology of the hadronic system, the resolved regime is further subdivided into two kinematic regions with different selection criteria that focus on different mass regions. Therefore, there are three selection regions in full:

- **Resolved Low-p_{T} Region** : $Z \rightarrow \ell\ell$ + low-p_{T} $W/Z \rightarrow jet + jet$, covering typically $300 < M(X) < 600$ GeV
- **Resolved High-p_{T} Region** : $Z \rightarrow \ell\ell$ + high-p_{T} $W/Z \rightarrow jet + jet$, covering typically $600 < M(X) < 1000$ GeV
- **Merged Region** : $Z \rightarrow \ell\ell$ + very high-p_{T} $W/Z \rightarrow FatJet$, covering typically $M(X) > 1000$ GeV

The values determined to be optimal for the selection criteria are determined based on ROC curves, discussed in Appendix C, similar to those used in the studies of boson jet identification but more suited to defining an optimal single selection value on a quantity for implementation in the analysis.

5.4.1 The Resolved Regime

The resolved regime is defined by a high-p_T $Z \to \ell\ell$ decay and a high-p_T $W/Z \to q\bar{q}$ decay reconstructed as two small-R jets. To identify these events, an initial selection is made on the transverse momentum of the dilepton system, shown in Figure 5.5, requiring it to be greater than 100 GeV for the low-p_T region and greater than 250 GeV for the high-p_T region which is found to be optimal since $M(X)$ is highly correlated with the boost of the Z boson. To identify the $W/Z \to q\bar{q}$ decay, an initial selection is made to require that the number of small-R jets, shown in Figure 5.6, is at least two. Subsequent selections are made on both the invariant mass ($M(jj)$) and transverse momentum ($p_T(jj)$) of the two highest p_T jets in the system system. The optimal signal window was determined by examining both signal models given that in one, the dijet invariant mass, shown in Figure 5.7, is intended to reconstruct a Z boson while in the other it is intended to reconstruct a W boson. From this, the rather broad window of $70 < M(jj) < 110$ GeV was found to be sufficiently optimal to accommodate both signals for both the low-p_T and high-p_T regions. Lastly, a selection is made on the dijet transverse momentum transverse momentum , shown in Figure 5.7, that is found to be optimal at values symmetric to those used for the dilepton transverse momentum; $p_T(jj) > 100$ GeV for the low-p_T region and $p_T(jj) > 250$ GeV for the high-p_T region. This selects a subset of events with the desired signal-like characteristics, similar to those shown in Figure 5.8 in which the presence of two high-p_T leptons and jets that are produced back-to-back in the transverse plane can clearly be seen.

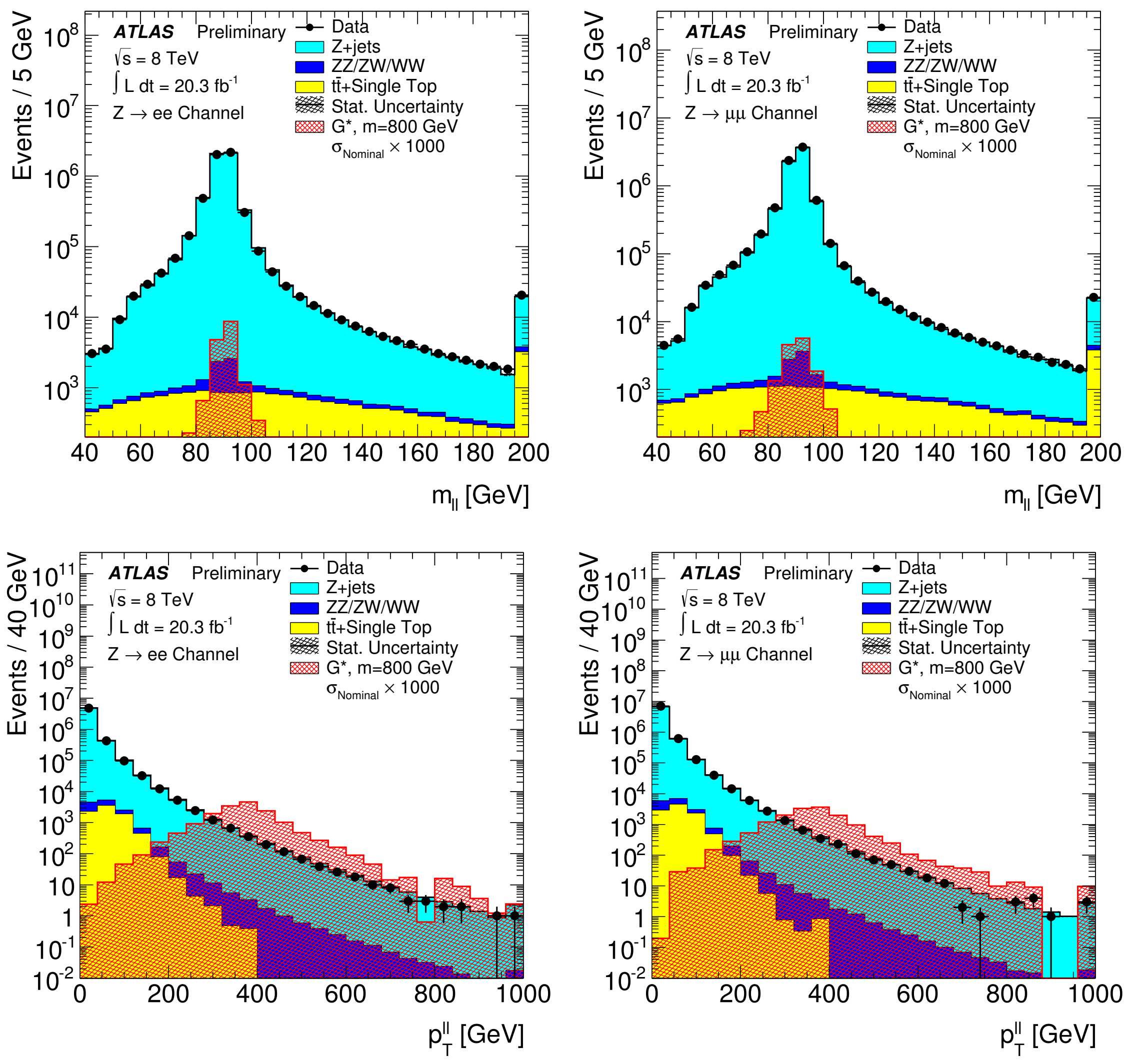

Figure 5.5: Comparison of the data with the background prediction for the dilepton mass (top) and p_{T} (bottom) distributions after applying only object selection cuts. The left (right) column shows the distributions for the electron (muon) channel. The rightmost bin includes events in overflow.

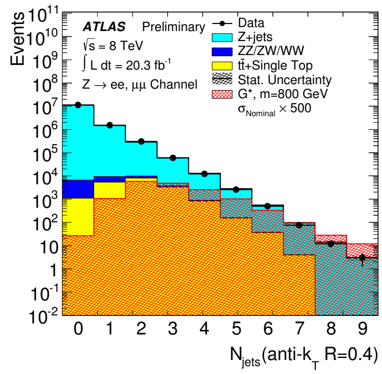

Figure 5.6: Data and background prediction for the number of jets reconstructed with the anti-k_t algorithm with R=0.4 used in the resolved regions. The electron and muon channels are combined. The rightmost bin includes events in overflow.

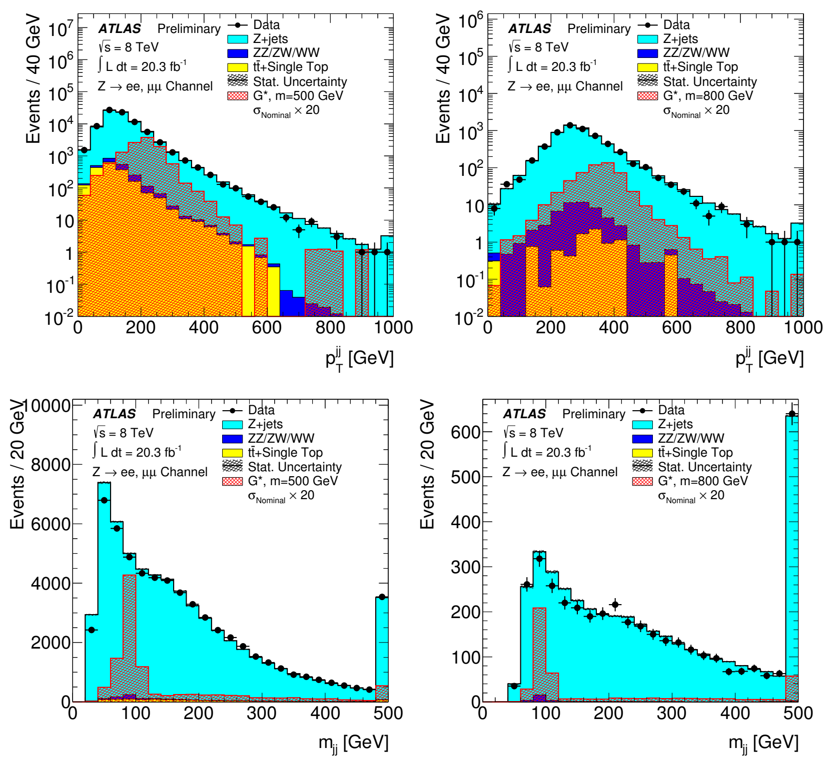

Figure 5.7: Comparison of the data with the background prediction for the dijet p_{T} (top) and mass (bottom) distributions for the combined electron and muon channels. The left (right) column shows the distributions in the low-p_{T} (high-p_{T}) resolved regions. The rightmost bin includes events in overflow.

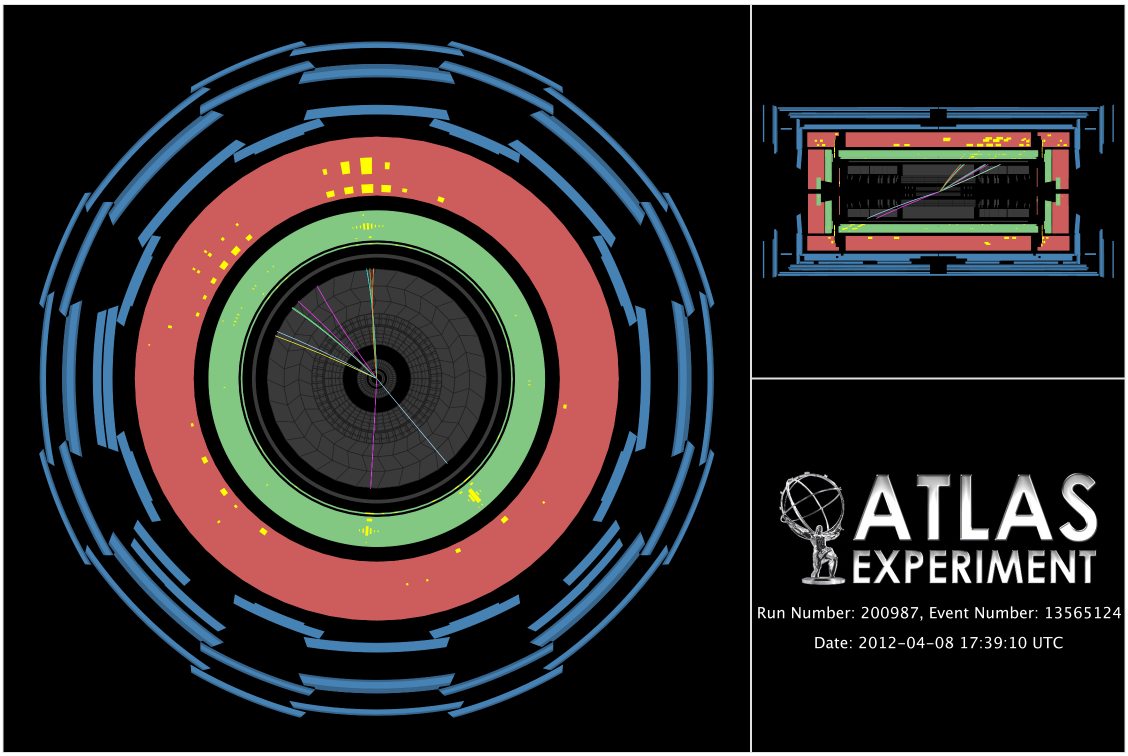

Figure 5.8: Example event passing all signal region selection criteria in the resolved region for the electron channel. The left image shows the (r, ϕ) projection of the event as recorded in the ATLAS detector with the inner most region being the inner detector with reconstructed charged tracks, the green and red rings the electromagnetic and hadronic calorimeters respectively with energy depositions shown in yellow, and the outermost blue shapes the various layers of the muon spectrometer system. The upper right image shows a (z, η) projection of the event with the same basic layout, but shown from the side. The four body invariant mass, $m(eejj)$, for this event is 665 GeV.

5.4.2 The Merged Regime

The merged regime is defined by a high-p_T $Z \rightarrow \ell\ell$ decay and a high-p_T $W/Z \rightarrow q\bar{q}$ decay reconstructed as a single large-R jet. To identify these events, an initial selection is made on the transverse momentum of the dilepton system, requiring it to be greater than 400 GeV, higher than the resolved regime because this region is intended to probe larger masses. To identify the $W/Z \rightarrow q\bar{q}$ decay, an initial selection is made to require that the number of large-R jets, shown in Figure 5.9, is at least one. The highest p_T large-R jet is then assumed to be the most likely candidate for reconstructing the W/Z boson decay and so an initial selection is made on the transverse momentum of this jet, shown in Figure 5.9, to be greater than 400 GeV. As described at much greater length in Section 4.4, a variety of techniques are available to determine whether a large-R jet comes from the decay of a boson. The two criteria used for this search are to select boson jets based on the invariant mass of the jet ($M(J)$) and subjet momentum balance ($\sqrt{y_f}$). It was found that the selection criteria for the invariant mass of the jet, shown in Figure 5.10, from $70 < M(J) < 110$ GeV was optimal, as was the case for the dijet invariant mass selection in the resolved region. Lastly, the selection on the substructure moment, the subjet momentum balance, shown in Figure 5.10, was found to be optimal at $\sqrt{y_f} > 0.45$. This full selection leads to a subset of events with the desired signal-like characteristics, similar to those shown on the left of Figure 5.11, in which the presence of two high-p_T leptons recoiling off a single large-R jet whose energy deposition in the calorimeter (upper right of Figure 5.11) is indicative of the hard two body decay of a massive object is clearly visible.

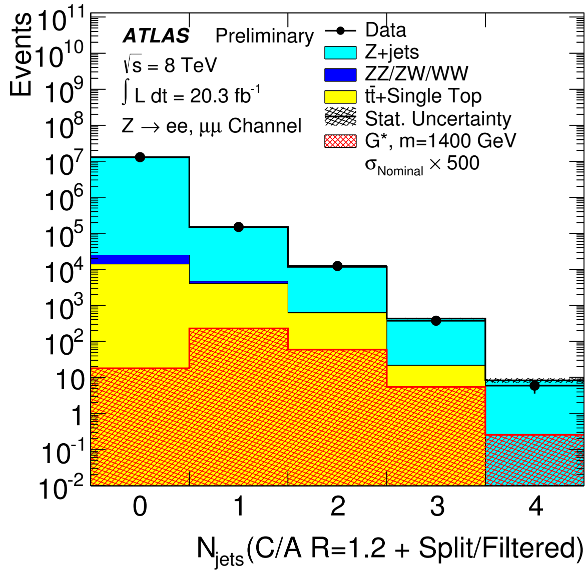

Figure 5.9: Comparison of data with the background prediction for the number of jets reconstructed with the Cambridge-Aachen algorithm with R=1.2 and groomed with the BDRS-A algorithm used in merged region (left) and for the leading large-R jet p_{T} (right). The electron and muon channels are combined. The rightmost bin includes events in overflow.

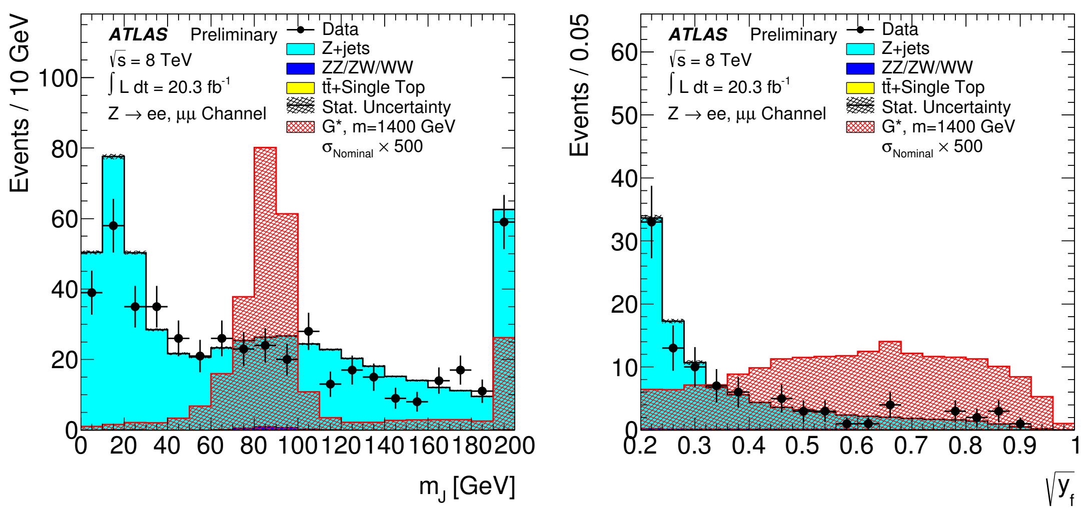

Figure 5.10: Comparison of the data with the background prediction for the leading large-R jet mass (left) and momentum balance (right) distributions in the merged region. The electron and muon channels are combined. The rightmost bin includes events in overflow.

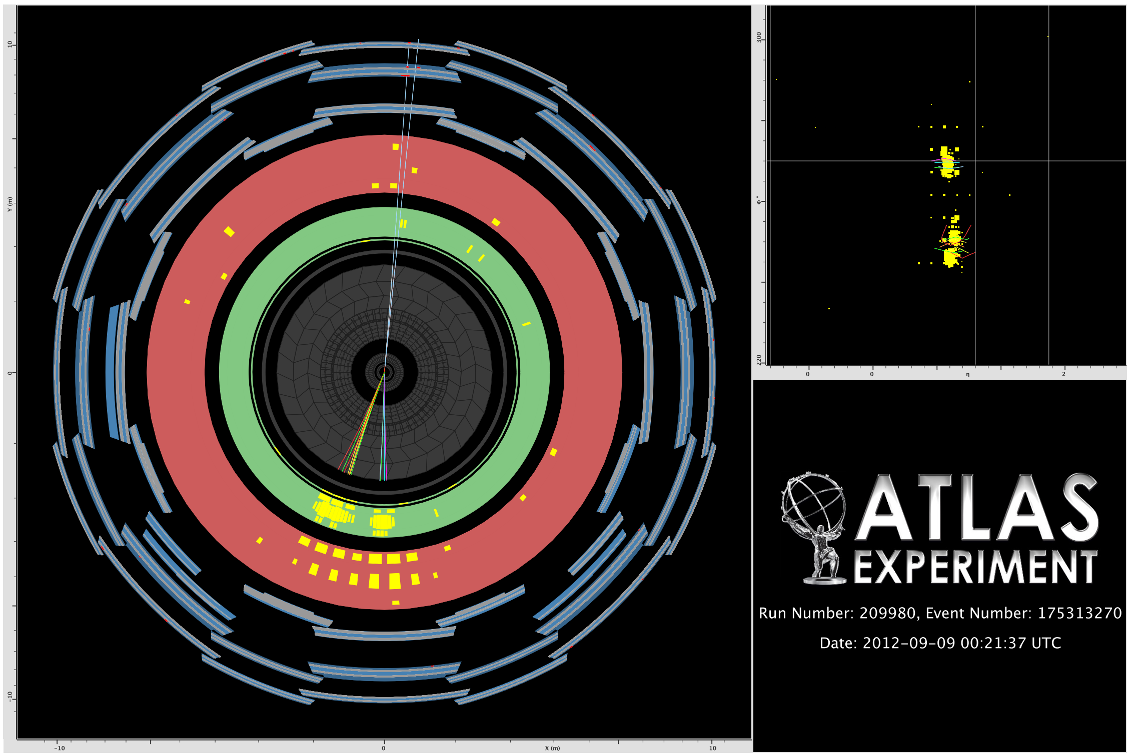

Figure 5.11: Example event passing all signal region selection criteria in the merged region for the muon channel. The left image shows the (r, ϕ) projection of the event as recorded in the ATLAS detector with the inner most region being the inner detector with reconstructed charged tracks, the green and red rings the electromagnetic and hadronic calorimeters respectively with energy depositions shown in yellow, and the outermost blue shapes the various layers of the muon spectrometer system. The muons can be seen as two blue tracks on the top half of this image and the large-R jet as the cluster of yellow cells near the bottom of the image. The upper right image, however, shows an (η, ϕ) projection, with η on the horizontal axis and ϕ on the vertical axis, of the calorimeter information, with calorimeter cell energies proportional to the size of the yellow block, in the local region of the leading large-R jet in the event used to reconstruct the three body invariant mass. The three body invariant mass, $m(\mu\mu J)$, for this event is 1086 GeV.

5.4.3 Signal Region

In full, the three signal regions are defined by the initial trigger selection described in Section 5.1, a set of quality criteria applied to data, and the criteria outlined in Table 5.1. To allow for the statistical combination of the sensitivity of these selection regions, the selection regions are made exclusive with priority given to the selections that target higher masses, checking first if an event is selected by the merged region, then the resolved high-p_T region, and finally the resolved low-p_T region, only categorizing each event as belonging to one signal region.

Resolved low-p_T	Resolved high-p_T	Merged
$N(e \text{ or } \mu)$==2	$N(e \text{ or } \mu)$==2	$N(e \text{ or } \mu)$==2
$66 < M(\ell\ell) < 116$ GeV	$66 < M(\ell\ell) < 116$ GeV	$66 < M(\ell\ell) < 116$ GeV
$p_T(\ell\ell) > 100$ GeV	$p_T(\ell\ell) > 250$ GeV	$p_T(\ell\ell) > 400$ GeV
$N(j) \geq 2$	$N(j) \geq 2$	$N(J) \geq 1$
$p_T(jj) > 100$ GeV	$p_T(jj) > 250$ GeV	$p_T(J) > 400$ GeV
$70 < M(jj)M < 110$ GeV	$70 < M(jj)M < 110$ GeV	$70 < M(J)M < 110$ GeV
		$\sqrt{y_f} > 0.45$

Table 5.1: Table summarizing the signal region selection criteria used to select events with which to perform the search. These criteria are applied in addition to the trigger and preselection data quality requirements.

For each signal region and both lepton flavors, the four body or three body invariant mass is formed for the resolved and merged regions separately as shown in Figure 6.1. This is the spectrum that is used to search for a resonant excess as described in Section 6. To get a sense of the sensitivity of the analysis to a new physics signal, two primary figures of merit are evaluated. The first is the acceptance times efficiency, shown on the top in Figure 5.12, which indicates the fraction of the initial signal from the benchmark model, in this case the bulk Randall-Sundrum graviton, that enters the signal region. The second is the $S/\sqrt{B}$ for various graviton masses of the benchmark signal, shown on the bottom in Figure 5.12, calculated for a given mass point by taking a 2σ window around the mean reconstructed mass and counting the number of events, normalized to the nominal theoretical cross sections and 20.3 fb^{-1} used in the analysis, for signal (S) and background (B). These two plots summarize two key features of the analysis. The first is that sensitivity for different signal masses is mainly provided by one of the three exclusive signal regions, with the merged region being a necessary addition in order to probe signals with masses greater than approximately 1 TeV. The second is that, although using modified jet algorithms allows for hadronic decays of bosons to be probed above 1 TeV, when considering leptonic decays of Z bosons of high enough transverse momentum (e.g. for $M(X) > 1.6$ TeV), it becomes necessary to reconsider the definition of a $Z \to \ell\ell$ decay and treat the dilepton system as a boosted object. In doing so, the acceptance of such decays can be increased leading to an overall increase in sensitivity.

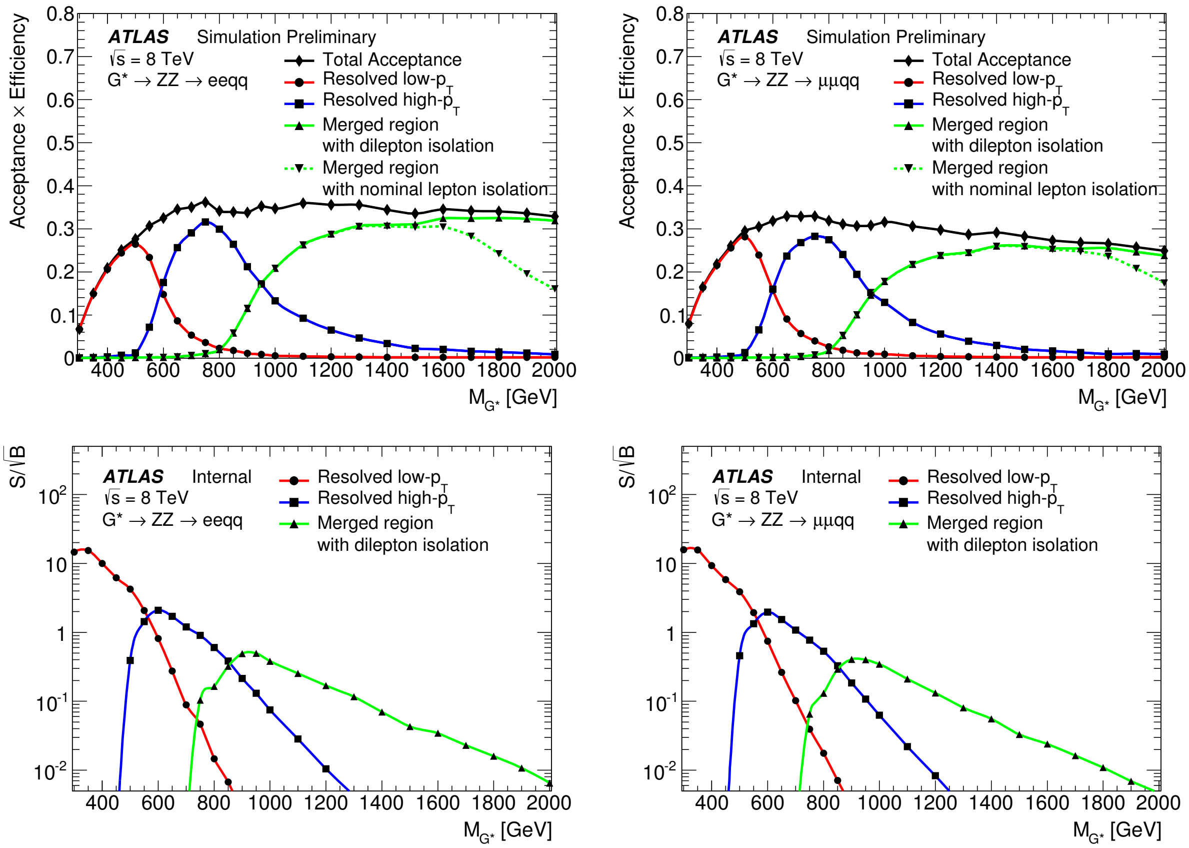

Figure 5.12: Signal acceptance times efficiency (top) and $S/\sqrt{B}$ sensitivity (bottom) for the low-p_T resolved, high-p_T resolved, and merged signal regions for the bulk Randall-Sundrum graviton signal for the electron (left) and muon (right) channels.

5.5 Understanding the Background

The goal of this search is to find any significant deviation of the measured data from the prediction of known standard model processes as measured in ATLAS. Therefore, it is crucial to accurately model those backgrounds and, if any mismodelling due to sources other than the presence of a signal exist, appropriately correct the background estimation. To achieve this requires that a region of phase space that contains a negligible amount of signal contamination exists in which the description of the data by the nominal Monte Carlo used to perform the optimization described in Section 5.4 can be evaluated and improved. These regions are called "control regions" and should be designed to be as kinematically identical to the signal region as possible. In this analysis, the control regions that are used are defined with the same signal region selections but with the selections on the mass of the hadronic system $M(jj)$ or $M(J)$ inverted. Explicitly, for the two resolved regions, this means that events are selected that fulfill $M(jj) < 70$ GeV or $M(jj) > 110$ GeV instead of $70 < M(jj) < 110$ GeV and for the merged region this means that events must fulfill $M(J) < 70$ GeV or $M(J) > 110$ GeV instead of $70 < M(J) < 110$ GeV.

The four body and three body invariant mass spectra are formed as in Figure 5.13, and in general show that the dominant $Z + jets$ background estimation models the data well. However, there are slight shape and normalization differences that may be a result of a number of sources including mismodelling of physics objects reconstructed in Monte Carlo and theoretical sources such as mismodelling of proton PDF's. This mismodelling is parameterized in two ways. The first is through a single overall normalization correction that is computed by taking the ratio of the data to the $Z + jets$ prediction, after subtracting the contamination from other background sources, in each of the six control regions. The second is a linear shape correction, derived by fitting a function $f(x) = mx + b$, where x is either $M(\ell\ell jj)$ or $M(\ell\ell J)$, which is constrained to preserve the overall normalization of the $Z + jets$ background, to the ratio of data to Monte Carlo in Figure 5.13. Because any mismodelling is presumably dominated by the measurement of the jets, this linear correction is derived only for each selection region, merging together the electron and muon channels.

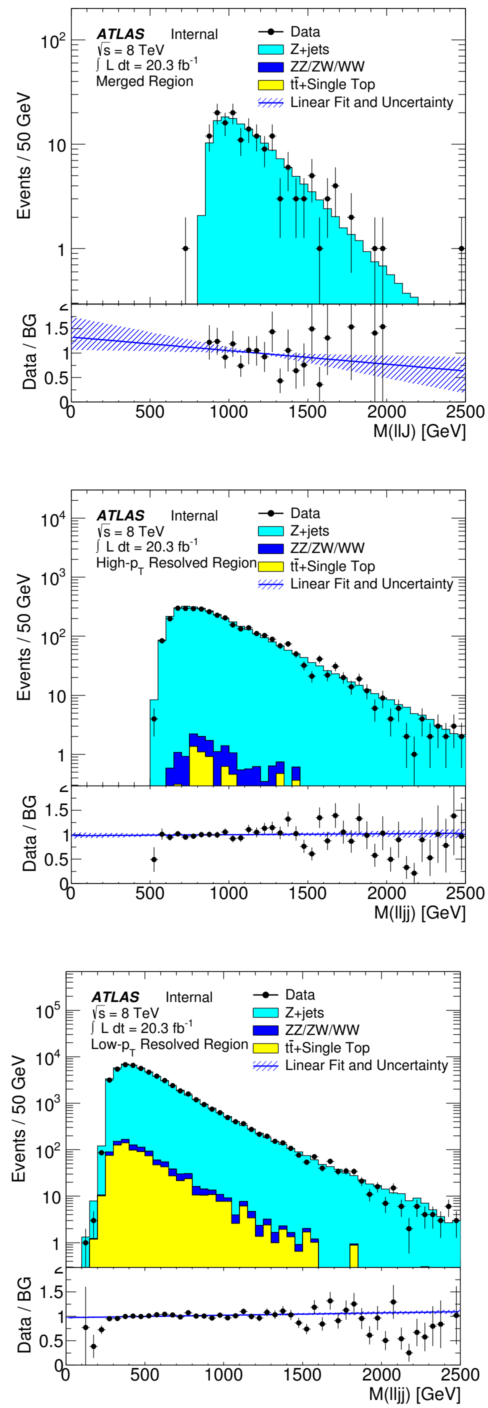

Figure 5.13: The three body (top) and four body mass (middle and bottom) distributions in the control regions described in Section 5.5 for the data and background predictions. The bottom part of each plot shows the ratio of the data to background. The blue line shows the result of a linear fit to the ratio and the fit uncertainty is given by the hatched area.

These two corrections, summarized in Figure 5.14 and Table 5.2, are used to correct the modelling of the dominant $Z + jets$ in the signal regions, again as a function of $M(\ell\ell jj)$ and $M(\ell\ell J)$. Lastly, the constraints on the $Z + jets$ background imposed by this method allow the uncertainty to be constrained, not by Monte Carlo based uncertainties but by the precision to which the derivation of the shape and normalization correction are known, as indicated in Table 5.2.

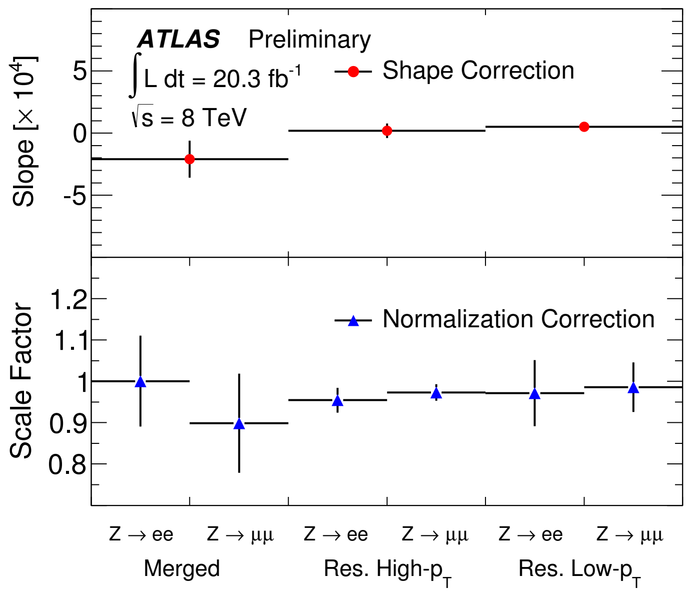

Figure 5.14: The normalization and shape correction factors for the simulated $Z + jets$ Monte Carlo, derived for the electron and muon channel control regions.

Correction		Res. Low-pT	Res. High-pT	Merged
Shape ± Uncer.		-0.00021 ± 0.00015	1.95e-05 ± 5.88e-05	4.98e-05 ± 1.94e-05
Norm. ± Uncer.	$Z \to ee$	1.00 ± 0.11	0.95 ± 0.024	0.97 ± 0.073
	$Z \to \mu\mu$	0.90 ± 0.11	0.97 ± 0.024	0.99 ± 0.073

Table 5.2: The normalization and shape correction factors for the simulated $Z + jets$ Monte Carlo, derived for the electron and muon channel control regions.

5.6 Systematic Uncertainties

The physics processes being measured have inherent statistical fluctuations and therefore the extent to which the background and signal can be understood is limited. In addition to the statistical uncertainty, however, there are a number of systematic uncertainties due to the limited knowledge of many sources of mismeasurement of the physics objects described in Section 5.3 and theoretical limitations of the inputs entering the analysis. A good understanding of these sources of uncertainty is essential to having a robust determination of the sensitivity to possible deviations from the Standard Model due to the presence of new physics. Described here are the dominant sources of uncertainty that are taken into account in the fit described in Section 6.

5.6.1 Electrons

There are three sources of uncertainty resulting from the use of electrons in the search. The first is on the reconstruction efficiency correction factors. The uncertainties are derived using the prescription described in [60] and are on the order of a percent or less in the kinematic regime of interest. The second two uncertainties are those due to mismeasurement of the electron energy scale and resolution, described in [60, 62]. This results primarily from the uncertainty in the amount of material in the simulation versus the true detector for the energy scale and the uncertainty in the modelling of the sampling in the calorimeter for the resolution. When taking into consideration all uncertainties, the electron energy is found to be uncertain at the level of approximately 1% and less than 1% for the scale and resolution respectively. These uncertainties are negligible on the background as they enter through the uncertainty on the subdominant top and diboson backgrounds, and not through the $Z + jets$ background which is constrained in the control regions as described in Section 5.5. Therefore, they primarily affect the analysis through the signal modelling and have an effect of less than a percent.

5.6.2 Muons

The sources of uncertainty coming from the use of muons in this search are the same as those for the electrons. One is from the uncertainty on the derivation of the reconstruction efficiency corrections and two are from the mismeasurement of the muon momentum scale and resolution. The derivation of the uncertainty on the reconstruction efficiency scale factors is described in [61] and, using a sample of $Z \rightarrow \mu\mu$ events, is found to be less than a percent with an additional uncertainty of $1\% \times p/[TeV]$ added for extrapolation to high momentum. The uncertainty on the muon momentum scale and resolution are described in [61, 65] and are derived using $Z \rightarrow \mu\mu$ events. A small momentum dependence of the momentum scale correction leads to a nonclosure[4] and requires a systematic of less than a percent and so to be conservative in the effect that the scale correction may have in the analysis, the effect is evaluated by completely turning off the muon momentum scale correction. The momentum resolution uncertainty is determined independently for tracks in the ID, MS, and combined ID and MS tracks and is taken into account using two separate uncertainties, one for the MS component and one for the ID component. These uncertainties affect the analysis through the signal modelling and amount to an effect on the percent level.

5.6.3 Small-R Jets

The uncertainty on the small-R jet energy scale is determined by studying the jet response using Monte Carlo samples with varied theoretical conditions (e.g hadronic shower model) and detector configurations (e.g. detector material) and further by using in-situ calibration methods in dijet, $\gamma + jet$, $Z + jets$ and multijet events as described in [67]. In total, there are 56 sources of uncertainty that enter the full jet energy scale uncertainty. However, in order to simplify the application of these uncertainties while accounting for correlation among various systematic uncertainties for in-situ calibration techniques, a reduced set of uncertainties is provided that combines sources of uncertainty where appropriate. In this analysis, the sources of uncertainty for the jet energy scale that are considered are

- 4 sources related to modeling and theoretical uncertainties in the Monte Carlo used for the derivation
- 3 sources related to limited statistics in the derivation of the jet energy scale
- 3 sources related to detector uncertainties

4. The term nonclosure refers to disagreement observed between data and calibrated Monte Carlo in a sample that is the same as that used to derive the calibration.

- 2 sources related to *mixed* detector/modeling/theoretical uncertainties
- 2 sources related to η-intercalibration uncertainty
- 1 source related to single hadron response uncertainties from test beam data for very high-p_T jets
- 1 source related to Monte Carlo nonclosure uncertainties (only applicable when using Monte Carlo samples in which the detector response is modelled with the ATLFASTII detector simulation [73])
- 4 sources related to pileup correction uncertainties
- 2 sources for uncertainties related to the flavor composition of the sample of jets and the difference in response between quark, gluon, and b-jets

The jet energy resolution uncertainty is determined in-situ with two different methods: the dijet p_T balance and bisector techniques, which give consistent results as documented in [74]. As in the case of leptons, these uncertainties have a negligible affect on the background uncertainty. The affect on the signal modelling only enters in the resolved regions where small-R jets are used, and is on the order of a percent or less.

5.6.4 Large-R Jets

Three selections are made on the large-R jets used in the merged region and described in Section 5.3.4; transverse momentum, invariant mass, and subjet momentum balance. Therefore, it is necessary to account for the uncertainty in both the scale and resolution of these variables. Although the topic of how to most correctly quantify these uncertainties and their correlations is an active area of work in ATLAS, a well defined method does exist to quantify individual uncertainties on the scale of any measurement associated with a jet. This method, a more detailed description of which can be found in [37], relies on the ability to reconstruct jets using both topoclusters from the calorimeter (calo jets) and tracks from the inner detector (track jets). In this sense, the same object is being measured in two separate subsystems of ATLAS and a comparison of these two measurements can elucidate any systematic mismodelling in the Monte Carlo. To perform this comparison for a given quantity, for instance the jet mass, the average of the ratio of the measurement of that quantity using the track jet to that using the calo jet, $r^m = \frac{m^{calojet}}{m^{trackjet}}$[5], is computed and parameterized as a function of some kinematic variable (e.g $p_T(jet)$). A comparison is then made between data and Monte Carlo for this measured quantity by computing $R^m = \frac{r^m_{data}}{r^m_{MonteCarlo}}$ and any residual deviation from unity is taken as a measure of the experimental systematic uncertainty on the given quantity. Two important assumptions are implicitly made here. The first is that any theoretical uncertainty (e.g. parton shower) will affect the track and calo measurement in a correlated way and so will cancel out when taking the first ratio. The second is that the detector related systematic uncertainties associated with the track jet and calo jet measurements are not correlated in such a way that they cancel, and lead to an unrealistically small estimate of the uncertainty. Under these assumptions, the uncertainty is found, as shown in Figure 5.15, to be 2% for the jet energy scale, 3% for the jet mass scale, and 2% for the scale uncertainty on the subjet momentum balance, independent of the transverse momentum of the jet.

The uncertainty on the jet energy resolution, jet mass resolution, and momentum balance resolution is not directly measured in [43]. However, studies of the W boson mass peak observed in high-p_T $t\bar{t}$ data samples indicate that it is well described by Monte Carlo simulation both in peak location and shape, and are used to estimate the uncertainty on the resolution in [42]. A similar agreement is observed also for the $\sqrt{y_{\mathrm{f}}}$ distributions in multijet events and a conservative uncertainty of 20% on the jet energy, mass, and subjet momentum resolution are applied at this point with ongoing studies working to better understand how to better quantify this. These uncertainties lead to an uncertainty on the signal modelling that is on the order of less than a percent.

5. Note that the average value of this comparison for a given varable will not necessarily be close to one because track jets only contain the charged constituents of the jet.

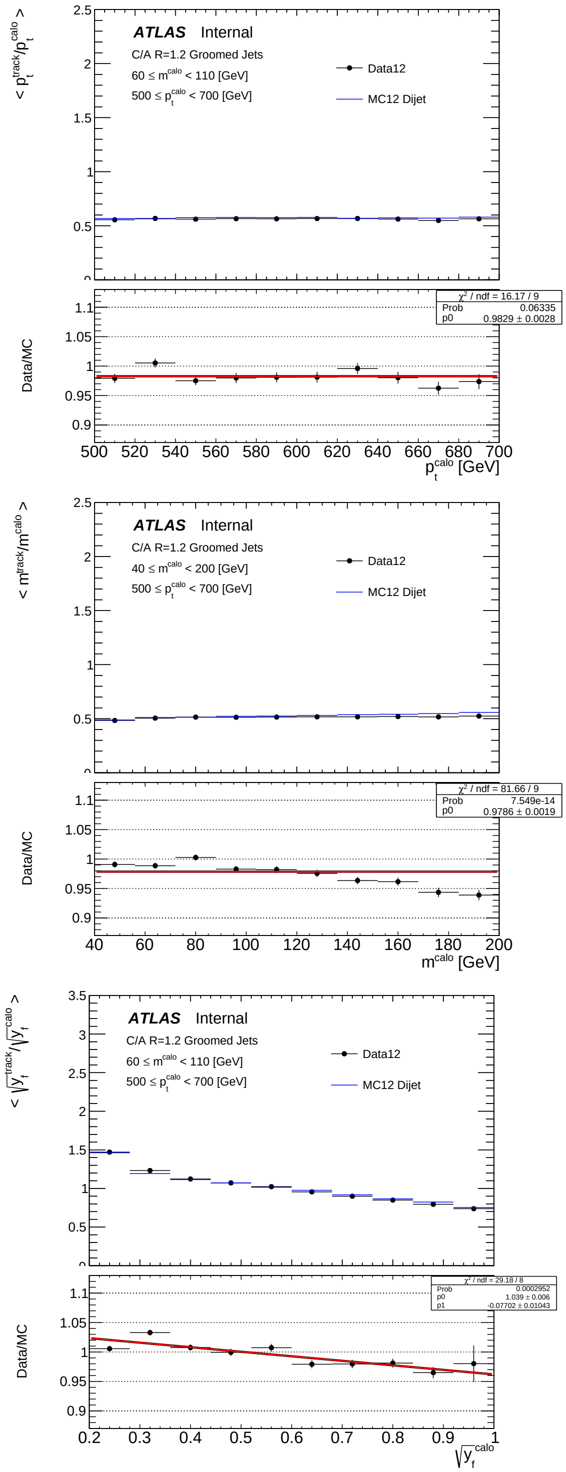

Figure 5.15: The track jet to calo jet double ratio comparison in data and dijet Monte Carlo used to estimate the uncertainty on the scale of the large-R jet energy, mass, and $\sqrt{y_f}$. From these studies, uncertainties are taken to be 2% for the jet energy scale, 3% for the jet mass scale, and 2% for the scale uncertainty on the subjet momentum balance.

5.6.5 Background Constraints

As described in Section 5.5, the description of the $Z + jets$ background is initially taken from Sherpa Monte Carlo, normalized to next to leading order cross section, and corrected both in shape and normalization by scale factors determined using data to Monte Carlo comparison in control regions. The derivation of both of these corrections come with associated uncertainties based on the available statistics in the control regions. In the resolved low-p_T region, when examining events in the low mass sideband, the normalization correction differs from that in the high mass sideband by more than one standard deviation and so the uncertainty on this normalization correction is taken to be the maximal difference between the central value (combined sidebands) and either the low mass sideband or the high mass sideband. However, due to lack of statistics in the resolved high-p_T and merged regions, the corrections factors derived by examining the low mass and high mass sidebands separately are consistent with each other and so the uncertainty in the derivation of these correction factors is purely based on the statistical uncertainty. In full, these uncertainties are summarized in Table 5.2 and two uncorrelated sources of systematic uncertainty are assigned to the $Z + jets$ background; one for the normalization correction and one for the shape correction. This is the dominant source of systematic uncertainty on the background estimation shown in the band in Figure 6.1.

5.6.6 Additional Uncertainties

In addition to the previously described systematic uncertainties, there are a number of subdominant systematic uncertainties that are taken into account. These uncertainties come from the following sources:

- **Luminosity**: The luminosity is measured in beam-separation scans performed following the procedure described in [75] and has an uncertainty of 2.8%. This uncertainty applies only to the signal, top, and diboson predictions as the $Z + jets$ background normalization is determined by a fit to the data.

- **Parton Distribution Functions**: One of the inputs to Monte Carlo generation are parton distribution functions (PDFs), which provide information concerning the momentum fraction carried by the parton entering into the hard collision. The uncertainty on signal acceptance associated with this input to Monte Carlo simulations is assessed by comparing multiple determinations of PDFs. Nominally, the benchmark bulk Randall-Sundrum graviton sample used in the analysis is generated using the CTEQ6L1 PDF set. The uncertainty due to this choice is derived by comparing the variation in signal acceptance when using CTEQ6L1 to that obtained when using the alternative MSTW2008LO PDF set. Furthermore, the MSTW2008LO set of PDF has a set of 40 variations representative of the error associated with the actual procedure implemented to extract the PDF's from data, and the signal acceptance variation between these 40 sets is used as a second source of PDF uncertainty. These two sources are added in quadrature and results in an overall uncertainty of 1-2% depending on the signal mass.

- **Initial and Final State Radiation**: The initial and final state radiation (ISR/FSR) of gluons in high-mass diboson resonant production could bring additional systematic uncertainty in the signal acceptance as those additional jets would affect the jet multiplicity and kinematic distributions leading to an ambiguity in the jet assignment of hadronic W/Z decay. The level of ISR/FSR is controlled in Monte Carlo by a number of tunable parameters (e.g.α_s). The uncertainty on this affect is investigated by producing $G^* \to ZZ \to \ell\ell q\bar{q}$ samples varying the ISR/FSR parameters of parton showering in `PYTHIA8` and examining the variation of signal acceptance relative to the nominal acceptance at truth level. The relative acceptance variation obtained from these samples is at maximum approximately 5% across the mass range for all signal regions and so a flat 5% uncertainty on signal acceptance is assigned from ISR/FSR uncertainty.

- **LHC Beam Energy**: The LHC beam energy at $\sqrt{s} = 4$ TeV operation has been measured in p-Pb run in January-February 2013 [76]. The result was 3988 ± 5(stat) $\pm$ 26(syst) GeV per beam, which is consistent with the nominal energy of 4 TeV within the uncertainty of 0.65%. This possible shift in the beam energy could affect acceptance for the signal with slightly modified parton luminosity distributions from those used in the signal simulation performed at 4+4 TeV. The affect on the signal acceptance is checked by modifying the beam energy (conservatively) by ± 40 GeV ($\pm 1\%$ of the nominal beam energy) in the W' signal production and checking the variation of signal acceptance relative to the nominal acceptance at truth level. The relative variation in cross section is consistent with unity and the variation on signal acceptance varies between 1-4% and so a flat systematic on uncertainty signal acceptance is assigned due to LHC beam energy uncertainty.

Chapter 6
Results

After defining an optimally sensitive signal region, estimating the various components of standard model backgrounds, and understandings the sources of systematic uncertainty associated with that background and the benchmark signal, the search proceeds by unblinding the data in the signal region, checking for consistency between the data and the background estimation and quantifying any excess. In the absence of an excess, an upper limit on the presence of new physics signals in terms of the production cross section times branching fraction of a new physics signal is set. In the context of a specific new model, this can be translated into a lower bound on the mass of the particle that is introduced.

6.1 Searching in the Signal Region

The first step in this process is to unblind the data in the signal region and compare the invariant mass spectra ($M(\ell\ell jj)$ and $M(\ell\ell J)$) in data with that from the expected backgrounds. As shown in Figure 6.1 and Table 6.1, the comparison indicates that the data is relatively well described by the background estimation where the dominant $Z + jets$ component has been constrained using the control regions as described in Section 5.5. If a resonant new physics signal were present, the expected shape would be similar to that indicated by the bulk Randall-Sundrum graviton template that has been added to the background spectra. However, the deviations observed are either covered by the systematic uncertainties described in Section 5.6, are too narrow for the experimental resolution of a resonant signal indicating that they are likely statistical fluctuations, or broad excesses (e.g. in the muon channel merged signal region) which is indicative of a mismodelling of the background.

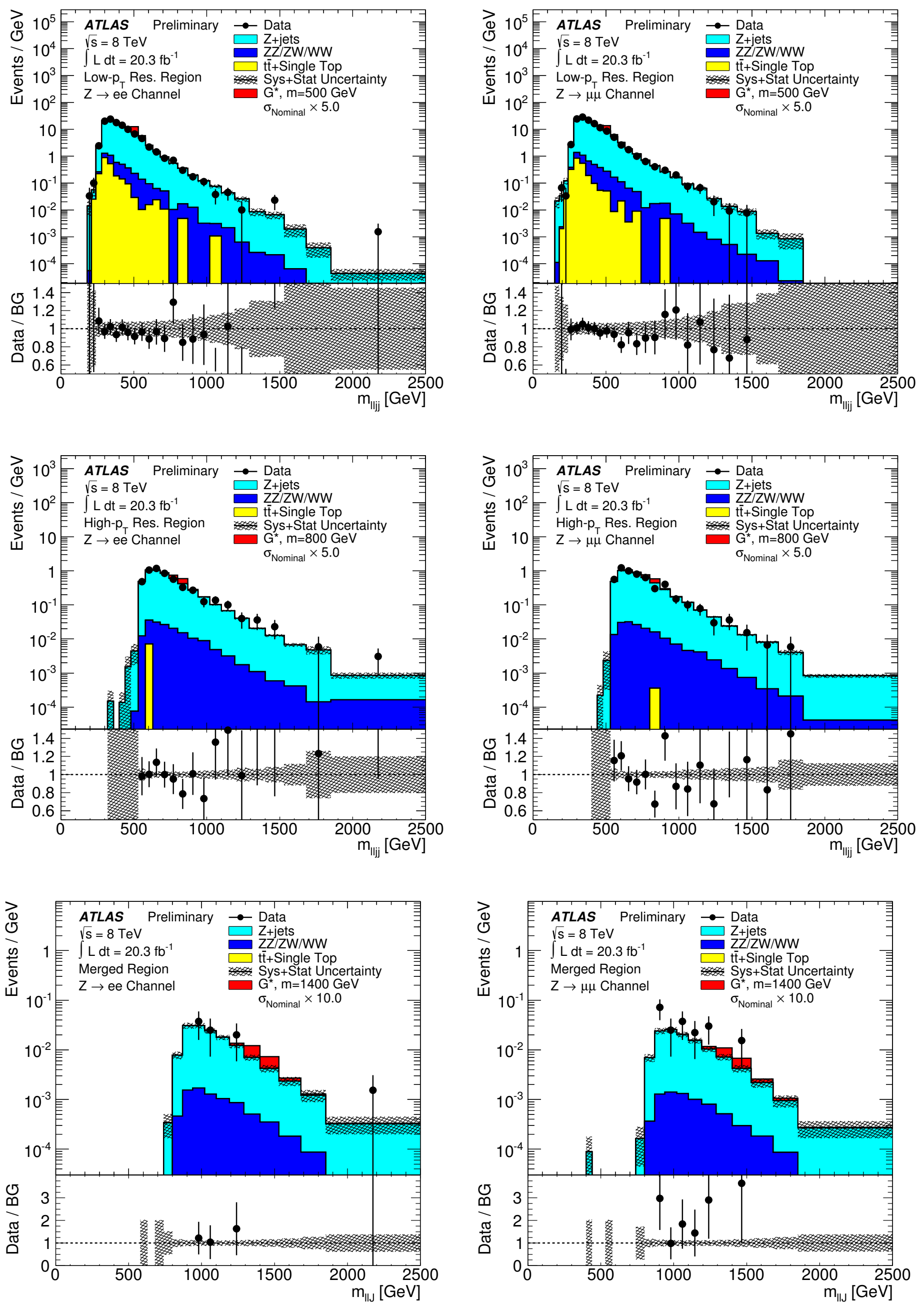

Figure 6.1: Comparison of the data with the background prediction for the $m_{\ell\ell jj}$ distributions in the low-p_{T} (top) and high-p_{T} (middle) resolved regions, and for the $m_{\ell\ell J}$ distributions in the merged region (bottom) in the electron (left) and muon (right) channels. The shaded band gives the total background uncertainty obtained by adding the statistical and systematic uncertainties in quadrature. A representative signal is overlayed to show how an excess would appear on top of the background.

Sample	LR	HR	MR
$Z + jets$	$9460 \pm 40 \pm 660$	$591 \pm 4 \pm 15$	$20.9 \pm 0.3 \pm 2.3$
$WW/WZ/ZZ$	$234 \pm 4 \pm 22$	$20.6 \pm 0.3 \pm 1.4$	$1.38 \pm 0.02 \pm 0.13$
$t\bar{t}$ + Single t	$175.3 \pm 9.2 \pm 9.9$	-	-
Total (unconstrained)	9870 ± 690	612 ± 17	22.3 ± 2.5
Total (constrained)	9730 ± 98	608.8 ± 3.8	21.80 ± 0.46
Data	9728	619	25
G^* Signal	$1097 \pm 17 \pm 63$	$14.27 \pm 0.19 \pm 0.76$	$0.0995 \pm 0.0013 \pm 0.0059$
W' Signal	$1950 \pm 40 \pm 140$	$145.0 \pm 2.3 \pm 8.1$	$3.64 \pm 0.06 \pm 0.31$

Table 6.1: Event yields in signal regions for data, expected backgrounds, and G^* and W' signals. The statistical and systematic uncertainties are given separately (in this order), except for the total background where the combined statistical and systematic uncertainty including correlations and constraints from data driven estimates is given. The signal points correspond to 500, 800, 1400 GeV.

6.2 Constraining New Physics

Given that there is no significant deviation from the Standard Model background expectation, the results can be interpreted as a constraint on the presence of new physics. In particular, the quantity that is constrained using this measurement is the production cross section times branching fraction for the production and decay of the new particle (i.e. G^*or W') and its subsequent decay to a ZZ or ZW pair at a particular mass and coupling (i.e. $\sigma(pp \to X) \times B(X \to ZZ/ZW)$). The final branching fraction of $B(Z \to \ell\ell)$ and $B(W/Z \to q\bar{q})$ is not included so as to allow the sensitivity of this search to be compared to the other diboson searches involving different final states.

At the LHC, these constraints are derived using the "profile likelihood method", which is beneficial in that it uses the data itself to constrain systematic uncertainties through simultaneously measuring the best fit values for these systematic uncertainties. However, understanding the method in which this calculation is performed benefits from first understanding the more basic CL_s test statistic.

6.2.1 The CL_s Method

The optimal method to distinguish this signal above the standard model background is to transform the full information contained within the signal region (i.e. six invariant mass spectra of $M(\ell\ell jj)$ and $M(\ell\ell J)$) into a single discriminating variable called the likelihood ratio test statistic, as shown in Equation 6.1. In this equation, $\mathbf{x}$ represents the data, b is the estimated background yield, s is the predicted signal yield, and $\mathcal{L}$ is the likelihood function, which for this application is a Poisson probability distribution function.

$$\Lambda(\mathbf{x}) = \frac{\mathcal{L}(s+b|\mathbf{x})}{\mathcal{L}(b|\mathbf{x})} \tag{6.1}$$

$$\mathcal{L}(s+b|\mathbf{x}) = \frac{(s+b)^{\mathbf{x}} e^{-(s+b)}}{\mathbf{x}!} \tag{6.2}$$

$$\mathcal{L}(b|\mathbf{x}) = \frac{(b)^{\mathbf{x}} e^{-(b)}}{\mathbf{x}!} \tag{6.3}$$

A combination of two or more orthogonal analysis channels is accommodated in this approach, because it is defined as the product of individual likelihoods for each channel. Furthermore, it is possible to take into account the full shape information of the given invariant mass spectrum by taking the full likelihood to be the product of the likelihood in each bin; $\mathcal{L} = \prod_i \mathcal{L}_i$.

$$\mathcal{L}(s+b|\mathbf{x}) = \prod_i^{\text{channels}} \prod_j^{\text{bins}} \frac{(s_{ij}+b_{ij})^{\mathbf{x}_{ij}} e^{-(s_{ij}+b_{ij})}}{\mathbf{x}_{ij}!} \tag{6.4}$$

$$\mathcal{L}(b|\mathbf{x}) = \prod_i^{\text{channels}} \prod_j^{\text{bins}} \frac{(b_{ij})^{\mathbf{x}_{ij}} e^{-(b_{ij})}}{\mathbf{x}_{ij}!} \tag{6.5}$$

By convention, the test statistic commonly reported is negative two times the logarithm of the likelihood ratio (LLR). This test statistic is evaluated for many sets of pseudo-experiments, to determine the frequency of the LLR value for the measured data ($P(s+b|x)$ and $P(b|x)$). In each experiment the data is sampled from a Poisson distribution whose argument is either the expected background yield or the sum of the signal and background for the background-only and signal+background hypotheses, respectively. Systematic uncertainties are introduced into the calculation by sampling the fractional uncertainty on each background or signal yield for each source of systematic uncertainty, as described in Section 6.2.1. A symmetric Gaussian distribution of the uncertainty is assumed unless asymmetric uncertainties are provided, as in the case of certain systematic uncertainties such as the jet energy scale uncertainty. Systematic uncertainties that are correlated between backgrounds and the signal are commonly sampled (e.g. luminosity) whereas uncorrelated systematic uncertainties (e.g. jet energy scale uncertainty in small-R versus large-R jets) are sampled independently. A distribution of the LLR for the signal+background and background-only hypothesis assumptions are constructed and confidence levels are defined by integrating the normalized probability distribution of LLR values from the observed LLR value to infinity as shown in Eqs. 6.6 and 6.7, respectively.

$$\mathrm{CL}_{s+b} = \int_{\mathrm{LLR}(s+b|\mathbf{x})}^{\infty} \mathbf{P}(s+b|x')d(\mathrm{LLR}(s+b|x')) \tag{6.6}$$

$$\mathrm{CL}_{b} = \int_{\mathrm{LLR}(b|\mathbf{x})}^{\infty} \mathbf{P}(b|x')d(\mathrm{LLR}(b|x')) \tag{6.7}$$

$$\mathrm{CL}_{s} = \frac{\mathrm{CL}_{s+b}}{\mathrm{CL}_{b}} \tag{6.8}$$

These two confidence intervals are combined to form the CL_s confidence interval, as in Eq. 6.8, by normalizing the result of the signal+background confidence level to that of the background only confidence level. This ensures that the presence of a signal is not rejected on account of a gross mismodelling of the background, which produces small values of both CL_{s+b} and CL_b. If an excess is observed in the data, the background-only hypothesis can be excluded at the 3σ and 5σ confidence level when 1-CL_b equals $1-2.7\times10^{-3}$ and $1-4.3\times10^{-7}$, respectively. In the case that data excess is not observed, the signal strength is excluded at 95% confidence level when 1-$\mathrm{CL}_s = 0.95$ and for all values in excess of this value of s.

Unfortunately, due to the presence of the systematic uncertainties described in Section 5.6, the sensitivity to the presence of new physics will degrade with respect to that shown in Figure 6.2. These systematic uncertainties on the signal and background are accounted for in the likelihood function using nuisance parameters. Nuisance parameters are extra degrees of freedom that, unlike the amount of the new physics signal s, are not of immediate interest. For each systematic uncertainty, the uncertainty is parameterized by two pieces, one for the uncertainty on the normalization and one for the uncertainty on the shape.

The normalization of the signal or background component k is given by $N_k = \prod \eta_{jk}$, where the product is over all of the systematics affecting component k. The η_{jk} are normalization scale factors, which are parametrized in terms of nuisance parameters α_{jk}^N as follows:

$$\begin{aligned} \eta_{jk} \;\equiv\;& (1+\sigma_{jk})^{\alpha_{jk}},\ \alpha \geq 0\,, \\ & (1-\sigma_{jk})^{-\alpha_{jk}},\ \alpha < 0\,, \end{aligned} \tag{6.9}$$

where σ_{jk} is the uncertainty on component k due to systematic j, and α_{jk}^N is a nuisance parameter with a Gaussian constraint of mean 0 and width 1. The parametrization ensures that the scale factor η_{jk} is positive. For small values of α, $\eta \approx (1+\alpha\sigma)$.

The shape systematics are provided by a second set of nuisance parameters. These are produced assuming a positive and negative 1σ variation in a given component of the systematic uncertainty, I^+ and I^-, which are used to determine an interpolation as in Equation 6.13, from the nominal estimate of the background to the systematic variation for

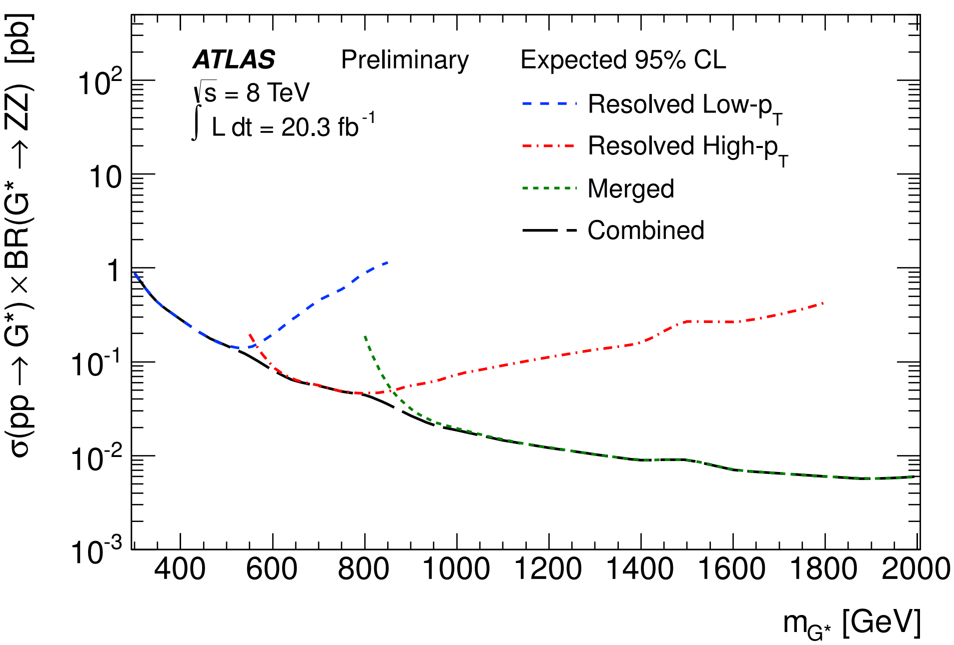

Figure 6.2: The expected limit with statistical uncertainties only for the three separate signal regions and for the combination of all selection regions.

each separate systematic.

$$I_{poly|exp}(\alpha_k^S) = \begin{cases} (I^+/I_0)^{\alpha_k^S} & \text{if } \alpha_k^S \geq 1 \\ 1 + \Sigma_{i=1}^{6} a_i \alpha_k^{Si} & \text{if } |\alpha_k^S| < 1 \\ (I^+/I_0)^{\alpha_k^S} & \text{if } \alpha_k^S \leq -1 \end{cases} \tag{6.10}$$

The extent to which this is varied is controlled by a set of nuisance parameters α_k^S, which are constrained by a Gaussian of mean 0 and width 1. The effect on the shape of the spectrum $\eta_{jk}(\alpha^S)$ for a given bin j in a signal or background template k is calculated bin-by-bin as a multiplication of the effect of the effect from all nuisance parameters as:

$$\eta_{jk} = \prod_{k}^{\text{syst}} I_{poly|exp}(\alpha_{jk}^S) \tag{6.11}$$

Lastly, because the background and signal estimations are ultimately derived from histograms with finite statistics, nuisance parameters are introduced to account for the bin-by-bin statistical uncertainties on each histogram [77].

6.2.2 The Profile Likelihood Method

This method can now be used to better understand the full profile likelihood method, the implementation of which differs slightly depending on whether one is testing for the presence of a new signal (discovery) or constraining the presence of that new signal (limits). In the case of testing for discovery, instead of using the basic likelihood ratio shown in Equation 6.1, the likelihood ratio is now formed by performing two binned maximum likelihood fits, one in which the signal strength is allowed to float, and one in which the signal strength is fixed to some value, in this case zero [78]. The likelihood ratio is then computed

$$\lambda(\mu) = \frac{\mathcal{L}(\mu, \hat{\hat{\theta}})}{\mathcal{L}(\hat{\mu}, \hat{\theta})}, \tag{6.12}$$

where μ is the signal strength, $\hat{\hat{\theta}}$ is a vector of the nuisance parameter values that maximize the likelihood $\mathcal{L}$ for the specified μ, and $\hat{\mu}$ and $\hat{\theta}$ are the signal strength and nuisance parameter values that maximize $\mathcal{L}$. These parameters are direct analogs of the signal strength

s and nuisance parameters α in the previous description of the CL_s method. It is these maximum likelihood fits that leverage the data to constrain systematic uncertainties if the data being fit have sufficient statistics. If this is the case, then the best fit value found in the construction of the likelihood will have an associated uncertainty on any given nuisance parameter that will not cause the fit to deviate significantly from the statistical uncertainty of that data being fit. This is used to calculate the test statistic

$$q(0) = \begin{cases} -2\ln\lambda(0) & \text{if } \hat{\mu} \geq 0, \\ 0 & \text{if } \hat{\mu} < 0, \end{cases} \tag{6.13}$$

Furthermore, this test statistic can be understood as a modification of the previous CL_s statistic in that the denominator against which the signal+background hypothesis is normalized is taken here to be the best description of the data, even in the presence of positive signal, and if the best fit signal strength is found to be negative, it is artificially made to be 0. A distribution of this likelihood can be built for the background only hypothesis (i.e. background estimation) and for each signal mass point. The p-value[1] of the data can be calculated to determine the extent to which the observed data deviate from the standard model prediction. This constitutes the search phase of the analysis, in which the local p-value is calculated, the results of which are shown in Figure 6.3. This demonstrates that the largest deviation from the background hypothesis has a local significance of at most approximately one sigma[2], which does not constitute any evidence for new physics.

Because the background only hypothesis describes the data sufficiently well, the results are interpreted as a constraint on the presence of new physics. A second set of maximum likelihood fits is thus performed, again one in which the signal strength is allowed to float, and one in which the signal strength is fixed to zero. The likelihood ratio is

$$\tilde{\lambda}(\mu) = \begin{cases} \frac{L(\mu,\hat{\hat{\theta}})}{L(0,\hat{\hat{\theta}})} & \text{if } \hat{\mu} < 0, \\ \frac{L(\mu,\hat{\hat{\theta}})}{L(\hat{\mu},\hat{\theta})} & \text{if } 0 \leq \hat{\mu}, \end{cases} \tag{6.14}$$

1. The p-value quantifies the probability that a new set of data would deviate from the expected background to an equal or greater extent than the current dataset assuming only Standard Model sources.

2. Quantifying the local significance in this way is standard nomenclature for the high energy physics community and is found by interpreting the p-value as the integration under the tail of a Gaussian curve. The location at which this integration starts is the corresponding number of sigmas of deviation.

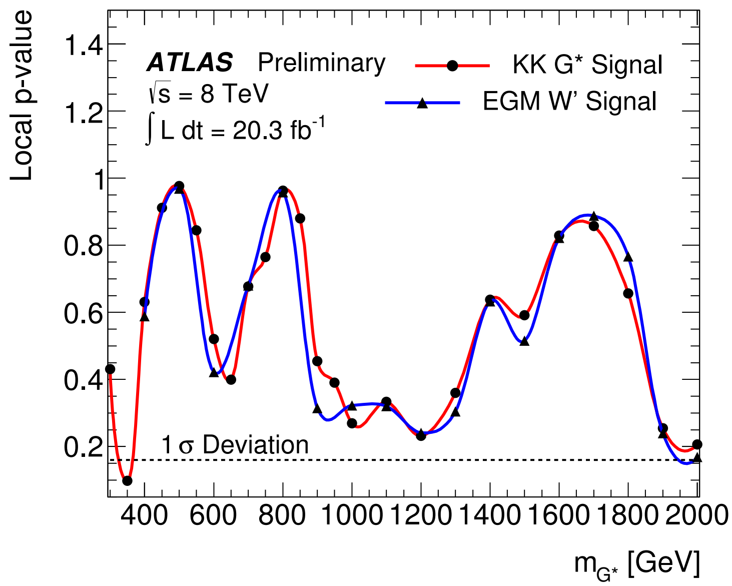

Figure 6.3: The local p-value calculated for the comparison of the data to background estimation by statistically combining all signal regions shown in Figure 6.1 using the method described in Section 6.2.2.

As before, this benefits by performing the multiple maximum likelihood fits to constrain systematic uncertainties where possible and is analogous to the normalized CL_s test statistic in the case that the best fit signal strength is negative. This is then used to calculate an analogous test statistic as before, where $\tilde{q}(\mu)$ is given by

$$\tilde{q}(\mu) = \begin{cases} -2\ln\tilde{\lambda}(\mu) & \text{if } \hat{\mu} \leq \mu, \\ 0 & \text{if } \hat{\mu} > \mu. \end{cases} \tag{6.15}$$

This test statistic, already normalized to the "background only" case, is integrated until 95%, at which point the signal strength μ (previously s) is taken as the upper limit on the signal strength. When the value of μ is then scaled by the initial cross section times branching ratio of the signal used, a limit is obtained on the physical quantity of interest. This calculation is performed for all signal mass points, using information from all signal regions. Shown in Figure 6.2 is the expected upper limit on $\sigma(pp \to G^*) \times B(G^* \to ZZ)$ when taking into account separately the three signal regions selected as described in Section 5.4, and the electron and muon channels. As expected, it is clear that the three selection regions contribute sensitivity to the signal in different mass regimes, with the merged regime dominating the

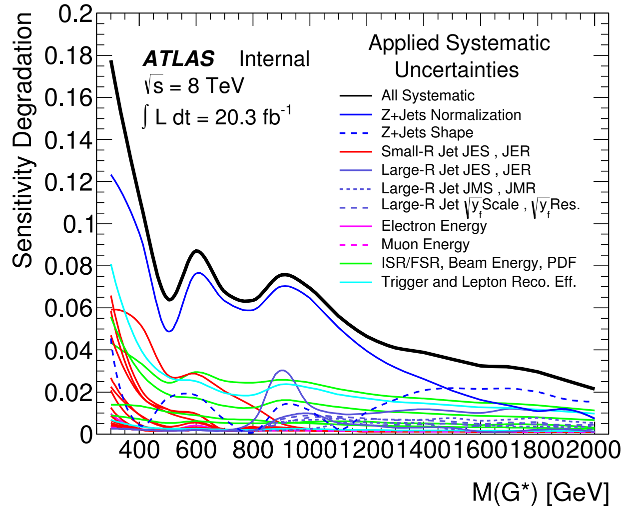

Figure 6.4: The fractional deviation from unity in comparing the expected upper limit on $\sigma(pp \to G^*) \times B(G^* \to ZZ)$ with and without the inclusion of systematic uncertainties as described in Section 6.2.1. For certain subdominant systematic uncertainties, multiple lines are shown, each which represent a separate uncorrelated uncertainty falling under that category.

sensitivity above 1 TeV.

The effect of the inclusion of systematic uncertainties into the final calculation of sensitivity, as described in Section 6.2.1, is apparent when deriving the limit on cross section times branching ratio in a way to isolate the effect of the systematic uncertainty in question. To do this, the sensitivity is first derived incorporating all systematic uncertainties (σ_{full}) and incorporating all systematics except the one in question ($\sigma_{full-syst}$). The quadrature difference between these two , $\sqrt{\sigma^2_{full} - \sigma^2_{full-syst}}$, is then taken as the effect on the sensitivity due to the inclusion of the given systematic uncertainty in the limit[3]. The results of this calculation are shown in Figure 6.4 for all of the systematic uncertainties considered in this search with a more explicit breakdown of these systematic uncertainties and the extent to which they affect the overall signal and background estimation in Appendix A. However, it is evident that the sensitivity is degraded by between 18% and 2% depending on the signal pole mass primarily due to the dominant uncertainty on the Z+jets background modelling, derived from the control region constraints.

3. Although other possibly ways to evaluate the effect of single systematic uncertainties exist, this is the conventionally recommended way to present the effect of single systematic uncertainties on sensitivity calculations in ATLAS.

6.2.3 The Full Constraints

The constraints derived from this analysis are interpreted in terms of two benchmark models as shown in Figure 6.5. The upper limits on $\sigma(pp \to G^*) \times B(G^* \to ZZ)$ range from approximately 1 pb at low mass to 200 pb at high mass. The upper limits on $\sigma(pp \to W') \times B(W' \to WZ)$ are similar with numerical values shown in Appendix B. However, due to the much larger production cross section of the W' as compared to the graviton, the mass limits that are obtained are quite different. In the case of the graviton signal, assuming $\kappa/\tilde{M}_{\mathrm{Pl}} = 1$, the observed (expected) mass limit is 740 (700) GeV and for the W', assuming a coupling of $c = 1$, the observed (expected) mass limit is 1590 (1540) GeV. These constraints extend those found by the experiments at the Tevatron, and are similar to those found by the CMS collaboration, as previously described in Section 2.2.3.

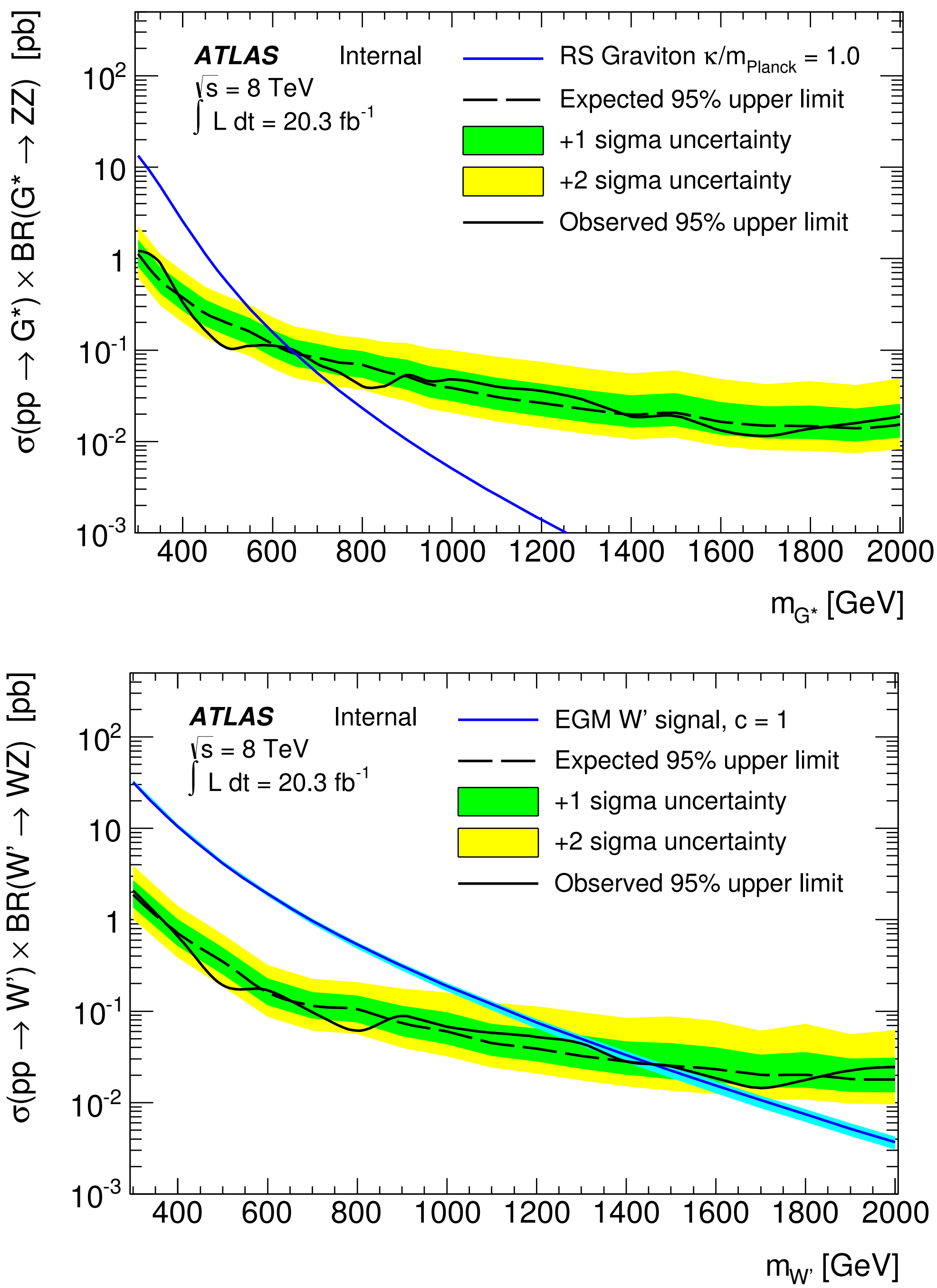

Figure 6.5: Observed and expected 95% CL upper limits on the cross section times branching fraction as a function of the resonance pole mass for (a) the bulk Randall-Sundrum graviton and (b) extended gauge model W'. The LO (NNLO) theoretical cross sections for the bulk Randall-Sundrum graviton (extended gauge model W') production are also shown. The band around the NNLO W' cross section represents the theoretical uncertainty on the NNLO calculation.

Chapter 7

Conclusions

This thesis presented a search for physics beyond the Standard Model in proton proton collisions at a center of mass energy of $\sqrt{s} = 8$ TeV using 20.3 fb^{-1} of data collected by the ATLAS detector. Guided by the philosophy of signature based searches, it focused on the $\ell\ell q\bar{q}$ final state originating from the resonant production of ZZ or ZW pairs of massive W and Z gauge bosons. To more effectively probe mass regimes greater than 1 TeV, in which there is a boosted hadronic $W/Z \rightarrow q\bar{q}$ decay, new techniques were applied that allow for the identification of merged boson jets through the understanding of jet substructure. When applied to this search, the improvement in sensitivity obtained is dramatic. No deviation from the Standard Model expectation is observed, and constraints are placed on the cross section times branching fraction of two benchmark models, the bulk Randall-Sundrum graviton and the extended gauge model W'.

These constraints, along with those from a wealth of other new physics signatures, can be translated into constraints on the mass scale allowed for generic benchmark models as shown in Figure 7.1. All such constraints are beginning to probe the TeV scale and beyond, widely believed to be the scale at which new physics must exist. Therefore, as the four experiments prepare to collect data in Run 2 of the LHC at an increased center of mass energy, it is essential to continue to advance the understanding of the experimental apparatus and the manner in which the data collected can be used to best search beyond the Standard Model and continue to work to expand the reach of the light on the lamp post.

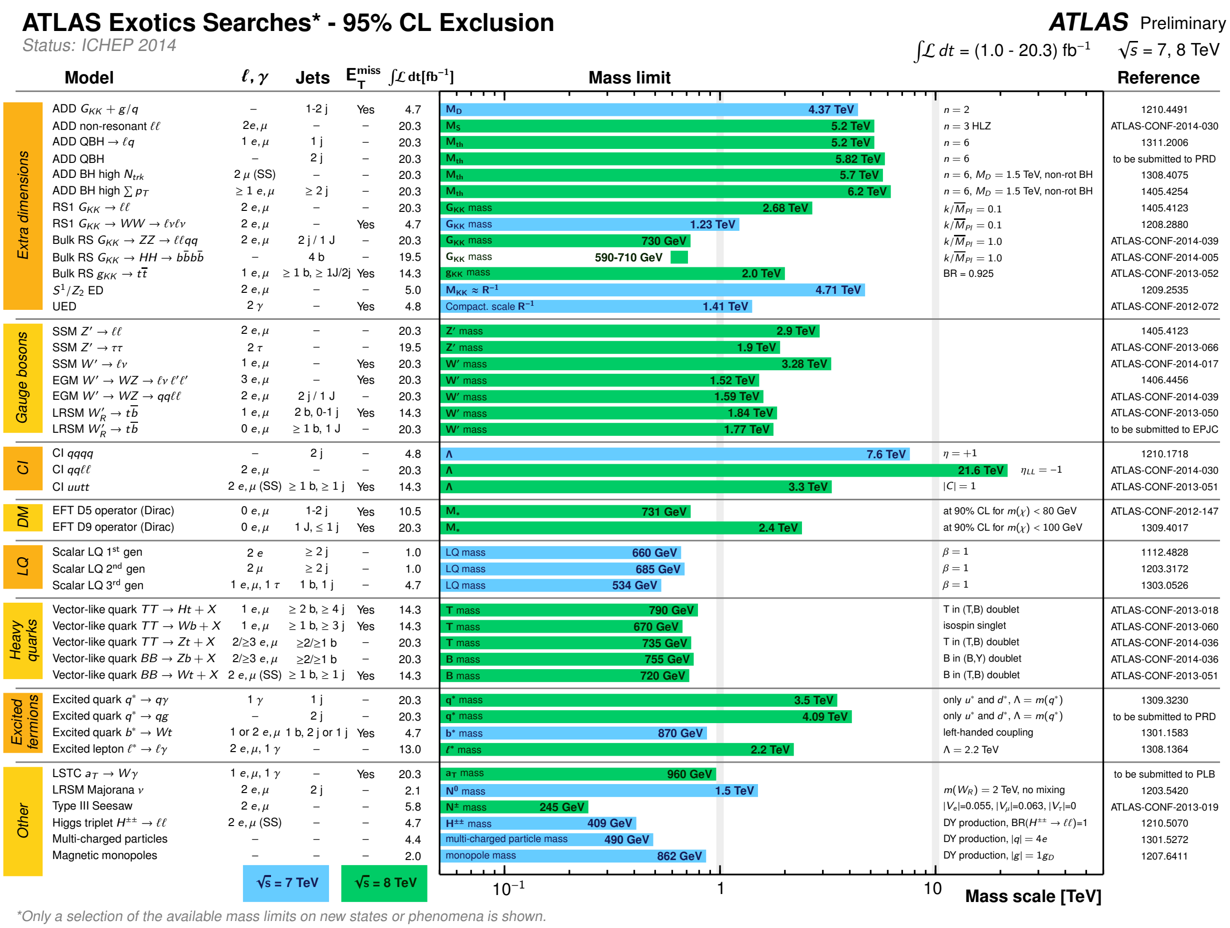

Figure 7.1: Summary of mass constraints placed on a number of searches for beyond the Standard Model physics performed at ATLAS.

Appendix A
Uncertainties in Fit

The uncertainties taken into account by nuisance parameters in the fit are listed in Table A.1, A.2, and, A.3. The dominant uncertainties on the background estimation comes from the correction of the Z+jets background correction, primarily because it is the dominant background. In order to simplify the fit and make the computation more efficient, all other systematic uncertainties deemed to be negligible are removed. To determine if an uncertainty is significant two tests are performed. First, the overall normalization of the nominal and systematically shifted spectra are compared and if the integrals are different by greater than 0.5σ of the statistical uncertainty, then an uncertainty on normalization is considered for that sample. For the shape, a Kolmogorov-Smirnov test is performed between the nominal and systematically shifted sample. If any background sample in a signal region returns a value of less than 0.1 then the systematic uncertainty is considered as a shape uncertainty for all backgrounds in that region. Systematic shape uncertainties are considered in the same way on signal samples, however each sample is considered individually. The results of these two, indicating the size of the systematic uncertainty in normalization and shape for the various background components and a G^* sample representative of the given signal region, are shown in Figures A.1, A.2, and A.3. It should be noted here that the background components evaluated here show separately the three $Z + jets$ components for bottom, charm, and light flavor jets referred to as $Z + B$, $Z + C$, and $Z + L$, respectively. Finally, shown in Tables A.1 through A.3 is a full summary of which systematic uncertainties have been included on *at least* one component in the fit based on the aforementioned prescription.

The effect of these individual systematic components is shown in Figure A.4. The effect of the inclusion of systematic uncertainties into the final calculation of sensitivity is apparent when deriving the limit on cross section times branching ratio in a way to isolate the effect of the systematic uncertainty in question. To do this, the sensitivity is first derived incorporating all systematic uncertainties (σ_{full}) and incorporating all systematics except that in question ($\sigma_{full-syst}$). The quadrature difference between these two , $\sqrt{\sigma^2_{full} - \sigma^2_{full-syst}}$, is then taken as the effect on the sensitivity due to the inclusion of the given systematic uncertainty in the limit. This calculation is shown in Figure 6.4 for all systematic uncertainties divided into five main categories based on their source.

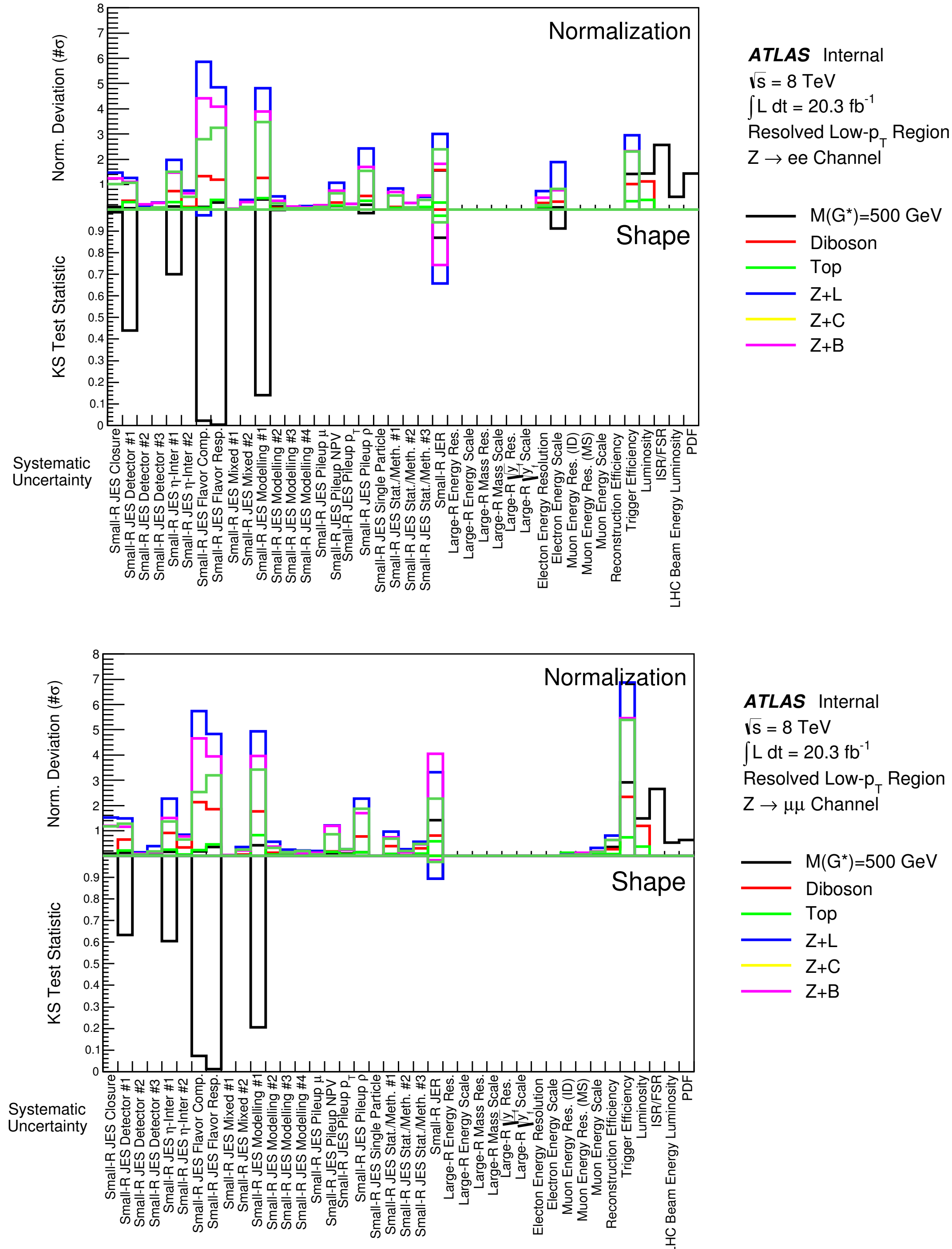

Figure A.1: Summary of the deviation from the nominal signal and background component estimates, in terms of the normalization and Kolmogorov-Smirnov (KS) test statistic for shape comparison, for all systematic uncertainties considered in the low-p_T resolved signal region in the electron channel (top) and muon channel (bottom).

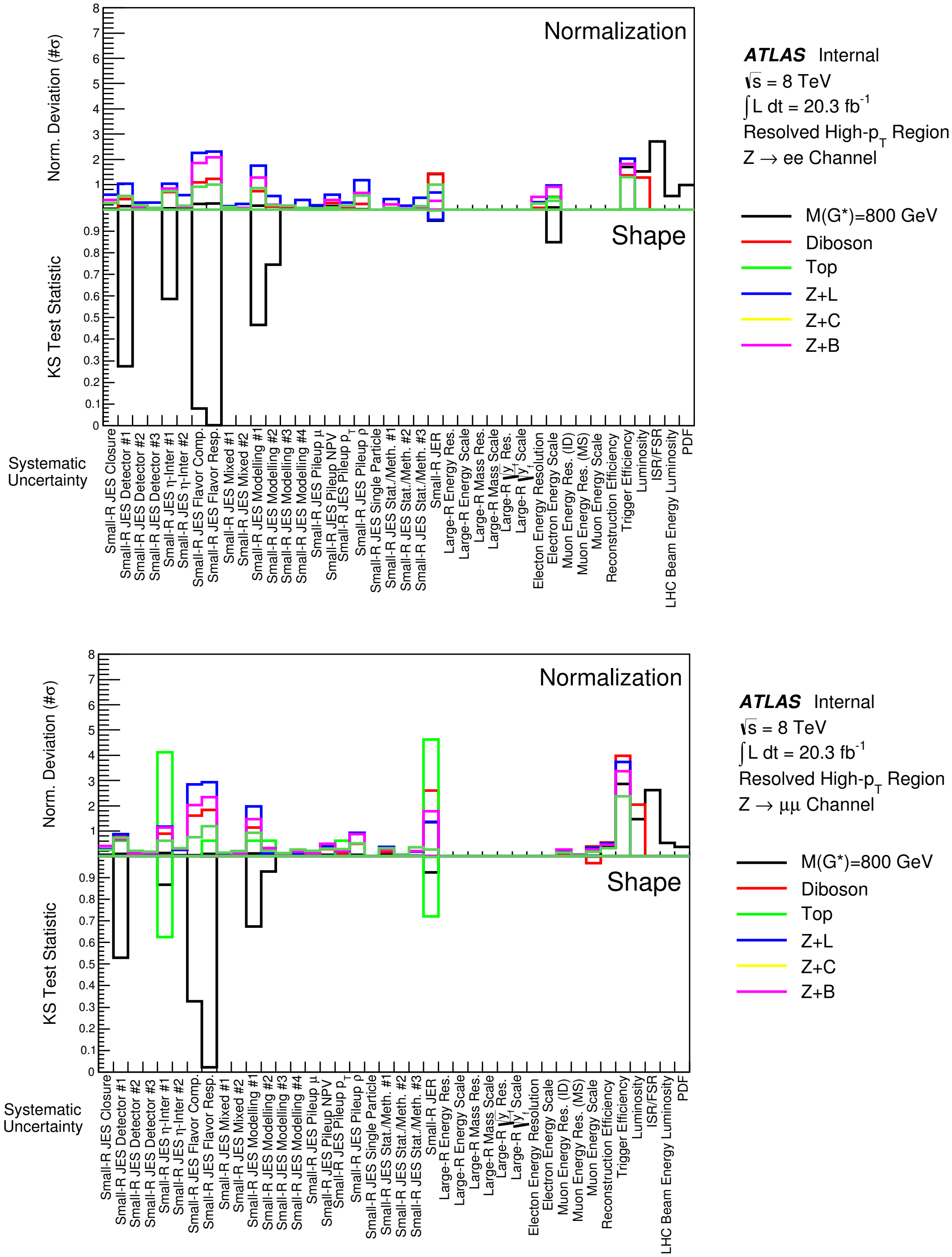

Figure A.2: Summary of the deviation from the nominal signal and background component estimates, in terms of the normalization and Kolmogorov-Smirnov (KS) test statistic for shape comparison, for all systematic uncertainties considered in the high-p_T resolved signal region in the electron channel (top) and muon channel (bottom).

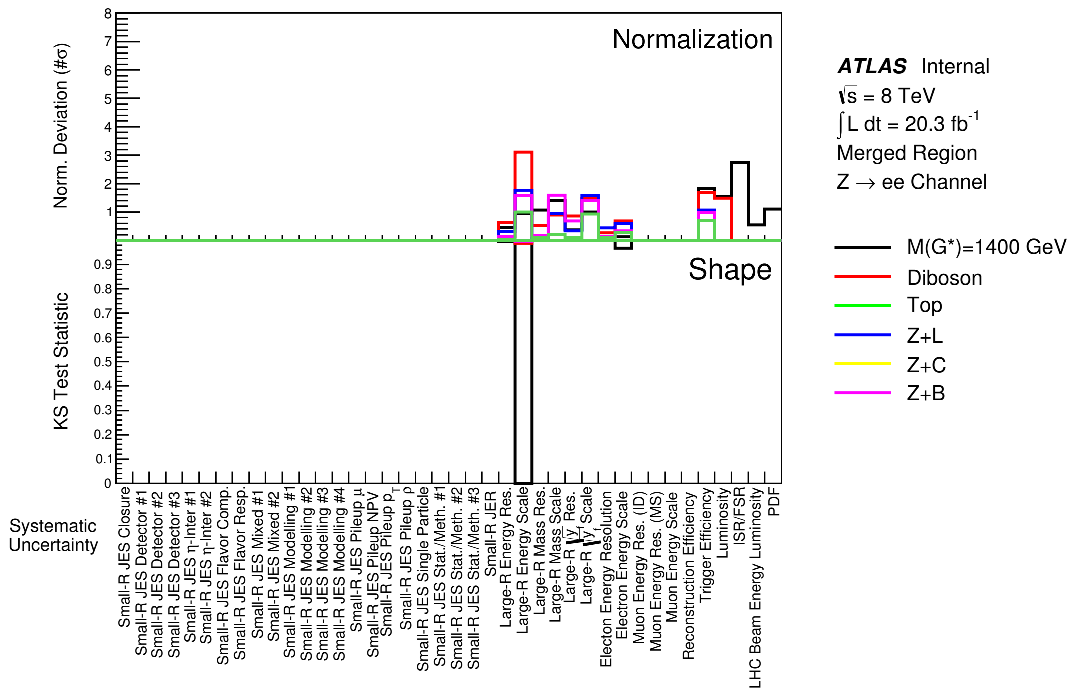

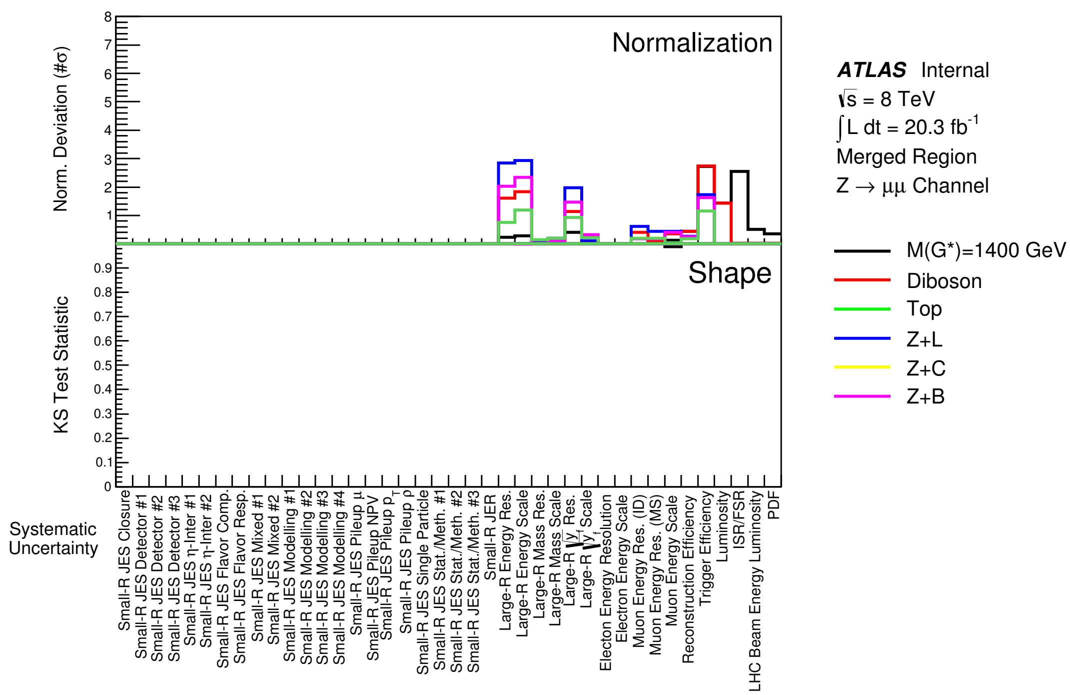

Figure A.3: Summary of the deviation from the nominal signal and background component estimates, in terms of the normalization and Kolmogorov-Smirnov (KS) test statistic for shape comparison, for all systematic uncertainties considered in the merged signal region in the electron channel (top) and muon channel (bottom).

Source of Systematic	Electron			Muon		
	Res. Low	Res. High	Merged	Res. Low	Res. High	Merged
JES Closure	N	N		N		
JES Detector #1	N	S		N	N S	
JES Detector #2	N					
JES Detector #3	N			N		
JES η-Inter #1	N	N		N	N	
JES η-Inter #2	N			N		
JES Flavor Comp.	N S	N S		N S	N S	
JES Flavor Resp.	N S	N S		N S	N S	
JES Mixed #1	N					
JES Mixed #2	N			N		
JES Modeling #1	N S	N		N S	N	
JES Modeling #2	N			N		
JES Modeling #3	N					
JES Modeling #4	N			N		
JES Pileup μ	N			N		
JES Pileup NPV	N	N		N		
JES Pileup p_T	N			N		
JES Pileup Rho	N	N		N	N	
JES Stat./Meth. #1	N			N		
JES Stat./Meth. #2	N					
JES Stat./Meth. #3	N			N		
JER	N			N		

Table A.1: For the small-R jet reconstruction uncertainties, the nuisance parameters used in template fit to incorporate systematic uncertainties. For each nuisance parameter and signal region, the entry indicates whether the nuisance parameter incorporates a normalization, "N", uncertainty and/or a shape, "S", uncertainty into the fit, based on the tests descried in A.

Source of Systematic	Electron			Muon		
	Res. Low	Res. High	Merged	Res. Low	Res. High	Merged
Energy Res.			N S			N S
Energy Scale			N S			N S
Mass Res.			N			N
Mass Scale			N			N
$\sqrt{y_f}$ Res.			N			N
$\sqrt{y_f}$ Scale			N			N

Table A.2: For the large-R jet reconstruction uncertainties, the nuisance parameters used in template fit to incorporate systematic uncertainties. For each nuisance parameter and signal region, the entry indicates whether the nuisance parameter incorporates a normalization, “N”, uncertainty and/or a shape, “S”, uncertainty into the fit, based on the tests descried in A.

Source of Systematic	Electron			Muon		
	Res. Low	Res. High	Merged	Res. Low	Res. High	Merged
Electron Energy Res.	N		N			
Electron Energy Scale	N	N	N			
ISR/FSR	N	N	N	N	N	N
LHC Beam Energy	N	N	N	N	N	N
Luminosity	N	N	N	N	N	N
Muon Energy Res. (ID)				N		N
Muon Energy Res. (MS)						
Muon Energy Scale				N	N	N
PDF	N	N	N	N	N	N
Reco. Efficiency				N	N	N
Trigger Efficiency	N	N	N	N	N	N
$Z + jets$ BG Norm.	N	N	N	N	N	N
$Z + jets$ BG Slope	S	S	S	S	S	S

Table A.3: For all uncertainties not related to jet reconstruction uncertainties, the nuisance parameters used in template fit to incorporate systematic uncertainties. For each nuisance parameter and signal region, the entry indicates whether the nuisance parameter incorporates a normalization, "N", uncertainty and/or a shape, "S", uncertainty into the fit, based on the tests descried in A.

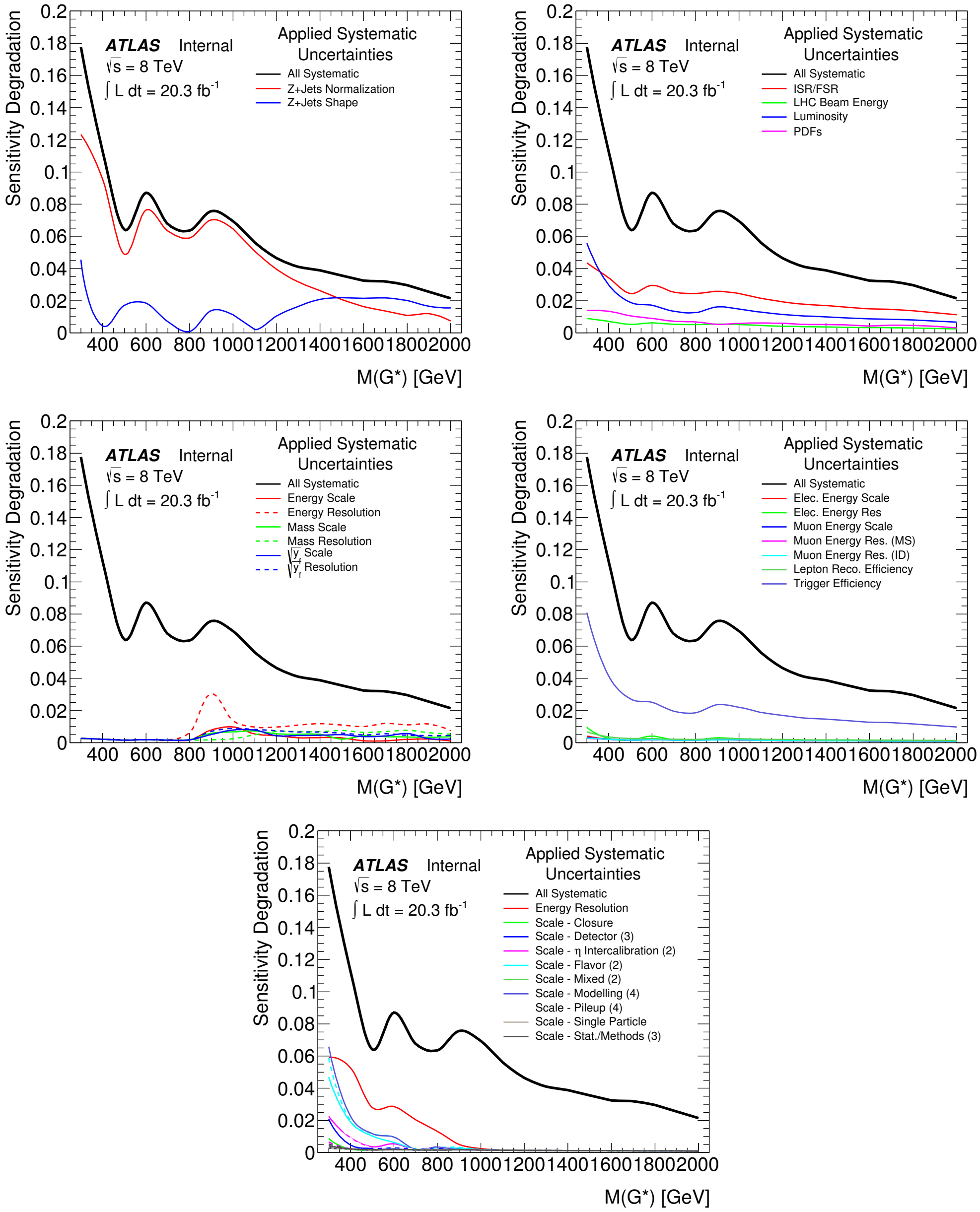

Figure A.4: The fractional deviation from unity in comparing the expected upper limit on $\sigma(pp \to G^*) \times B(G^* \to ZZ)$ with and without the inclusion of systematic uncertainties. The affect on the sensitivity due to each component is calculated as the quadrature difference between the sensitivity derived incorporating all systematic uncertainties (σ_{full}) and incorporating all systematics except that in question $(\sigma_{full-syst})$, $\sqrt{\sigma^2_{full} - \sigma^2_{full-syst}}$.

Appendix B
Tabulated Numerical Results

Presented here are the numerical results for the total event counts for the three signal regions, summarized in Section 6.1, but presented in greater detail in more exclusive signal regions and with additional signal points in Tables B.1 B.2 B.3. In addition, shown in Tables B.4 and B.5 constraints on production cross section times branching for the two benchmark models considered in this search, presented graphically in Figure 6.5.

Signal region	Low-p_{T} Resolved	
Channel	Electron	Muon
Z+jets	$4358 \pm 27 \pm 20$	$5102 \pm 29 \pm 21$
Diboson	$108.2 \pm 2.7 \pm 9.2$	$125 \pm 3 \pm 13$
Top	$87.6 \pm 6.4 \pm 5.1$	$87.7 \pm 6.5 \pm 4.8$
ΣBackgrounds	$4553 \pm 28 \pm 33$	$5315 \pm 30 \pm 37$
After Profiling	4547 ± 22	5305 ± 20
Data	4440	5288
$G^*(M = 0.5$ TeV)	$554 \pm 12 \pm 41$	$543 \pm 12 \pm 47$
$G^*(M = 0.8$ TeV)	$0.514 \pm 0.03 \pm 0.11$	$0.62 \pm 0.039 \pm 0.12$
$G^*(M = 1.4$ TeV)	$0.00027 \pm 0.00007 \pm 0.00041$	$0.00027 \pm 0.00007 \pm 0.00042$
W'($M = 0.5$ TeV)	$911 \pm 26 \pm 86$	$1040 \pm 27 \pm 110$
W'($M = 0.8$ TeV)	$9.2 \pm 0.6 \pm 1.2$	$9.4 \pm 0.6 \pm 1.2$
W'($M = 1.4$ TeV)	$0.0710 \pm 0.0087 \pm 0.0094$	$0.00033 \pm 0.00008 \pm 0.00051$

Table B.1: Estimated background yields, the observed number of data events, and the predicted signal yields for the low p_{T} resolved region. Where two uncertainties are shown these are statistical and systematic. For the profiled backgrounds the uncertainty combines statistical and systematic.

Signal region	High-p_{T} Resolved	
Channel	Electron	Muon
Z+jets	$291.8 \pm 3.0 \pm 4.8$	$298.8 \pm 3.0 \pm 4.7$
Diboson	$10.19 \pm 0.22 \pm 0.65$	$10.37 \pm 0.14 \pm 0.80$
Top	-	-
ΣBackgrounds	$302.4 \pm 3.0 \pm 7.4$	$309.2 \pm 3.0 \pm 7.3$
After Profiling	300.8 ± 4.5	307.9 ± 4.1
Data	307	312
$G^{*}(M = 0.5$ TeV)	$6.3 \pm 1.3 \pm 1.3$	$7.5 \pm 1.4 \pm 1.5$
$G^{*}(M = 0.8$ TeV)	$7.42 \pm 0.14 \pm 0.52$	$6.86 \pm 0.13 \pm 0.56$
$G^{*}(M = 1.4$ TeV)	$0.00360 \pm 0.00025 \pm 0.00032$	$0.00258 \pm 0.00021 \pm 0.00024$
W'($M = 0.5$ TeV)	$6.7 \pm 2.1 \pm 6.4$	$5.5 \pm 2.1 \pm 4.9$
W'($M = 0.8$ TeV)	$74.1 \pm 1.6 \pm 5.4$	$70.9 \pm 1.6 \pm 6.0$
W'($M = 1.4$ TeV)	$0.237 \pm 0.016 \pm 0.020$	$0.236 \pm 0.016 \pm 0.023$

Table B.2: Estimated background yields, the observed number of data events, and the predicted signal yields for the high p_{T} resolved signal region. Where two uncertainties are shown these are statistical and systematic. For the profiled backgrounds the uncertainty combines statistical and systematic.

Signal region	Merged	
Channel	Electron	Muon
Z+jets	$11.31 \pm 0.23 \pm 0.77$	$9.60 \pm 0.20 \pm 0.72$
Diboson	$0.723 \pm 0.014 \pm 0.063$	$0.660 \pm 0.013 \pm 0.064$
Top	-	-
ΣBackgrounds	$12.0 \pm 0.2 \pm 1.2$	$10.3 \pm 0.2 \pm 1.1$
After Profiling	11.80 ± 0.69	10.57 ± 0.68
Data	8	17
$G^*(M = 0.5$ TeV)	$2.2 \pm 0.7 \pm 1.8$	$1.05 \pm 0.50 \pm 0.94$
$G^*(M = 0.8$ TeV)	$0.53 \pm 0.04 \pm 0.12$	$0.432 \pm 0.033 \pm 0.092$
$G^*(M = 1.4$ TeV)	$0.056 \pm 0.0010 \pm 0.0046$	$0.043 \pm 0.0010 \pm 0.0038$
W'($M = 0.5$ TeV)	$0 \pm 0 \pm 0$	$0.053 \pm 0.053 \pm 0.005$
W'($M = 0.8$ TeV)	$2.54 \pm 0.30 \pm 0.70$	$2.76 \pm 0.32 \pm 0.78$
W'($M = 1.4$ TeV)	$2.00 \pm 0.05 \pm 0.23$	$1.63 \pm 0.04 \pm 0.21$

Table B.3: Estimated background yields, the observed number of data events, and the predicted signal yields for the merged region. Where two uncertainties are shown these are statistical and systematic. For the profiled backgrounds the uncertainty combines statistical and systematic.

M(G^*)	Cross Section (σ) Process $\times$ BR [fb]	-2σ [fb]	-1σ [fb]	Expected [fb]	+1σ [fb]	+2σ [fb]	Observed [fb]
300	1.3E+04	5.6E+02	7.5E+02	1.0E+03	1.5E+03	2.1E+03	1.1E+03
350	6.2E+03	2.7E+02	3.6E+02	4.9E+02	7.0E+02	9.8E+02	7.8E+02
400	2.6E+03	1.7E+02	2.3E+02	3.2E+02	4.5E+02	6.2E+02	2.8E+02
450	1.1E+03	1.1E+02	1.5E+02	2.1E+02	3.0E+02	4.1E+02	1.4E+02
500	5.4E+02	8.5E+01	1.1E+02	1.6E+02	2.2E+02	3.1E+02	8.5E+01
550	2.8E+02	6.7E+01	8.9E+01	1.2E+02	1.8E+02	2.4E+02	8.7E+01
600	1.6E+02	4.7E+01	6.4E+01	8.8E+01	1.3E+02	1.7E+02	8.5E+01
650	9.2E+01	3.6E+01	4.9E+01	6.8E+01	9.6E+01	1.3E+02	7.3E+01
700	5.6E+01	3.2E+01	4.3E+01	5.9E+01	8.4E+01	1.2E+02	5.1E+01
750	3.6E+01	2.7E+01	3.7E+01	5.1E+01	7.3E+01	1.0E+02	4.0E+01
800	2.3E+01	2.5E+01	3.4E+01	4.7E+01	6.7E+01	9.3E+01	2.7E+01
850	1.5E+01	2.0E+01	2.7E+01	3.8E+01	5.4E+01	7.7E+01	2.6E+01
900	1.0E+01	1.5E+01	2.1E+01	2.9E+01	4.2E+01	6.0E+01	3.0E+01
950	7.2E+00	1.2E+01	1.6E+01	2.3E+01	3.3E+01	4.7E+01	2.5E+01
1000	5.1E+00	1.1E+01	1.4E+01	2.0E+01	2.9E+01	4.2E+01	2.5E+01
1100	2.6E+00	8.3E+00	1.1E+01	1.5E+01	2.2E+01	3.3E+01	1.9E+01
1200	1.4E+00	6.8E+00	9.1E+00	1.3E+01	1.9E+01	2.7E+01	1.6E+01
1300	7.7E-01	5.8E+00	7.7E+00	1.1E+01	1.6E+01	2.3E+01	1.3E+01
1400	4.4E-01	5.0E+00	6.7E+00	9.3E+00	1.4E+01	2.1E+01	8.8E+00
1500	2.6E-01	5.0E+00	6.7E+00	9.3E+00	1.4E+01	2.1E+01	8.6E+00
1600	1.5E-01	3.9E+00	5.3E+00	7.3E+00	1.1E+01	1.7E+01	6.0E+00
1700	9.3E-02	3.6E+00	4.8E+00	6.7E+00	1.0E+01	1.6E+01	5.3E+00
1800	5.8E-02	3.3E+00	4.4E+00	6.2E+00	9.4E+00	1.5E+01	5.8E+00
1900	3.6E-02	3.1E+00	4.2E+00	5.8E+00	8.9E+00	1.4E+01	6.6E+00
2000	2.3E-02	3.3E+00	4.4E+00	6.1E+00	9.4E+00	1.5E+01	7.3E+00

Table B.4: Observed and expected limits on cross section times branching fraction for the bulk Randall-Sundrum $G^* \to ZZ$ signal.

M(W')	Cross Section (σ) Process $\times$ BR [fb]	-2σ [fb]	-1σ [fb]	Expected [fb]	+1σ [fb]	+2σ [fb]	Observed [fb]
400	1.0E+04	3.8E+02	5.1E+02	7.1E+02	1.0E+03	1.4E+03	6.6E+02
500	4.1E+03	1.9E+02	2.5E+02	3.5E+02	5.0E+02	6.9E+02	1.9E+02
600	1.9E+03	8.6E+01	1.2E+02	1.6E+02	2.3E+02	3.2E+02	1.7E+02
700	9.7E+02	6.2E+01	8.3E+01	1.1E+02	1.6E+02	2.3E+02	9.7E+01
800	5.4E+02	5.6E+01	7.6E+01	1.0E+02	1.5E+02	2.1E+02	6.1E+01
900	3.1E+02	3.2E+01	4.3E+01	6.0E+01	8.8E+01	1.3E+02	7.0E+01
1000	1.9E+02	2.4E+01	3.3E+01	4.6E+01	6.7E+01	9.8E+01	5.4E+01
1100	1.2E+02	2.0E+01	2.7E+01	3.7E+01	5.4E+01	8.0E+01	4.5E+01
1200	7.5E+01	1.7E+01	2.3E+01	3.2E+01	4.7E+01	7.0E+01	4.1E+01
1300	5.0E+01	1.4E+01	1.9E+01	2.7E+01	4.0E+01	6.1E+01	3.5E+01
1400	3.3E+01	1.3E+01	1.7E+01	2.4E+01	3.5E+01	5.4E+01	2.4E+01
1500	2.3E+01	1.1E+01	1.4E+01	2.0E+01	3.0E+01	4.6E+01	1.9E+01
1600	1.5E+01	1.0E+01	1.4E+01	1.9E+01	2.9E+01	4.6E+01	1.6E+01
1700	1.1E+01	9.8E+00	1.3E+01	1.8E+01	2.8E+01	4.5E+01	1.3E+01
1800	7.5E+00	8.8E+00	1.2E+01	1.6E+01	2.5E+01	4.0E+01	1.5E+01
1900	5.2E+00	9.0E+00	1.2E+01	1.7E+01	2.6E+01	4.2E+01	2.0E+01
2000	3.7E+00	8.4E+00	1.1E+01	1.6E+01	2.4E+01	3.9E+01	2.0E+01

Table B.5: Observed and expected limits on cross section times branching fraction for the extended gauge model $W' \to ZW$ signal.

Appendix C
Receiver Operator Characteristic (ROC) Curves

A common method to optimize a selection, or compare performance characteristics on a given variable to reject background in favor of signal is through the use of receiver operator characteristic (ROC) curves[1]. The general idea to produce a ROC curve is to scan a number of selection criteria and count the relative amount of selected and rejected events given each selection criteria. This scan produces a set of signal efficiency (ϵ_{sig}) and background rejection ($1 - \epsilon_{bg}$) values, one for each selection, that trace out a curve in the (ϵ_{sig}, $1 - \epsilon_{bg}$) space. However, two slightly different methods of doing this are implemented in this analysis.

The first method of defining a ROC curve, used in the optimization of boson tagging in Section 4.4, is rather general and can be generalized to higher dimensions of variables for more complex analyses. The general idea is to select the region of phase space, which may not necessarily be defined by a single rectangular cut, that produces the optimal ratio of signal to background. The procedure for a single selection variable is as follows

1. Given a binned signal distribution (S_i) and background distribution (B_i), order the bins based on the quantity $R_i = \frac{S_i}{B_i}$. Note that this ordering can be based on any figure of merit, R_i, if desired.

2. Define a selection criteria for some value of R_i and calculate ϵ_{sig} and $1 - \epsilon_{bg}$ for this selection.

3. Repeat 2 for a monotonically increasing set of selection criteria and define the ROC curve as the set of (ϵ_{sig}, $1 - \epsilon_{bg}$) points determined here.

There are two features of note concerning this procedure. The first is that it will produce ROC curves that monotonically select a region of phase space that has higher values of signal over background. Therefore, the ROC curve produced from two very different methods of dividing the phase space, meaning two different selection selection variables or sets of selection variables. However, this also means that a given selection on the variable R_i will

1. The concept of using ROC curves was initially developed by radar engineers during world war II to detect enemy objects in battlefields and test the methods they developed to perform this task.

not necessarily select a single region of phase space in the original set of variables, but may select different "pockets" of phase space depending on the form of the S_i and B_i distributions.

The second method of defining a ROC curve is very similar to previous method, but no transformation to the R_i variable is made. Instead, the monotonic cuts and subsequent calculation of the (ϵ_{sig},$1-\epsilon_{bg}$) set of points is made directly on the phase space, in this case a single variable, used to classify events. This creates ROC curves that have structure based on the details of the signal and background spectra which is beneficial from the standpoint that is allows for the definition of a single selection criteria that can directly be implemented as a single selection criteria in a search. For the search in this thesis, the specific selection value is defined as the selection criteria that produces the ROC curve point located closest to the optimal $\epsilon_{sig} - 1$ and $1 - \epsilon_{bg} = 1$ point, namely that minimizes $R = \sqrt{\epsilon_{sig}^2 + \epsilon_{sig}^2}$. This is the method used in Section 5.4 to determine the numerical values of selection criteria used in the analysis.

Appendix D
Signal Shape

In general, this search is sensitive to narrow resonances. However, the width of the excess that is expected on the reconstructed $M(\ell\ell+jet+jet)$ or $M(\ell\ell+FatJet)$ mass spectrum is a combination of the physical width of the resonance, which is typically on the order of a few percent times the pole mass of the signal being considered, and resolution effects coming from reconstruction of physics objects. To estimate the behavior of this width, the $G^*$and W' signals are reconstructed in the three signal regions for a subset of mass points targetted by that region. The resulting templates are fit with Gaussian PDFs and the fitted width is extracted. The resulting set of widths are fit with an exponential function as Shown in Figure D.1 for the G^*signal, which is representative of the shape of the expected excess and guides the binning used in this search, which is taken to be $BinWidth = 1.5e^{2.9+0.0011\times M_{reco}}$ GeV.

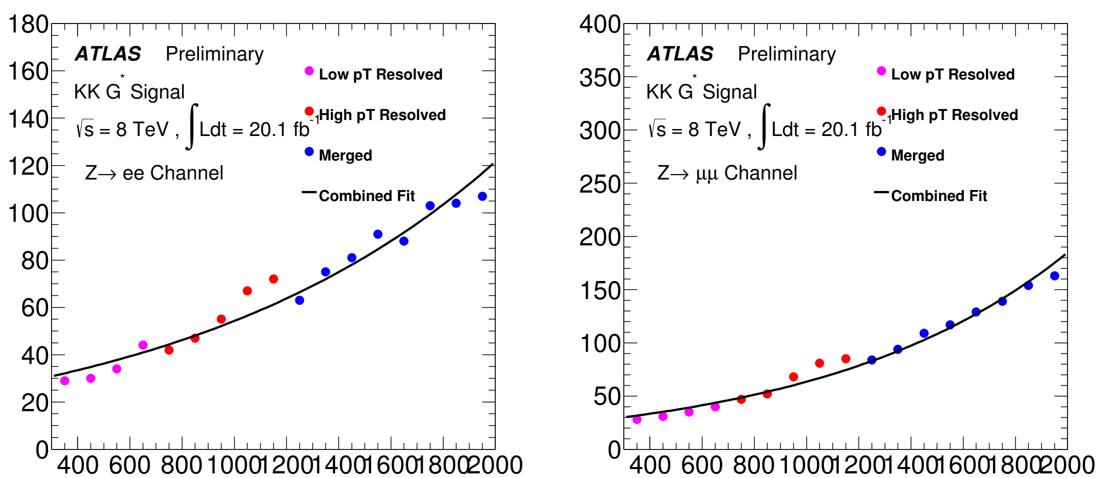

Figure D.1: Reconstructed mass resolution, the fitted Gaussian width of the $M(\ell\ell+jet+jet)$ and $M(\ell\ell+FatJet)$ mass spectra, as a function of the G^*mass for the electron (left) and muon (right) channels.

Appendix E
Final State Sensitivity Comparison

Due to the nature of different final states for diboson pairs, sensitivity to a new physics signal varies as a function of the mass scale of the particle for which the search is performed. In particular, the low mass region (< 1 TeV) is probed with greatest sensitivity using fully leptonic final states which have increased mass resolution. However, the lack of statistics at high mass ($>> 1$ TeV) in these channels necessitates the use of hadronic final states and therefore the fully hadronic final state, with the highest mass reach dominates in this region. However, in the overlap region near 1.5 TeV, the semileptonic final states combine these strengths to provide increased sensitivity in this region. This is demonstrated in Figure E.1 which shows the expected sensitivity for a number of final states for the Extended Gauge Model W'signal.

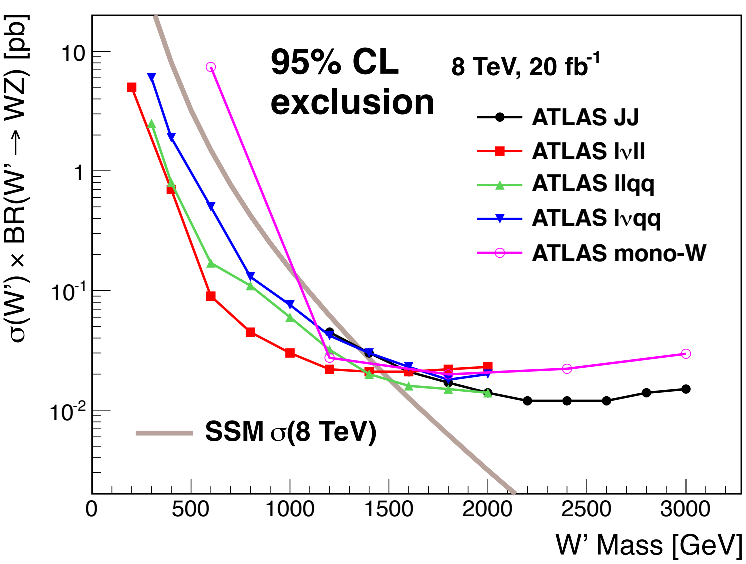

Figure E.1: Comparison of the sensitivity to the Extended Gauge Model W'signal in terms of production cross section times branching ratio to WZ for a number of final state channels.

References

[1] Matteo Cacciari, Gavin P. Salam, and Gregory Soyez. The anti-k_t jet clustering algorithm. *JHEP*, 04:063, 2008.

[2] ATLAS Collaboration. Performance of boosted w boson identification with the atlas detector. 2014.

[3] CERN. Ecfa-cern workshop on large hadron collider in the lep tunnel.

[4] ATLAS Collaboration. Observation of a new particle in the search for the standard model higgs boson with the atlas detector at the lhc. *Phys. Lett.*, B 716:1–29, 2012.

[5] CMS Collaboration. Observation of a new boson at a mass of 125 gev with the cms experiment at the lhc. *Phys. Lett.*, B 716:30–61, 2012.

[6] C. Burgess and G. Moore. *The Standard Model : A Primer*. Cambridge University Press, Cambridge, UK, 2007.

[7] M. Schwartz. *Quantum Field Theory and the Standard Model*. Cambridge University Press, Cambridge, UK, 2014.

[8] C. Quigg and R. Shrock. Gedanken worlds without higgs: Qcd-induced electroweak symmetry breaking. *Phys. Rev.*, D 79:096002, 2009.

[9] B. Cleveland et al. Measurement of the solar electron neutrino flux with the homestake chlorine detector. *Astrophysical Journal*, 496:505–526, 1998.

[10] V.C. Rubin et al. Extended rotation curves of high-luminosity spiral galaxies. iv - systematic dynamical properties, sa through sc. *Astrophysical Journal, Part 2 - Letters to the Editor*, 225:L107–L111, 1978.

[11] G. Paal et al. Inflation and compactification from galaxy redshifts? *Astrophysics and Space Science*, 191:107–124, 1991.

[12] H. Murayama. Supersymmetry. *Proceedings of the 22^{nd} International Symposium on Physics with High Energy Colliders*, page 476, 1995.

[13] A. De Ruula et al. Hadron masses in a gauge theory. *Phys. Rev.*, D 12:147–162, 1975.

[14] *Image courtesy of Hitoshi Murayama.*

[15] L. Randall and R. Sundrum. A large mass hierarchy from a small extra dimension. *Phys. Rev. Lett.*, 83:3370–3373, 1999.

[16] K. Agashe et al. Warped gravitons at the cern lhc and beyond. *Phys. Rev.*, D 76:036006, 2007.

[17] A. et. al Belyaev. Calchep - a package for calculation of feynman diagrams and integration over multi-particle phase space. *Comput. Phys. Commun.*, 184:1729, 2013.

[18] Pavel M. Nadolsky et al. Implications of cteq global analysis for collider observables. *Phys. Rev.*, D 78:013004, 2008.

[19] Torbjorn Sjostrand, Stephen Mrenna, and Peter Z. Skands. A Brief Introduction to PYTHIA 8.1. *Comput. Phys. Commun.*, 178:852–867, 2008.

[20] G. Altarelli et al. Searching for new heavy vector bosons in $p\bar{p}$ colliders. *Z. Phys. C - Particles and Fields*, 45:109–121, 1989.

[21] UA1 Collaboration. Experimental observation of isolated large transverse energy electrons with associated missing energy at $\sqrt{s} = 540$ gev. *Phys. Lett.*, B 122:103–116, 1983.

[22] UA1 Collaboration. Experimental observation of lepton pairs of invariant mass around 95 gev/c^2 at the cern sps collider. *Phys. Lett.*, B 126:398–410, 1983.

[23] G. Watt and R.S. Thorne. Study of Monte Carlo approach to experimental uncertainty propagation with MSTW 2008 PDFs. *JHEP*, 1208:052, 2012.

[24] D0 Collaboration. Search for resonant ww and wz production in $p\bar{p}$ collisions at $\sqrt{s} =$ 1.96 tev. *Phys. Rev. Lett.*, 104:061801, 2010.

[25] CDF Collaboration. Search for ww and wz resonances decaying to electron, missing e_t, and two jets in $p\bar{p}$ collisions at $\sqrt{s} = 1.96$ tev. *Phys. Rev. Lett.*, 104:241801, 2010.

[26] CDF Collaboration. Search for high-mass resonances decaying into zz in $p\bar{p}$ collisions at $\sqrt{s} = 1.96$ tev. *Phys. Rev.*, D 85:012008, 2012.

[27] ATLAS Collaboration. Search for massive resonances decaying into pairs of boosted bosons in semi-leptonic ïňĄnal states at $\sqrt{s} = 8$ TeV. *Submitted to Journal of High Energy Physics*, 2014.

[28] ATLAS Collaboration. Search for massive resonances in dijet systems containing jets tagged as W or Z boson decays in pp collisions at $\sqrt{s} = 8$ TeV. *Submitted to Journal of High Energy Physics*, 2014.

[29] ATLAS Collaboration. Search for new particles decaying to ZZ using final states with leptons and jets with the ATLAS detector in $\sqrt{s} = 7$ TeV proton-proton collisions. *Phys. Lett.*, B 712:331, 2012.

[30] L. Evans and P. Bryant. Lhc machine. *Journal of Instrumentation*, 3:S08001, 2008.

[31] ATLAS Collaboration. The atlas experiment at the cern large hadron collider. *Journal of Instrumentation*, 3:S08003, 2008.

[32] R.K. Ellis et al. Cambridge University Press, Cambridge, UK, 1996.

[33] Dieter Zeppenfeld. Standard model at hadron colliders.

[34] Michael Seymour. Searches for new particles using cone and cluster jet algorithms : a comparative study. *Z. Phys. C*, 62:127–138, 1994.

[35] J. M. Butterworth et al. Jet substructure as a new Higgs search channel at the LHC. *Phys. Rev. Lett.*, 100:242001, 2008.

[36] M. Dasgupta et al. Towards an understanding of jet substructure. *Journal of High Energy Physics*, 1309:029, 2013.

[37] Performance of large-R jets and jet substructure reconstruction with the ATLAS detector. June 2012.

[38] Studies of the impact and mitigation of pile-up on large radius and groomed jets in ATLAS at $\sqrt{s} = 7$ TeV. June 2012.

[39] ATLAS measurements of the properties of jets for boosted particle searches. *Phys. Rev.*, D 86:072006, 2012.

[40] Identifying Hadronically Decaying Vector Bosons Merged into a Single Jet. Aug 2013.

[41] D. Krohn et al. Jet cleansing: Pileup removal at high luminosity. *Submitted to Phys. Rev. D.*

[42] Performance of jet substructure techniques for large-R jets in proton-proton collisions at $\sqrt{s} = 7$ TeV using the ATLAS detector. *submitted to JHEP*, 2013.

[43] ATLAS Collaboration. High-p_T boson jet tagging with the atlas detector. 2013.

[44] D. Krohn, J. Thaler, and L.-T. Wang. Jet Trimming. *JHEP*, 02:084, 2010.

[45] S. D. Ellis, C. K. Vermilion, and J. R. Walsh. Recombination Algorithms and Jet Substructure: Pruning as a Tool for Heavy Particle Searches. *Phys. Rev.*, D 81:094023, 2010.

[46] Performance and Validation of Q-Jets at the ATLAS Detector in pp Collisions at $\sqrt{s} =$ 8 TeV in 2012. Aug 2013.

[47] Tilman Plehn, Gavin P. Salam, and Michael Spannowsky. Fat Jets for a Light Higgs. *Phys. Rev. Lett.*, 104:111801, 2010.

[48] Stefano Frixione, Paolo Nason, and Carlo Oleari. Matching NLO QCD computations with Parton Shower simulations: the POWHEG method. *JHEP*, 11:070, 2007.

[49] M. Dasgupta and D.G. Salam. Resummation of non-global qcd observables. *Phys. Lett.*, B 512:323–330, 2001.

[50] V. Rentala et al. Tagging boosted ws with wavelets. *MSUHEP-2014-04*, 2014.

[51] A. Larkoski et al. Soft drop. *Journal of High Energy Physics*, 1405:146, 2014.

[52] A. Larkoski et al. Energy correlation functions for jet substructure. *MIT-CTP 4446*, 2013.

[53] Y. Cui et al. W-jet tagging: Optimizing the identification of boosted hadronically-decaying w bosons. *Phys. Rev.*, D 83:074023, 2011.

[54] J. M. Butterworth, B. E. Cox, and J. R. Forshaw. WW scattering at the CERN LHC. *Phys. Rev.*, D 65:096014, 2002.

[55] Leandro G. Almeida, Seung J. Lee, Gilad Perez, George F. Sterman, Ilmo Sung, et al. Substructure of high-p_{T} Jets at the LHC. *Phys.Rev.*, D79:074017, 2009.

[56] Jesse Thaler and Ken Van Tilburg. Identifying Boosted Objects with N-subjettiness. *JHEP*, 03:015, 2011.

[57] Stephen D. Ellis, Andrew Hornig, Tuhin S. Roy, David Krohn, and Matthew D. Schwartz. Qjets: A Non-Deterministic Approach to Tree-Based Jet Substructure. *Phys.Rev.Lett.*, 108:182003, 2012.

[58] J. Gallichio et al. Multivariate discrimination and the higgs+w/z search. *Journal of High Energy Physics*, 1104:069, 2011.

[59] ATLAS Collaboration. Performance of shower deconstruction in atlas. 2014.

[60] ATLAS Collaboration. Electron reconstruction and identification efficiency measurements with the ATLAS detector using the 2011 LHC proton-proton collision data. *Submitted to The European Physical Journal C*, 2014.

[61] ATLAS Collaboration. Preliminary results on the muon reconstruction efficiency, momentum resolution, and momentum scale in atlas 2012 pp collision data. 2013.

[62] ATLAS Collaboration. Improved electron reconstruction in atlas using the gaussian sum filter-based model for bremsstrahlung. 2014.

[63] ATLAS Collaboration. Electron reconstruction and identification efficiency measurements with the ATLAS detector using the 2011 LHC proton-proton collision data. *Submitted to The European Physical Journal C*, 2014.

[64] ATLAS Collaboration. Staco muon reconstrution algorithm. 2012.

[65] ATLAS Collaboration. Muon momentum resolution in first pass reconstruction of pp collision data recorded by atlas in 2010. 2011.

[66] W Lampl et al. Calorimeter clustering algorithms: description and performance. April 2008.

[67] ATLAS Collaboration. Jet energy measurement and its systematic uncertainty in proton-proton collisions at $\sqrt{s} = 7$ tev with the atlas detector. *Submitted to European Physical Journal C.*

[68] T. et. al Gleisberg. Event generation with sherpa 1.1. *Journal of High Energy Phys.*, 0902:007, 2009.

[69] Stefano Frixione and Bryan R. Webber. Matching NLO QCD computations and parton shower simulations. *JHEP*, 06:029, 2002.

[70] G. Marchesini et al. A Monte Carlo event generator for simulating hadron emission reactions with interfering gluons. *Comput. Phys. Commun.*, 67:465–508, 1991.

[71] J. M. Butterworth, Jeffrey R. Forshaw, and M. H. Seymour. Multiparton interactions in photoproduction at HERA. *Z. Phys. C*, 72:637, 1996.

[72] Borut Paul Kersevan and Elzbieta Richter-Was. The Monte Carlo event generator AcerMC versions 2.0 to 3.8 with interfaces to PYTHIA 6.4, HERWIG 6.5 and ARIADNE 4.1. *Comp. Phys. Comm.*, 184:919, 2013.

[73] ATLAS Collaboration. Fast simulation for atlas: Atlfast-ii and isf. 2012.

[74] Jet energy resolution from in-situ techniques with the atlas detector using proton-proton collisions at a center of mass energy $\sqrt{s} = 7$ tev. 2011.

[75] G. Aad et al. Luminosity Determination in pp Collisions at sqrt(s)=7 TeV Using the ATLAS Detector at the LHC. *Eur.Phys.J.*, C71:1630, 2011.

[76] J. Wenniger. Energy calibration of the lhc beams at 4 tev.

[77] J.S. Conway. Nuisance parameters in likelihoods for multisource spectra. *Proceedings of PHYSTAT 2011 Workshop on Statistical Issues Related to Discovery Claims in Search Experiments and Unfolding*, 2011.

[78] G. Cowan et al. Asymptotic formulae for likelihood-based tests of new physics. *European Physical Journal*, C 71:1554, 2011.